VILNIUS UNIVERSITY

AUDRONĖ SABALIAUSKIENĖ

SYNTHESIS, INVESTIGATION AND POSSIBLE APPLICATIONS OF SELECTED PHOSPHATES AND SILICATES

Doctoral dissertation,

Physical Science, Chemistry (03 P)

Vilnius 2014

The dissertation was carried out at Vilnius University from 2009 to 2014.

Scientific supervisor:

Prof. habil. dr. Aivaras Kareiva (Vilnius University, Physical Science, Chemistry – 03 P)

Table of Contents

ACKNOWLEDGEMENTS

On the first place I would like to sincerely thank my supervisor Prof. Habil. Dr. Aivaras Kareiva, who guided me through the fields of material science all these years. I am grateful for his support, patience and goodwill.

Special thanks are given to all members of Sol-Gel scientific group, and especially to Olga Opuchovič, Skirmantė Butkutė and Olga Darčanova – to whom I got the opportunity to work personally. Sincere thanks are also gone to Plasma group (HAS), especially dr. Zoltán Károly for helping in everything about RF-thermal plasma technique. Also to dr. Nadezda V. Tarakina from University of Wuerzburg for TEM analysis and explicit contribution to mutual article.

The author would also like to acknowledge the research support provided by the Erasmus Programme of the Life Long Learning (VU) and prof. dr. János Szépvölgyi from Chemical Research Center, Hungarian Academy of Sciences. Also to VU Mobility Programme and Prof. dr. Thomas Chung-Kuang Yang from National Taipei University of Technology and Jen-Chang Yang from Taipei Medical University.

My special thanks goes to people who I gladly call my friends. They spare time to advice, discuss and help me from the beginning of my studies. Simas Šakirzanovas and Artūras Katelnikovas – Thank You. The other dearest friend, who supported me and who deserves my warmest thanks is Viktorija Tomkutė.

I must thank Ričardas and Žilvinas for being the best husband and son on the whole wide world! Above all others, they have been near day in a day out to comfort, console, encourage and empathize with me during all my hardships and successes.

Ypatingai dėkoju savo šeimai už palaikymą.

NOTATIONS AND ACRONYMS

3D – Three dimensional

AFM – Atomic force microscopy

AW – Apatite-wollastonite glass ceramic

BET – Barrett-Emmett-Teller method.

BG – Bioactive Glass

Bioglass® – Trade name for the first biologically active glass

BJH – Barrett-Joyner-Halenda analysis

C3S – Tricalcium silicate (Ca_3SiO_5)

CaP – Calcium phosphates

CDHA – Calcium deficient hydroxyapatite

CHAp – Calcium hydroxyapatite ($Ca_{10}(PO_4)_6(OH)_2$).

CTE – Coefficient of thermal expansion

DC – Dental ceramic

DCTA – Trans-1,2-diaminocyclohexane-N,N,N',N'-tetraacetic acid monohydrate

DTA – Differential thermal analysis

DTG – Differential thermal gravimetry

EDTA – Ethylenediamine-N,N,N',N'-tetraacetic acid

EDX – Energy-dispersive X-ray spectroscopy

EG – 1,2-Ethanediol

GC – Glass Ceramic

IPC – Interpolymer complex

IR – Infrared spectroscopy

KHN – Knoope’s microhardness

Le – Leucite ($KAlSiO_6$)

PFM – Porcelain-fused-to-metal

pH – Decimal logarithm of the reciprocal of the hydrogen ion activity

PL – Photoluminescence

RF – Radio frequency

SBF – Synthetic body fluid

SEM – Scanning electron microscopy

SPS – Spark plasma system

TA – 2,3-dihydroxybutanedioic acid (tartaric acid)

TEA – Triethanolamine

TEM – Transmission electron microscopy

TEOS – Tetraethyl orthosilicate ($Si(OC_2H_5)_4$)

TG – Thermal gravimetry

XRD – X-ray diffraction

CHAPTER 1

1.1 INTRODUCTION

One of the most exciting and rewarding chemical research areas of material science implicates applications of materials used for medical purposes. Different ceramics and glasses have been employed in modern health care industry for more than 50 years, while the desire to substitute hard tissue and reach better quality of life was always a preference for mankind.

As lifespan increases we all eventually ran out of spare parts, mostly the calcined tissue. The body tissues and organs begin to deteriorate and degenerate from the age of 30 onwards. The great challenge for chemist is to perform materials that would be resistant to the harsh environment of the human, such as the corrosive food and saline solution of 37 °C, multiaxial mechanical loads. The materials should also possess biocompatibility and osteocunductivity. They should be bioinert, bioactive or bioresorbable [1]. Thus, cause as less damage to surroundings as possible. Early dental implants, such as ivory, bone, wood, extracted animal or human teeth were not stable, decayed, stained and permanently malodorous dentures [2]. Other bone replacements were hardly imaginable. Eventually, the most important factor of implants is the co-existence of biomaterial and hosting tissues [3]. Therefore, scientists should be aware of many factors that might have influence to final product – biomedical material. Beside the technical approach to the sintering, characterizing, manufacturing and testing materials, chemists should also have specific knowledge about the bones and surrounding tissues. The mineral in bone and dentine is a poorly-crystalline analog of the geologic mineral calcium hydroxyapatite ($Ca_{10}(PO_4)_6(OH)_2$), CHAp. The analogy was recognized from X-ray diffraction analyses performed almost a century ago. In the 1920s *de Jong* first observed the similarities between the X-ray diffraction patterns of bone minerals and calcium phosphate compound – hydroxyapatite [4]. The crystal structure of a

single crystal of stoichiometric hydroxyapatite was solved in 1964 [5]. Since then, an extremely important period in the development of bioceramics came on age with major contributors include Professors *Bonfield*, *Hench*, *DeGroot*, and *Kokubo* with Professors *Zhang*, *Aoki* and *Jarcho*, who provided major advances around the world [6-11].

As a class of biomaterials, ceramics, glasses, and glass-ceramics are generally used to repair or replace skeletal hard connective tissues. The huge number of different biomaterials are widely used in orthopedics and orthodontics [4, 12, 13]. Current applications include total and partial hip, knee, teeth, tendon, ligaments replacements, and repair for periodontics, maxillofacial reconstruction, augmentation and stabilization of the jawbone, spinal fusions and bone fillers after surgeries [14]. The wide variety of different and sophisticated applications might make wrong impression than all above mentioned materials are also of different origin. However, bioceramics can be prepared from alumina, zirconia, carbon, silica-containing compounds and some others [14, 15]. Bioceramics bonding with bone was first demonstrated *by Hench et al* in 1971. The system of SiO_2–Na_2O–CaO–P_2O_5 with B_2O_3 and CaF_2 additions formed a strong, adherent bond with bone [6]. The firs porcelain inlay was introduced in the early 1800s, though the porcelain fused to metal (PFM) crowns were refined in 1900s [16]. Feldspathic glasses became the predominant matrix material for dental restorations and up to day their composition essentially remain alkali-modified aluminosilicate glasses [2]. The tetragonal leucite (K_2O–Al_2O_3–$4SiO_2$, or $KAlSiO_6$) is commonly used as bodies in dental porcelain [17]. Usually, ceramics have high melting point above 1000 °C that makes processing and manufacturing quite difficult and aggregative. Moreover, CHAp becomes unstable and decomposes at temperatures ~1250–1300 °C. Thus, the desirable synthesis temperature is 1000 °C and less.

1.2 THE THESIS FOCUS AND SCOPE

This thesis focuses on the development of efficient and powerful synthesis methods of CHAp and Le (leucite), investigation and characterization of the intermediate and final products. The finding of specific synthesis parameters and particle size of the final products were preferential targets. The research activities in this thesis follow the two different biomaterial groups of metal phosphate and silicate systems. Both are well known but still under intense investigation and systematic examination for modern applications. Recently, lanthanide-doped calcium hydroxyapatite nanoparticles have attracted extensive attention on the potential applications as luminescent biological labels due to their excellent spectral characteristics and biocompatibility. This work includes investigations of doped CHAp. Doped $KAlSiO_6$ ceramics are discussed as well, since glasses are promising hosts to investigate the influence of chemical environment on the optical properties of the rare earth ions [18, 19].

The main tasks of PhD thesis were formulated as follows:

- To synthesize nano-hydroxyapatite samples with different morphological properties using aqueous sol–gel chemistry routes by changing starting materials, complexing agents and using milling procedures;
- To elucidate the potentials of designed calcium hydroxyapatite nanoparticles for dental and orthopedic applications;
- To investigate Ce^{3+} and Mn^{2+} substitution effects in CHAp ($Ca_{10-x}Ce_x(PO_4)_6(OH)_2$ and $Ca_{10-x}Mn_x(PO_4)_6(OH)_2$).
- To synthesize leucite (K_2O-Al_2O_3-$4SiO_2$) ceramics using an aqueous sol-gel chemistry processing and RF thermal plasma routes;
- To investigate Ce^{3+}, Eu^{3+}, Sm^{3+} and $Tb^{3+/4+}$ substitution effects in Le ceramics.

1.3 STATEMENT PRESENTED FOR THE DEFENCE

- Aqueous sol-gel synthesis route provides lower synthesis temperatures. The low synthesis temperature provides better manufacturing possibilities and quality of end products. This synthesis route provides more controlled crystallization regime. Ceramics prepared by this route possess high homogeneity that is necessary for the glass-ceramic machinability and good strength.
- RF thermal plasma technology is a novel synthesis and manufacturing technique for bioactive glass and glass-ceramic materials. Thermal plasma has several advantages over other conventional techniques that allow to prepare materials with advanced properties for a variety of applications.
- The sol-gel chemistry processing route is suitable technique for the synthesis of lanthanide-substituted metal phosphate and silicate ceramics.

1.4 SCIENTIFIC NOVELTY AND SIGNIFICANCE

Different complexing agents were successfully used in the preparation of monophasic calcium hydroxyapatite (CHAp) by an aqueous sol-gel technique. 1,2- diaminocycloheksanetetracetic acid monohydrate (DCTA) as complexing agent in the sol-gel processing was suggested for the first time. It was shown that selection of starting materials and complexing agents in the sol-gel processing allows to control the phase purity and grain size of the resulting $Ca_{10}(PO_4)_6(OH)_2$ powders. The hydroxyapatite nano-powders were synthesized by using low-energy milling. This technique is remarkable due to the easiness of application. The hydroxyapatite nano-powders were successfully developed at bone blocks and teeth remineralization. Simple and environmentally friendly sol-gel synthesis processing was successfully applied for the preparation of monophasic leucite. Moreover, leucite ceramics was doped with different lanthanide elements for optical

applications. It was demonstrated that RF thermal plasma route is suitable synthesis methods for the preparation core-shell nanostructures.

CHAPTER 2 GENERAL KNOWLEDGE ON BIOMATERIALS

This chapter gives an overview of the biomaterial field.

A number of definitions for the term "biomaterials" have been developed. The most common was that *biomaterials* or biomedical materials are defined as synthetic or natural materials to be used to replace parts of living system or to function in intimate contact with living tissues [20]. However, according to *Williams*, the situation has changed as medical technologies now encompass a range of drug and gene delivery systems, tissue engineering and cell therapies, organ printing and cell patterning, nanotechnology based imaging and diagnostic systems and microelectronic devices. These technologies still encompass metals, ceramics and synthetic polymers, but also biopolymers, self-assembled systems, nanoparticles, carbon nanotubes and quantum dots. The 'material' can be a single, well defined and characterized entity, such as a titanium alloy or hydroxyapatite ceramic, or it can be a virus coated with a layer of a cationic polymer. Therefore, there are an advice to refine the biomaterial paradigm and redefine the word "biomaterial" as following [21]:

''A biomaterial is a substance that has been engineered to take a form which, alone or as part of a complex system, is used to direct, by control of interactions with components of living systems, the course of any therapeutic or diagnostic procedure, in human or veterinary medicine.''

All biomaterials are distinguished into three main groups, also called – generations. **1st generation** bioinert, non-absorbable materials such as carbons, Al_2O_3 and ZrO_2. **2nd generation** biodegradable materials that are resorbable and dissolves after specific time, e.g. calcium phosphates, calcium sulphate, calcium sulphates and phosphates + ZnO, Al_2O_3, Fe_2O_3, also $CaCO_3$; **bioactive** materials that are surface reactive and tightly bonds to living tissues, e.g. calcium hydroxyapatite (CHAp), pure and substituted hydroxycarbonate apatite, glasses and

glass-ceramics. **3rd generation** scaffolds of biologically active molecules that stimulate regeneration of living tissues, e.g. Bioglass® in particular form, porous biodegradable and bioactive ceramics, advanced bioceramics: mesoporous materials, organic-inorganic hybrids [22, 23].

There is growing need for bioactive materials, as they replace large areas of bone which cannot heal themselves. Bioactivity is merely the ability of direct attachment to bone tissue without the formation of a fibrous tissue layer at the bone.

2.1 GLASSES, CERAMICS AND BIOCERAMICS

Ceramic materials are inorganic materials which consist of metallic and nonmetallic elements bonded together primarily by ionic and/or covalent bonds. The variation of chemical compositions enables to create a variety of chemical materials used today. New and advanced ceramic materials, such as alumina, zirconia, silicon carbide and nitride, are generally distinguished as structural ceramics for their high strengths, hardness and toughness. Above mentioned ceramics are considered as bioinert, as they do not form any bonds with living tissue. Ceramic materials may have a crystalline or partly crystalline structure, or may be amorphous and glassy. Glass-ceramics (GC) are materials composed of one or more glass and crystal phases [24].

The bioactivity mechanism of bonding of biomaterials to living tissue, especially of bioactive glasses (BG), was introduced by *Hench* [5, 25]. BG are presented in Table 1 that is adopted from [5, 6, 25]. The chemical reactions which occur on the surface of bioactive glasses proceed mostly via 5 steps. Firstly an exchange between alkali ions from the glass and hydrogen ions from the solution takes place. Secondly the silica structure breaks down and the glass totally dissolves at the interface. Further the SiO_2 polymerization reaction contributes to the enrichment of surface SiO_2-rich gel layer. Later an amorphous calcium phosphate film precipitates on this layer and is followed by crystallization to form carbonated HA crystals where

calcium and phosphate ions provide the nucleation sites for crystallization. The more bioactive glass is the faster these surface reaction reach completion.

Table 1. Reaction stages of BG implant

1	Rapid exchange of Na^+ or K^+ with H^+ from solution: 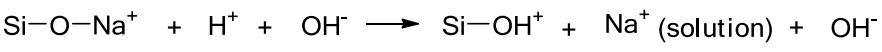 This stage is usually controlled by diffusion and exhibits a $t^{-1/2}$ dependence.
2	Loss of soluble silica in the form of $Si(OH)_4$ to the solution, resulting from breaking of Si–O–Si bonds and formation of Si–OH (silanols) at the glass solution interface: 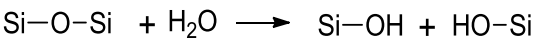 This stage is usually controlled by interfacial reaction and exhibits a $t^{1,0}$ dependence.
3	Condensation and repolymerization of a SiO_2-rich layer on the surface: 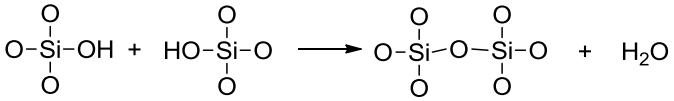
4	Migration of Ca^{2+} and PO_4^{3-} groups to the surface through the SiO_2-rich layer forming a $CaO–P_2O_5$-rich film on top of the SiO_2-rich layer, followed by growth of the amorphous $CaO-P_2O_5$-rich film by incorporation of soluble calcium and phosphates from solution.
5	Crystallization of the amorphous $CaO–P_2O_5$ film by incorporation of OH^-, CO_3^{2-}, or F^- anions from solution to form a mixed hydroxyl, carbonate, fluorapatite layer.
6	Adsorption of biological moieties in CHAp layer.
7	Action of macrophages.
8	Attachment of osteoblast stem cells.
9	Differentiation and proliferation of osteoblasts.
10	Generation of matrix.
11	Crystallization of matrix and growth of the bone.

The biological response of living cells at the interface with the bioactive glass is to the presence of the growing carbonated CHAp layer, and not a foreign body. Carbonate (CO_3^{2-}) anions substitute for OH^- in the apatite crystal structure to form a carbonated hydroxyapatite similar to living bone. Crystallization of carbonated CHAp takes place around collagen fibrils and results in interfacial bonding. The five stages of surface reactions occur within 24 hours. The reaction layers enhance adsorption and desorption of growth factors produced by the cells, and greatly decrease time that is necessary for macrophages to prepare the implant site for tissue repair. Mineralization of the matrix and mature osteocytes is the final product by 6 – 12 days.

There is a well-established relations between the ability of a given material to form bonds with living tissue and form apatite like layer. The Table 2 describes the types of possible attachments in details.

Table 2. Types of bioceramics-tissue attachment and bioceramic classification [25]

Type of bioceramics	Type of attachment	Example
1	Dense, nonporous, nearly inert ceramics attach by bone growth into surface irregularities by cementing the device into the tissues, or by press fitting into a defect (termed morphological fixation).	Al_2O_3 (single crystal and polycrystalline)
2	For porous inert implants bone ingrowth occurs which mechanically attaches the bone to the material (termed biological fixation).	Al_2O_3 (porous polycrystalline). Hydroxyapatite-coated porous metals
3	Dense, nonporous, surface reactive ceramics, glasses and glass-ceramics attach directly by chemical bonding with the bone (termed bioactive fixation).	Bioactive glasses. Bioactive glass-ceramics. Hydroxyapatite
4	Dense, nonporous (or porous), resorbable ceramics are designed to be slowly replaced by bone.	Calcium phosphate salts. Calcium sulfate dihydrate. Tricalcium phosphate

2.1.1 Diversity and applications

Silica based bioceramics are probably the largest group of biomaterials. The characteristic amorphous quality of these glasses is basically a product of the structure of silicate glasses, [SiO_4] tetrahedral. These geometrical figures are linked together at all corners, while crystallized silica shows uniform arrangements. Either way, they form the glassy network and are called *network formers.* The inclusions of cations in the network are referred as *network modifiers*. They provide lower melting temperatures, viscosity values and high degree of disorder that increase reactivity of these glasses in aqueous environment [26].

Many bioactive silica glasses (SiO_2–CaO–P_2O_5) are based upon the formula called **45S5**, signifying 45 wt. % SiO_2 (S = the network former) and 5:1 ratio of CaO to P_2O_5. Glasses with lower ratios of CaO to P_2O_5 do not bond to bone. The substitutions in the 45S5 formula of 5–15 wt. % B_2O_3 for SiO_2 or 12.5 wt. %

CaF_2 for CaO or heat treating the bioactive glass compositions to form glass-ceramics has no measurable effect on the ability of the material to form a bone bond. However, adding as little as 3 wt. % Al_2O_3 to the 45S5 formula prevents bonding to bone [4, 5, 15]. This glass has been developed to replace hard or even soft tissue, and due to its insoluble properties, it has potential as a long-term device. In order to enhance bioactivity of BG different modifiers are incorporated in the SiO_2 network [27].

The possible applications of bioactive materials are listed in Table 3.

Table 3. The bioactive materials and their clinical applications.

Type	Applications
Glasses	
$Na_2O–CaO–SiO_2–P_2O_5$ bioglass-type	Ossicle replacement in the middle ear, cone-shaped devices for jaw defects filling, curved plates for restoring eye orbit floor, soft tissue sealing for transdermal implants, Bone tissue replacement in periodontal diseases, soft tissue augmentation in paralysis of vocal cords, Maxillofacial reconstructions: bone tissue reconstructions in frontal sinus infections, chronic pansinusitis, mucocele, lower jaw restoring after tumor removal or posttraumatic injury, sinus lift operation; Spine reconstruction: lumbar radicular syndrome [28].
$Na_2O–CaO–B_2O_5–Al_2O_3–SiO_2–P_2O_5$	
$Ca–SiO_2$	
Glass-ceramics	
$Na_2O–K_2O–MgO–CaO–SiO_2–P_2O_5$ CHAp containing	
$MgO–CaO–SiO_2–P_2O_5$ apatite-wollastonite containing	
$Na_2O–MgO–CaO–SiO_2–P_2O_5–F$ Bioverite type apatite and fluoroflogopite-like mica containing GC	
Crystalline ceramics	
Sintered CHAp	Dental applications, orthopedics, metal coatings for prosthesis.
Sintered β-TCP	
Sintered BCP	
$CaSO_4$	
Calcite	
Leucite	Reinforcement for dental applications, crowns and fixed bridges.
Inorganic-organic composites	
Polyethylene containing glass ceramics AW particles	Prosthesis, graft materials.

A range of Ca-Si based glasses are employed in bone reconstruction as they also have excellent bone bonding ability [29]. Tricalcium silicate (Ca_3SiO_5, C3S) is a typical group of Ca-Si-based bioactive ceramics for bone tissue regeneration due to its excellent self-setting property, bioactivity, and degradability and stimulation effect on cell growth. The beneficial effects of Zn on the **C3S** formation and osteointegration for bone tissue repairing applications.

Lithium disilicate glass-ceramic showed a great deal for dental applications. Initially, the materials system $SiO_2–Li_2O–P_2O_5–La_2O_3–ZnO–Al_2O_3–K_2O$ was

developed for the product called **IPS Empress® 2** [24]. Subsequently, the materials systems SiO_2–Li_2O–P_2O_5–ZnO–Al_2O_3–K_2O and SiO_2–Li_2O–P_2O_5–ZrO_2–Al_2O_3–K_2O were developed as well. The ZnO-free system containing ZrO_2 allows the optical properties to be selectively controlled (translucency without additional opalescence) [30].

However, the long-term reaction to silica, both locally and systemically, is still unknown [31]. In addition, the use of phosphate glasses offers a more controlled rate of dissolution, as compared to silica containing glasses. Other different types of ceramic materials have also been developed that have osteoconductive and osteoinductive properties, which make them effective in the repair and regeneration of bone. These include hydroxyapatite and wollastonite and other inorganic phosphates containing glass ceramics [32]. Phosphate based bioglasses (PBG) have basic composition CaO–Na_2O–P_2O_5 and have gained major interest as bone filling materials and for fabricating scaffolds for bone tissue engineering. Their advantages are high solubility, degradability and chemical similarity to the inorganic phase of human bone. The network former of PBGs is a phosphate (PO_4^{3-}) which is highly degradable and the glass can be engineered to include mineral elements, such as Ca^{2+}, Na^+, Mg^{2+}, Sr^{2+} and K^+ – network modifiers [33]. There are established that only glass compositions containing 50 mol% or above of P_2O_5 were suitable for fiber fabrication [34]. Calcium orthophosphate based materials of the ternary system $Ca(OH)_2$– H_3PO_4–H_2O are also widely used for medical applications.

Apatite-Wollastonite glass-ceramic (AW) production and behavior was firstly reported in 1982 [35]. A dense and homogenous composite of 38 wt. % oxyflourapatite ($Ca_{10}(PO_4)_6(O,F)_2$) and 34 wt. % β-wollastonite ($CaO{\cdot}SiO_2$) crystals, 50–100 nm in size in MgO–CaO–SiO_2 glassy matrix was obtained after heat treatment. This glass ceramic has high mechanical strengths and is capable of forming strong chemical bonds with bone. P_2O_5 is one of the most widely used nucleating agents for glass. Following work on adding Li_3PO_4 to binary $Li_2O{-}SiO_2$

revealed that substitution of 1 mol % P_2O_5 for the equivalent amount of SiO_2 results in significant phase separation; also observed that the addition of 1 mol % P_2O_5 resulted in a much finer grained microstructure [36].

The 45S5 glass known as Bioglass® (for orthopedic surgery – NovaBone®) consists of a silicate network which incorporates sodium, calcium and phosphorus with a composition of 45% SiO_2, 24.5% Na_2O, 24.5% CaO and 6% P_2O_5. In the 1970s, Brömer and Pfeil developed one of the earliest glass–ceramics for clinical use. Ceravital® in the SiO_2–CaO–P_2O_5–Na_2O–K_2O–MgO system contains crystalline apatite. In 1983, Höland et al. developed a new series of bioactive glass–ceramics, which they called Bioverit® I. This material could be machined with standard tools and retouched in the operating theatre. It is in the SiO_2–Al_2O_3–MgO–Na_2O–K_2O–F–CaO–P_2O_5 system which undergoes a controlled nucleation and growth of crystals resulting in the presence of fluoroflogopite–like mica (Na/KMg_3[$AlSi_3O_{10}F_2$]) in the glassy matrix. A second family of Bioverit®, called Bioverit® II, was produced following the success of type I which contained much lower P_2O_5 content but other crystalline phases of cordierite (Mg_2[$Si_5Al_4O_4$]). Höland alongside Vögel further developed the Bioverit® to create a III version using a phosphate glass in the P_2O_5–Al_2O_3–CaO–Na_2O system with no silica content but doped with Fe_2O_3 and ZrO_2 [37].

Most dental porcelains for metal–ceramic systems contain leucite ($KAlSi_2O_6$) as the main crystalline phase to increase the thermal expansion coefficient and the mechanical resistance of the porcelain. The glass matrix of these porcelains consists of about 75 to 85 wt. % of feldspar. Therefore, opaque porcelains contain oxides such as SnO_2 and ZrO_2 to veil the dark color of metallic frameworks. However, dental porcelains present only leucite as crystalline phase since their role is to provide high translucency to simulate the dentine structure of a natural tooth [38].

2.1.2 Synthesis methods

The bioactive glasses and glass-ceramics can be prepared by the classic quenching technique of melts and sol-gel processing. The principal scheme of glass preparation is presented in Figure 1.

Melt-quenching technique is simple and suitable for massive production. However, during the high temperature stage, the volatile component P_2O_5 tends to escape. The sol-gel process has great versatility: bioactive glasses can be made as nanoporous powders or monoliths or as nanoparticles simply by changing the pH of the process [39]. The physical differences in melt and sol-gel derived glasses are that sol-gel glasses tend to have an inherent nanoporosity whereas melt-quenched glasses are dense.

The first bioglasses were prepared by conventional melt-quenching technique, where starting materials are melted together at high temperatures (above 1300 °C) in a platinum crucible and quenched in a graphite mould (for rods or monoliths) or in water (frit). High purity SiO_2, Na_2CO_3, $CaCO_3$ and P_2O_5 powders were weighted and mixed to obtain 45S5 Bioglass® (45 SiO_2, 24.5 CaO, 24.5 Na_2O, 6 P_2O_5 in wt. %). The powders were melted in a Pt crucible for 4 h at 1400 °C. The melt was then quenched in water and ground in ethanol to a fine powder (1 μm) [40].

Glasses of phosphate based (PBG) $CaO–Na_2O–P_2O_5$ system were prepared from P_2O_5, NaH_2PO_4 and $CaCO_3$. The precursors were placed in a Pt/10 % Rh crucible and heated between 1100 and 1200 °C for 1 h. Upon removal, the glass was poured into a graphite mould preheated to 350 °C. The mould was then placed in a furnace at 350 °C and slowly cooled to room temperature to remove any residual stress [41]. The bioactive glass of the system $CaO–SiO_2–P_2O_5$ with 57.44 % CaO, 35.42 % SiO_2 and 7.15 % P_2O_5 was obtained by melting the oxides at 1600 °C for 2.5 h and posterior quenching in water to room temperature [42].

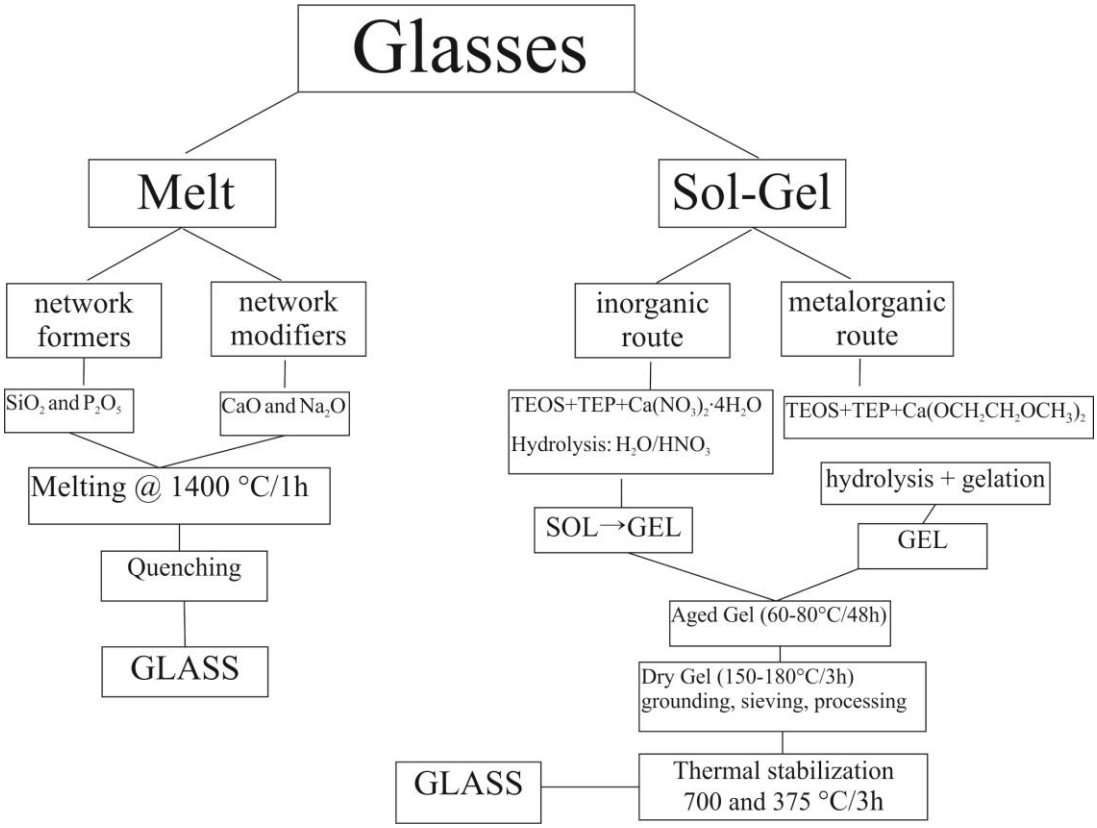

Figure 1. The main stages in the melting and sol-gel processes of glass preparation

The A-W glass ceramic in the ternary system of $3CaO{\cdot}P_2O_5$–$CaO{\cdot}SiO_2$–$MgO{\cdot}CaO{\cdot}2SiO_2$ was prepared from MgO, $CaCO_3$, SiO_2, $CaHPO_5{\cdot}2H_2O$ and CaF_2 by calcination in Pt10%Rh crucible at 1000 °C for 10 h and then melting at 1450 °C for 2 h in a SiC furnace. Consequently, the melts were poured onto a steel plate and pressed into plates of 2 mm thick. The glass plates as-prepared from the melts, to provide crystal growth from the glass surface, were pulverized in alumina ball mill and mixed with water (10:1), then pressed into discs and heat treated up to 1050 °C at a rate of 5 °C/min. and held for 2 h in a SiC furnace [35].

Sol-gel method has been reported to produce glasses and glass-ceramics with enhanced bioactivity, as it provides composite materials with fine porous textures and enhanced bioactivity compared to the melt-derived materials of the same composition [43, 44]. In 1991, Li et al. showed that a stable bioactive gel-glass

could be made by sol-gel processing [45]. A typical silicate precursor is tetraethyl orthosilicate (TEOS), $Si(OC_2H_5)$, which hydrolysis under acidic or basic conditions to form a sol containing nanoparticles. If synthesis is carried out under basic conditions (Stöber process), spherical bioactive nano- and submicrometre particles can be formed. Common precursors for introducing calcium and phosphate into the sol-gel are calcium nitrate tetrahydrate and triethylphosphate, respectively.

A group of sol-gel derived bioglasses in the system of SiO_2–CaO–P_2O_5 has been widely studied, such as 55S, 58S, 60S, etc. Series of glasses with different SiO_2 constituent nearly 90 wt. % were examined. The new method offered many wide variety of glass processing into particles, fibers, foams, porous scaffolds, coatings, and net shaped monoliths. Lately, the sol-gel processing of bioactive gel-glasses was simplified by eliminating P_2O_5. The $70SiO_2/30CaO$ (in mol %) system was as bioactive as 58S or 45S5 [46]. The gel-glass powder containing 70 mol % SiO_2 and 30 mol % CaO was prepared in a large polymethyl pentene (PMP) container using 935 mL of tetraethylorthosilicate, $Si(OC_2H_5)_4$, 98 %, and 425 g of calcium nitrate tetrahydrate, $Ca(NO_3)\cdot 4H_2O$, A.C.S reagent. Deionized water and 2 M nitric acid were used as catalysts for the hydrolyzation TEOS. The prepared sol was immediately transferred to an oven at 60 °C for aging. Gelation occurred within a few hours at this temperature [47, 48].

Recently ultrasonic assisted synthesis and microwave assisted synthesis are gaining attention as they can help to reaction in a short time and can modify the reaction environment to produce nano phase powders. The calcium nitrate tetrahydrate, diammonium hydrogen phosphate and sodium silicate (as 37 % SiO_2 in NaOH solution) were dissolved in deionized water and transferred to the ultrasonic bath. Microwave operation was performed in a second batch of powders after the ultrasonic irradiation. The obtained amorphous powder was washed in de-ionized water, filtered, dried for 24 hours in oven at 80 °C and calcined at 700 °C temperatures for the development of BG [49].

2.2 MANUFACTURING AND SCAFFOLD PROCESSING METHOD OF IMPLANTS

Orthopedic biomaterials are limited to those materials that can withstand cyclic loadbearing applications. While metals, polymers, and ceramics are used in orthopedics, it remains metals, which have provided appropriate material properties such as high strength, ductility, fracture toughness, hardness, corrosion resistance, formability, and biocompatibility necessary for most loadbearing roles required in fracture fixation and total joint arthroplasty (TJA) [50, 51]. The most used metal alloys are stainless steel 316 L, Co based alloys (Co–Cr–Mo), Ti alloy (Ti–6 % Al– 4 % V). However, metals do not develop a chemical bond with bone, and wear, and corrosion of the metallic implant overtime can lead to the release of metallic particles causing different pathologies that could finally end in the removal of the implant [52]. The most extensive applications in both orthopedics and dentistry have involved CHAp and Le. Those have been used as a cladding for metal prostheses. The elastic properties (modulus) of Le, CHAp and related compounds are compared with those of bone, dentin and enamel. In the production of dental metal-ceramic systems for oral rehabilitation, a metal alloy is used to increase the mechanical strength of the system while the porcelain plays an aesthetic function.

The mechanically strong bioinert or biotolerant prosthesis has been coated with bioactive calcium orthophosphate. For instance, metallic implants are encountered in total hip joint replacement and artificial teeth sockets. The major advantage is the bonding between metal framework and host bone via calcium orthophosphate. Moreover, it serves as shield for the substrate surface from the environmental attack and decrease the potential release of hazardous chemicals from core implant [53]. There are various techniques to deposit bioactive coatings on the metallic surface, such as thermal spraying, sputter coating, pulsed laser deposition, dynamic mixing method, sol-gel technique, electrophoretic deposition, biomimetic coating, hot isostatic pressing and electrochemical deposition [54, 55].

Today, porcelain plays a vital role in restorative dentistry. Common uses include full coverage as crowns, inlays and onlays, porcelain bridges, veneering agents, castable ceramics and porcelain-fused-to-metal, or PFM, restorations. PFM crowns and bridges are widespread and popular as overtime they showed positive clinical results. The bonding of porcelain to metal occurs via Van der Waals forces, mechanical interlocking between the two materials, chemical bonds between the porcelain and metal oxide layer, and the compressive force caused by the slightly different thermal expansion coefficients of porcelain and metal [56]. Porcelain, a specific type of ceramic is essentially made from white clay (kaolin), quartz and feldspar. To reinforce the porcelain, by increasing the hardness and raise the coefficient of thermal expansion (CTE), leucite is commonly used. It is important that the coefficient of thermal expansion of the porcelain would be slightly less than that of the metal substrate to prevent the happening of bond failure between ceramic and metal. However, the ordinary CTE of porcelain is less than 10×10^{-6} $°C^{-1}$, which is too low compared to some metals such as gold and Ni–Cr alloy. Leucite has a higher CTE (2.8×10^{-5} $°C^{-1}$), high strength and therefore dental porcelain will be strengthened, translucent and compatible to the metal matrix during thermal expansion by adding leucite [57-59].

Hot pressing is a common technique for both sintering and forming of all dental ceramic. Firstly, moulds are fabricated to desirable shape. Secondly, powder materials or ingots are placed in moulds and when heated to sintering temperature the pressure is applied via a ram and the materials fills the moulds' cavities. Typical dental glass-ceramics used in clinics are IPS Empress and IPS Empress2. The first one consists of 17–23 wt. % Al_2O_3, 10–14 wt. % K_2O, 3–7 wt. % Na_2O, 58–63 wt. % SiO_2 as main components, additives such as B_2O_3, BaO, CaO, CeO_2, TiO_2 and 0,5–2 wt. % of pigments. Le crystals content is in the range of 40–60 vol. %. Depending on its composition, the glass transformation temperature is in the range of 625–650 °C. Mould and ingot are warmed-up to 850 °C for 90 min to get even

temperature distribution and when heated to 1100 °C a slight pressure is applied on to the piston until its movement per minute is smaller than a preset threshold value. Afterwards the mould is destroyed, the restorations are glass pearl-blasted, and the sprues are removed. IPS Empress2 consists of up to 5 wt. % Al_2O_3, up to 13 wt. % K_2O, up to 6 wt. % La_2O_3, up to 13 wt. % Li_2O, 7–5 wt. % Na_2O, up to 11 wt. % P_2O_5, 57-80 wt. % SiO_2, up to 8 wt. % ZnO as main components, up to 8 wt. % other additives and pigments. Lithium disilicate $Li_2Si_2O_5$ crystals content is more than 60 vol. % with additions of a secondary face of lithium orthophosphate. Its glass transformation temperature is 535 °C and pressure temperature – 920 °C [60-62].

In the bone tissue regeneration, large size parts with distinct 3D form require a support for their formation from cells. The support is called scaffold, template and/or artificial extracellular matrix (ECM). Typically, materials for scaffolds should be biocompatible, should promote adhesion and proliferation, mimic host bone morphology, and should not exhibit degradation products that provoke artificial tissue rejection. Scaffolds for tissue engineering are commonly constructed from biodegradable polymers, unfortunately they have low mechanical strength. Although brittle, scaffolds fabricated form bioceramics or bioglasses provide higher mechanical strength. The best candidate is CHAp due to its physical and chemical resemblance to natural bone. A large number of synthetic bone substitutes such as CHAp, β-TCP and calcium phosphate cements, and glass ceramics are available [63, 64]. Those ceramics have been used in dental and orthopedic surgery to fill bone defects and to coat metallic implant surfaces to improve implant integration with the host bone [65]. There are also growing interest in nano CHAp (n-CHap) as it exhibits improved sinterability and enhanced densification due to larger surface area, which could improve the fracture toughness as well as other mechanical properties [66].

One of the most important physical properties of scaffolds is porosity. According to IUPAC pores less than 100 nm should be referred as nanopores. Pores below 2 nm – micropores, 2–50 nm – mesopores and 50–1000 nm – macropores. A high porosity and pores with interconnections allows cell migration and nutrition diffusion [67]. Namely, scaffolds should have a network of interconnected pores where more than 60 % of pores should have a size ranging from 150 to 400 μm and at least 20 % should be smaller than 20 μm. The pore of <1 μm interact with proteins and are responsible for bioactivity; 1–20 μm have a biochemical effect on type of cells attracted, cellular development and orientation and directionality of cellular ingrowth; 100–1000 μm effect cellular growth, bone ingrowth and gives predominant function in the mechanical strength; >1000 μm provides implant functionality, implant shape and implant esthetics [68]. Images of porous phosphates and CHAp scaffold [69] are shown in Figure 2.

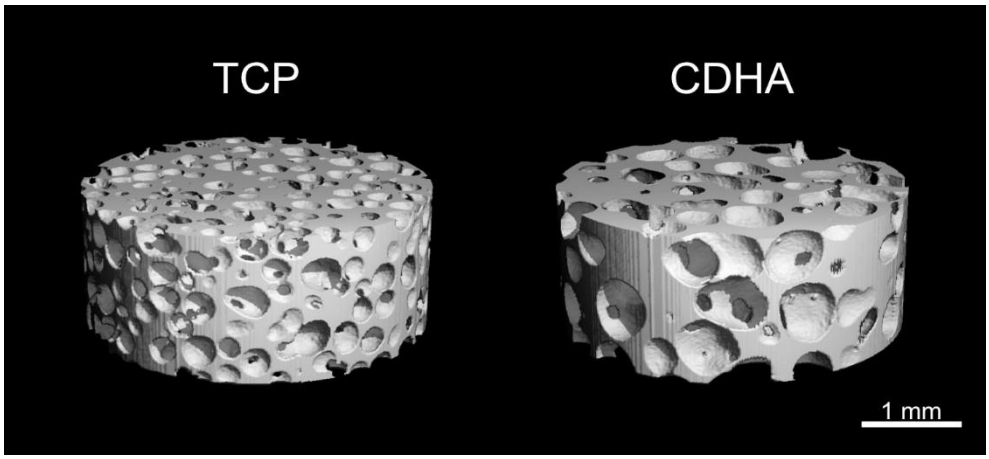

Figure 2. Micro-computed tomography (μCT) images of a porous tricalcium phosphate (TCP) and a calcium-deficient hydroxyapatite (CDHA) scaffold.

There are several scaffold fabrication techniques to produce calcium orthophosphate scaffolds with desirable architectural. These can include the use of porogens which can melt, dissolve or produce gas bubbles, e.g. microsphere sintering, gelcasting, foaming method, freez-drying, sol-gel processing, solid free-form fabricating (SFF), replication method, 3D printing [70, 71]. One of the most

popular replication method involves preparation of green bodies of ceramic (or glass) foams by coating a polymer (e.g. polyurethane) foam with a ceramic (or glass) slurry. The polymer, having the desired pore structure, simply serves as a sacrificial template for the ceramic coating. The polymer template is immersed in the slurry, which subsequently infiltrates the structure and ceramic (glass) particles adhere to the surfaces of the polymer. Excess slurry is squeezed out leaving a more or less homogeneous coating on the foam struts. After drying, the polymer is slowly burned out in order to minimize damage to the ceramic (glass) coating. Once the polymer has been removed, the ceramic (or glass) network is sintered to a desired density. The process replicates the macrostructure of the starting sacrificial polymer foam, and results in a rather distinctive and well-defined microstructure within the struts [39, 72].

CHAPTER 3 BIOPHOSPHATES

3.1 BIOAPATITES

In biological systems calcium orthophosphates occur in the principal inorganic constituent of bones, teeth, fish enameloid, and some species of shells. CHAp is a type of calcium phosphate that exhibit similarities to the mineralized tissue of mammals, such as bone and teeth. Although, biological apatite are non-stechiometrical structure and are poorly crystalized, due to the trace elements such as K^+, Na^+, Mg^{2+}, F^-, Cl^- and CO_3^{2-}. Detail information on the chemical composition of the most important calcified human tissue is given in Table 4 [73]. Hence, the chemical formula of bioapatites can be written as $(Ca,M)_{10}(PO_4,Y)_6(OH,X)_2$, where M represents cations (Mg^{2+}, Na^+, K^+, Sr^{2+}, and Ba^{2+}, etc), Y represents CO_3^{2-}, HPO_4^{2-}, SO_4^{2-}, etc., and X represents F^-, Cl^-, CO_3^{2-}, etc [74].

Table 4. Composition of the mineral phase of the human bone.

Composition	Enamel	Dentine	Bone	CHAp
Constituents, wt. %				
Calcium	36.5	35.1	34.8	39.6
Phosphorus	17.7	16.9	15.2	18.5
Ca/P (molar ratio)	1.63	1.61	1.71	1.67
Sodium	0.5	0.6	0.9	±
Magnesium	0.44	1.23	0.72	±
Potassium	0.08	0.05	0.03	±
Carbonate	3.5	5.6	7.4	±
Fluoride	0.01	0.06	0.03	±
Chloride	0.30	0.01	0.13	±
Pyrophosphate,(as $P_2O_7^{4-}$)	0.022	0.10	0.07	±
Total inorganic	97	70	65	100
Total organic	1.5	20	25	±
Water	1.5	10	10	±

3.1.1 Bone

Bone is a composite material that mainly consist of cells (osteoprogenitors, osteocytes, osteoblasts, osteoclasts) and matrix: organic (collagen, non-collagenous proteins, mucopolysacharides) and inorganic materials, namely calcium phosphates. The mineral matrix of the bone shows different porosity. Usually bone is composed of a relatively dense outer layer (Figure 3). The compact bone part is called *osteon* and *trabeculea* is a less dense spongy like bone. This is one of the most important feature of the bone and thus scaffold materials that should mimic host porosity. The calcium phosphate of the bone is an impure calcium hydroxyapatite crystals. In particular, about 4–6 % of phosphate are replaced by

carbonate groups, making the CHAp more carbonate apatite and are usually referred as “biological apatite” [73].

Figure 3. A noncalcined cancellous bone (femoral head) showing the transition from a more compact outer layer to a more porous interior [75].

3.1.2 Teeth

Enamel is the hardest tissue in the human body and hardly contains collagen. Enamel is an acellular tissue comprised of 80–90 vol. % (97 wt. %) carbonated hydroxyapatite crystals. The remaining consist of fluid and organic material [76]. The apatite crystal in enamel forms into needle-like rod and has a diameter approximately 5 μm. Additionally, the enamels’ surface contains small amount 0.01 wt. % of fluoride. Dentine is more alike to the bone, and contains 45 vol. % mineral phase, 30 – collagen and 25 – water. The main future of the dentine’s are tubules of approximately 1 μm width. The structure of tooth is shown in Figure 4.

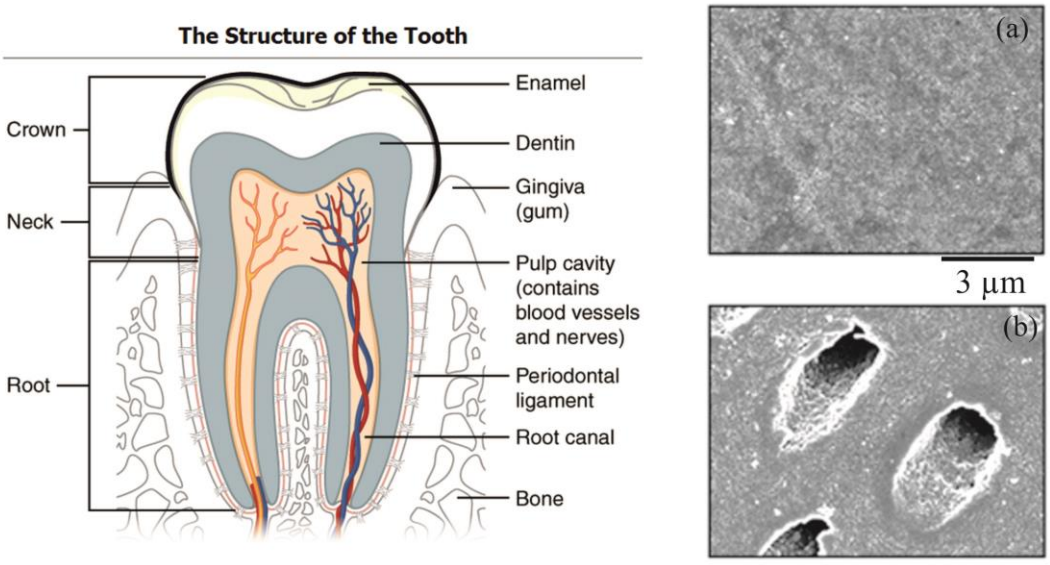

Figure 4. The structure of the tooth: on the left schematic view and on the right SEM image of enamel (a) and dentine (b) [77, 78].

3.2 SYNTHETIC CALCIUM HYDROXYAPATITE

Calcium hydroxyapatite (CHAp) with formula $Ca_{10}(PO_4)_6(OH)_2$ is very similar to inorganic mineral component of bone and teeth [79]. Apatites possess the general formula $Ca_{10}(PO_4)_6X_2$ where X is typically F (fluorapatite, FAp), OH (hydroxyapatite, CHAp), or Cl (chlorapatite, ClAp). The apatite lattice is very tolerant of substitutions, vacancies and solid solutions, for example, X can be replaced by $½CO_3$ or ½O; Ca by Sr, Ba, Pb, Na or vacancies; and PO_4 by HPO_4, AsO_4, VO_4, SiO_4 or CO_3. The ranking of the cations according to amount exchanged if found to be $Cd^{2+} \approx Zn^{2+} > Ni^{2+} > Ba^{+2} \approx Mg^{2+}$ [80].

The basic apatite structure is hexagonal with space group $P6_3/m$ and approximate lattice parameters a = 9.433Å and c = 6.880 Å. The crystal structure of CHAp is provided in Figure 5. A primitive unit cell contains 44 atoms. There are two crystallographically different Ca atoms, and three O atoms [81]. Ca(I) is coordinated to nine oxygen ions ($3O_a$, $3O_b$, $3O_c$) from six different phosphate

tetrahedral groups and Ca(II) is 7-fold coordinated by six oxygen ions of five phosphate groups and one from the hydroxyl group ($1O_a$, $1O_b$, $4O_c$, $1O_H$). The $Ca(I)O_9$ polyhedron is much bigger than $Ca(II)O_7$ polyhedron in volume (30 $Å^3$ vs. 22 $Å^3$) [82]. Considering different sites which Ca and O ions occupy, the CHAp molecular formula can be written as $Ca(I)_4Ca(II)_6(PO_aO_b(O_c)_2)_6(O_HH)_2$.

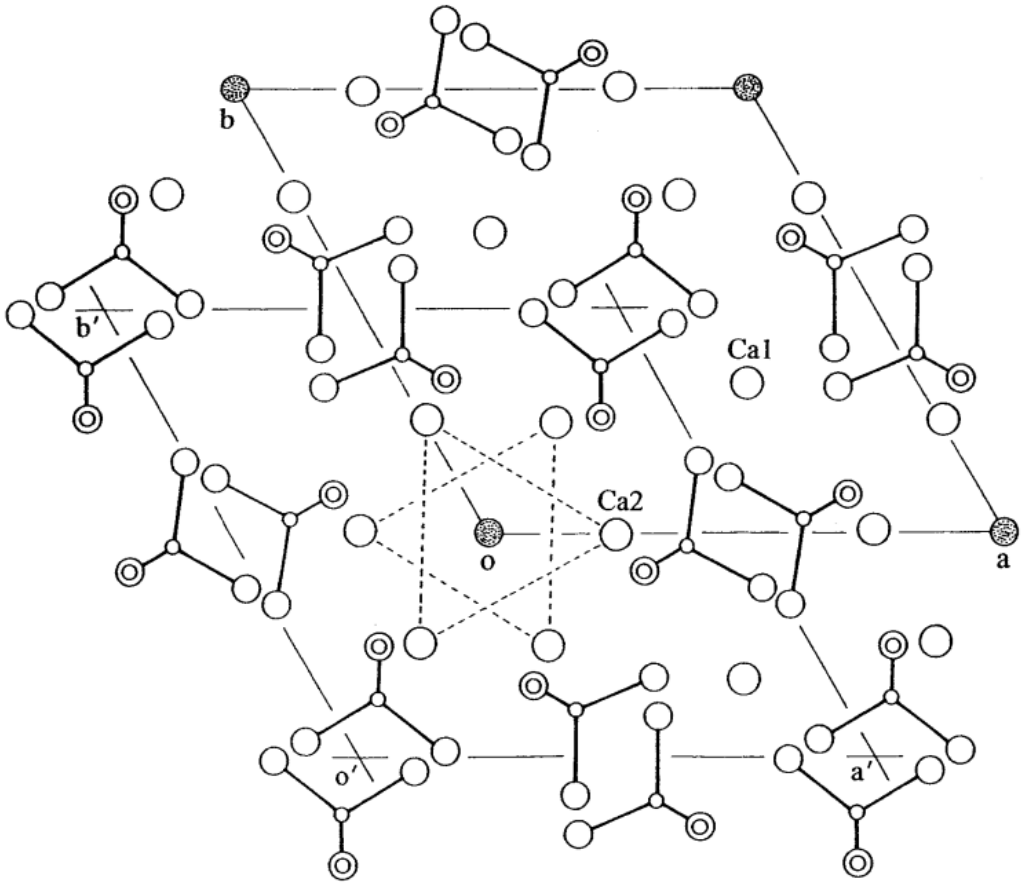

Figure 5. Crystal structure of FAp or hexagonal CHAp projected down the c-axis. The corners of the unit cell (marked by shaded circles) are occupied by F^- in FAp and by OH^- in CHAp. An alternate choice of unit cell is identified as a' and b'.

It is generally accepted that slightly nonstoichiometric CHAp has the hexagonal space group $P6_3/m$ structure, with a = 9.433 and c = 6.880 nm, while in the case of stoichiometric CHAp the structure becomes monoclinic $P2_1/b$ with the lattice

parameters a = 9.426 Å [51], b = 18.856 Å, c = 6.887 Å [53], and γ = 119.97 °. The structure is closely related to that of the hexagonal form, but with no restrictions imposed by the mirror symmetry. The Ca^{2+} and PO_4^{3-} ions occupy similar positions as in the hexagonal form. The OH^- ions are located in two different columns. However, the hexagonal form of CHAp is formed by precipitation from supersaturated solutions at 25 °C to 100 °C, while the monoclinic form of HAp is primarily formed by heating the hexagonal form at 850 °C in air and then cooling to room temperature. Figure 6 gives a closer look to the differences of hydroxyapatite crystal structure of space groups $P6_3/m$, $P6_3$ and $P2_1/b$.

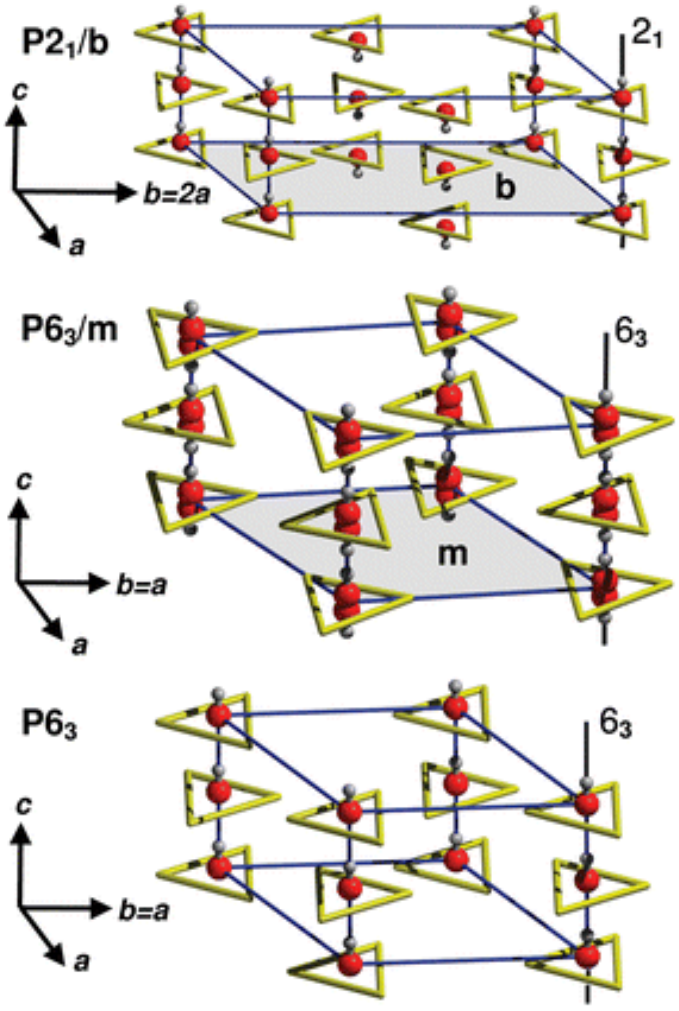

Figure 6. The proposed crystal structures of monoclinic (top), hexagonal (in the middle) and theoretical (bottom) CHAp structure [83].

3.2.1 Synthesis methods

Several methods have been employed for the synthesis of CHAp. This chapter will give you an overview on the conventional synthesis routes, such as wet and dry methods, and new methods, such as microwave, multiple emulsion and biomimetic techniques. Dry methods include solid-state and mechanochemical synthesis; wet approach includes chemical precipitations, sol-gel hydrolysis, hydrothermal, sonochemical and emulsion methods. CHAp can be synthesized in different pH ranges, from 4.2 pH and higher. Depending on the synthesis route, CHAp can possess various different properties: crystallinity, phase purity, grain size, morphology, microstructure and porosity [79, 84-90].

The main advantage of wet chemical synthesis is that its by-product consists primarily of water and the probability of contamination during processing is very low. The obtained CHAp particles have nanosized structure with regular morphology. The main disadvantages of wet methods are low crystallinity, due to low sintering temperature, that leads to other CaP phases beside CHAp. In addition, various ions can be incorporated in aqueous solutions. The most popular and well elaborated precipitation method was firstly proposed by *Tagai* and *Aoki* [91] as indicated *Bouyer at al.* Calcium hydroxide and orthophosphoric acid were precursors of this reaction (*equation 1*).

$$10\ Ca(OH)_2 + 6\ H_3PO_4 \longrightarrow Ca_{10}(PO_4)_6(OH)_2 + 18\ H_2O \quad (1)$$

The only byproduct was water. Unless the simplicity, this reaction is very sensitive to the temperature and orthophosphoric acid addition rate. It's strongly linked to the pH obtained at the end of the synthesis and affects size, shape and surface area of the CHAp. The favorable synthesis conditions of pure CHAp need a moderate acid addition rate coupled with a reaction temperature lower than 60 °C, this involves a reasonably high pH at the end of the reaction (pH > 10) [92]. *Hayek et al.* [93] disclosed the precipitation of hydroxyapatite using calcium nitrate

($Ca(NO_3)_2$) with diammonium hydrogen phosphate ($(NH_4)_2HPO_4$) in basic environment as shown in *equation 2*.

$$10\ Ca(NO_3)_2 + 6\ (NH_4)_2HPO_4 + 8NH_4OH \longrightarrow CHAp + 20\ NH_4NO_3 + 6\ H_2O \quad (2)$$

A solution of $Ca(NO_3)_2$ and $(NH_4)_2HPO_4$ in water were brought to pH ~11–12 with concentrated NH_4OH separately. The $(NH_4)_2HPO_4$ was then dropwise added to $Ca(NO_3)_2$ under vigorous stirring. White precipitations were washed and few times centrifuged. Resulting sludge was filtered, dried (at 90 °C) and sintered at 1000– 1200 °C. The grain size can be controlled by changing sintering temperature and reaction time [11].

Santos et al. has synthetized CHAp by three different aqueous precipitation routes as shown in *equations 3, 4* and *5* [94].

$$10\ Ca(OH)_2 + 6\ H_3PO_4 \longrightarrow CHAp + 18\ H_2O \quad (3)$$

$$10\ Ca(OH)_2 + 6\ (NH_4)_2HPO_4 \longrightarrow CHAp + 12\ NH_4OH + 6\ H_2O \quad (4)$$

$$7\ Ca(OH)_2 + 3\ Ca(H_2PO_4)_2H_2O \longrightarrow CHAp + 15\ H_2O \quad (5)$$

Synthesis (3) and (4) were carried out at 40 °C in order to improve $Ca(OH)_2$ dissolution and increase reaction kinetics, and synthesis (5) was performed at room temperature. Pure CHAp was prepared under stirring at room temperature, pH ~10 and Ca/P ratio 1,67. Crystallization started right after NH_4OH addition and allowed to grow for 24 h, afterwards sintered at 1000 °C for 1 h [95]. Janackovic et al. modified the homogeneous precipitation technique using hydrothermal reaction in $Ca(EDTA)^{2-}$ – Na_2HPO_4 solution:

$$Ca(edta)^{2-} + 3/5\ HPO_4^{2-} + 2/5\ H_2O \longrightarrow 1/10\ CHAp + H(edta)^{3-} + 1/5\ OH^- \quad (6)$$

The addition of urea instead of NaOH leads to more homogeneous formation of *monetite* and further transformation of CHAp, due to pH changes when urea hydrolysis occurs. The reaction temperature varied in the range of 125–160 °C [96].

Overall, precipitation techniques can produce small particles and high-purity CHAp powders. The important precipitation process variables include solution concentration (Ca/P ratio), pH, and acid addition rate, stirring speed, temperature, reaction time and atmospheric condition.

Calcium phosphates were synthesized by emulsion-precipitation method using glycerol, $Ca(OH)_2$ and H_3PO_4. During the synthesizing procedures, 0.5 M H_3PO_4 aqueous and 0.5M glycerol-$Ca(OH)_2$ suspension in distilled water were used. The H_3PO_4 was slowly added to the $Ca(OH)_2$ suspension at a rate of 30–40 ml/min until the Ca/P molar ratio reached 1.67. The reaction mixtures were vigorously stirred during the precipitation process, which proceeded at 37 °C. 1M tris-(hydroxymethyl)aminomethane and HCl solution were used to adjust the pH value. The resulting gelatinous precipitate was allowed to react for 24 h, washed three times in distilled water, and then lyophilized for 48 h. The as-synthesized powders were heated from 600 to 800 °C for 2 h. CHAp beads were obtained at 800 °C and remained stable till 1300 °C [97].

Hydrolysis method is mainly used to utilize other CaP phases into CHAp. The nano-sized CHAp powders were obtained using the hydrolysis of DCPD and $CaCO_3$ with 2.5 M NaOH at 75 °C for 1 h. The only product synthesized from DCPD is CHAp, and the crystallinity of the CHAp is improved with increasing annealing temperature up to 1000 °C. Authors have pointed out that dicalcium phosphate dihydrate ($CaHPO_4 \cdot 2H_2O$, DCPD) is thought to be one of the precursors of CHAp. The end product was obtained through the hydrolysis of DCPD based on the following reaction [98]:

$$10\ CaHPO_4 \cdot 2H_2O \longleftrightarrow CHAp + 18\ H_2O + 12\ H^+ + 4\ PO_4^{3-} \quad (7)$$

Hydrothermal synthesis is a process that utilizes single or heterogeneous phase reactions in aqueous media at elevated temperature (T > 25 ºC) and pressure (P > 100 kPa) to crystallize ceramic materials directly from solution [99, 100]. It might be considered as a simple chemical precipitation reaction in which the aging step is

conducted at higher temperature inside autoclave or pressure vessel. A facile urea-assisted hydrothermal synthesis and systematic characterization of hydroxyapatite with calcium nitrate tetrahydrate ($CaNO_3 \cdot 4H_2O$) and diammonium hydrogen phosphate ($(NH_4)_2HPO_4$) as precursors are reported. The main advantage is the simple and precise control of the CHAp crystals morphology by slow thermal decomposition of urea [101].

The growth of carbonated CHAp at hydrothermal conditions was reported [10]. These precursors were chosen: $CaHPO_4$, H_2O and CO_2 dry ice. The synthesis conditions were optimized: $CaHPO_4$ concentration was 10 g/l, temperature gradient – 33.5 °C/cm, heating rate – 0.005 °C/min, CO_2 concentration – 55 g/l. The biggest crystal was 12 mm × 200 μm × 400 μm. Ca/P ratio and CO_2 concentration in monocrystal were 1.60–1.67 and 0.09–0.65 wt. %, respectively. It was also observed that carbonate ions replace only hydroxyl groups. This synthesis was also utilized to obtain polycrystalline CHAp [96].

Monetite and CHAp have been synthesized by hydrothermal treatment of monocalcium phosphate monohydrate (MCPM) suspension at 160 and 200 °C. The monetite formed whiskers typically having length, diameter and aspect ratio in the range of 26–40 mm, 1–2 mm and 20–26, respectively and the hydroxyapatite shaped needle like crystals typically being in the range of 0.2–0.5 mm in length and 0.02–0.04 mm in diameter. The morphology of the crystals seems to be controlled mainly by the solubility of the reactant species. The phase of the hydrothermal product is determined by the combination of the pH and the Ca/P ratio of the aqueous solution [102].

Europium-doped hydroxyapatite nanoparticles were also synthesized by hydrothermal method. An aqueous solution of calcium nitrate ($Ca(NO_3)_2 \cdot 4H_2O$) and europium nitrate ($Eu(NO_3)_3$) was added dropwisely into ammonium hydrogen phosphate ($(NH_4)_2HPO_4$)) and arginine solution. The mole ratio of Ca/P should be 1.67. During the reaction at 60 °C, the solution was stirring and pH was maintained at 9.5 by using ammonia solution or urea. Afterward the solution was transferred

into an autoclave. The reaction was continued under the set solution temperature until completion. At the end of the experiment, the solids were collected by centrifugation (10 000 r/min) and filtration and then were washed using ethanol and dried overnight in vacuum conditions [103].

Silicon-substituted hydroxyapatite (Si-HA) with up to 1.8 wt. % Si content was prepared successfully by a hydrothermal method, using $Ca(NO_3)_2$, $(NH_4)_3PO_4$ or $(NH_4)_2HPO_4$ and $Si(OCH_2CH_3)_4$ (TEOS) as starting materials. Silicon has been incorporated in hydroxyapatite lattice by partially replacing phosphate (PO_4^{3-}) groups with silicate (SiO_4^{4-}) groups resulting in Si-CHAp described as $Ca_{10}(PO_4)_{6-x}(SiO_4)_x(OH)_{2-x}$. The reaction mixtures were stirred for 0.5 h followed by hydrothermal treatment at 200 °C for 8 h. The resulting precipitates were washed three times, and then dried at 100 °C for 12 h. A fraction of each as-prepared samples was treated at 800 °C for 1 h in air [104].

Sol-Gel approach is an effective method to synthetize nano-to-submicron particles with crystalline structure due to the strict control of process parameters. Many different calcium and phosphorus precursors used for sol-gel synthesis of CHAp. Selection of the synthesis route depends on the possible application of CHAp [105-107]. Besides, bioactivity of Ca–P based materials is dependent on many factors such as the synthesis procedure, precursor reagents, impurity contents, crystal size and morphology, concentration and mixture order of reagents, pH and temperature. Balamurugan et al. [108] used $CaNO_3 \cdot 4H_2O$ and triethyl phosphate as calcium and phosphorus precursors respectively, and the stoichiometry was strictly 1.67. The pure CHAp was obtained after calcination the gel at 900 °C. While Brendel et al. [109] have synthetized CHAp at low temperature (400 °C), however, the material showed low purity and poor crystallinity. They used $CaNO_3 \cdot 4H_2O$ and phenyl dichlorphosphite as precursors. By increasing the annealing temperature to 900 °C well-crystallized and pure CHAp was obtained. Takahashi et al. [110] also used $CaNO_3 \cdot 4H_2O$ as Ca precursor and the P precursor was phosphonoacetic acid $[HOOCCH_2PO(OH)_2]$. CHAp was synthetized in aqueous solution after heat

treatment of the gel 700 °C. Although, the crystallinity was improved after increasing the sintering temperature up to 1100 °C. There were more reports on the same conclusion that the CHAp crystallinity can be improved by increasing the sintering temperature [110-112].

The alkoxide based sol-gel synthesis approaches have been also reported [113-116]. The different variations of sol-gel technique were elaborated. The EDTA [117-119] and citric acid [120, 121] were used as complexing agents. The Ca–P–O gels were synthesized using $CaNO_3 \cdot 4H_2O$ – ethanol solution of pH = 10.5 and afterwards mixed with diammonium hydrogen phosphate [122, 123]. P_2O_5 dissolved in absolute ethanol [124], triethanol phosphite or triethanol phosphate [125, 126] were also used as P source. Good quality CHAp coatings by non-aqueous sol-gel technique using calcium 2-ethylhexanoate and tricalcium phosphate or other starting materials [127] were produced.

Dry synthesis methods do not use a solvent, unlike wet methods. The characteristics of a powder synthesized by a dry method are not strongly affected by the processing parameters, and most dry methods do not require precisely controlled conditions, making them suitable for mass production of powders. A number of researchers have therefore adapted well-known dry methods, including solid-state synthesis and the mechanochemical process. In the conventional solid state reactions method of preparation CHAp the precursors were $CaCO_3$, $CaHPO_4 \cdot 2H_2O$, $Ca_3(PO_4)_2$, $Ca(OH)_2$, P_2O_5, $(NH_4)H_2PO_4$ [110, 128, 129]. In a typical procedure, precursors are first milled and then calcined at high temperatures above 1000 °C that lead to well-crystallized structures. Unfortunately, powders usually exhibits heterogeneity having irregularly shaped micron-size grains. This method suffers from the small diffusion of ions during the layer of reaction products. For improving it, some researchers have used an alternative approach known as mechanochemical method in a dry manner. Typically, materials in necessary stoichiometry are grounded in planetary mill.

Hydroxyapatite powders were synthesized using calcium pyrophosphate ($Ca_2P_2O_7$) and calcium carbonate ($CaCO_3$) through the solid state reaction. The presence of water in the solid state reaction is crucial. The results were explained in terms of the mechanochemical reaction that could supply enough amount of hydroxyl groups to the starting powders to form a single CHAp phase [130]:

$$3Ca_2P_2O_7 + 4\ CaCO_3 \rightarrow 3\ Ca_3(PO_4)_2 + CaO + 4\ H_2O \quad (8)$$

$$3Ca_2P_2O_7 + 4\ CaCO_3 + x\ H_2O \rightarrow x\ CHAp + 3(1-x)Ca_3(PO_4)_2 + 4CO_2 \quad (9)$$

$$3Ca_2P_2O_7 + 4\ CaCO_3 + x\ H_2O \rightarrow CHAp + (x-1)H_2O + 4CO_2 \quad (10)$$

Kim et al. [131] performed mechanochemical synthesis of CHAp from $Ca(OH)_2$ –P_2O_5 and CaO–$Ca(OH)_2$–P_2O_5 mixture with a Ca/P molar ratio of 1.67. CHAp was obtained after 30 min. grinding using a planetary ball mill at room temperature. It is stated that $Ca(OH)_2$-P_2O_5 system favorable towards CHAp formation, and water also plays vital role for the formation of phase. The reaction mechanism was determined and described:

$$10\ Ca(OH)_2 + 3P_2O_5 \rightarrow 6\ H_3PO_4 + 9\ CaO + Ca(OH)_2 \quad (11)$$

$$6\ H_3PO_4 + 9\ CaO + Ca(OH)_2 \rightarrow 6\ CaHPO_4 + 4\ Ca(OH)_2 + 3\ H_2O \quad (12)$$

$$6\ CaHPO_4 + 4\ Ca(OH)_2 + 3\ H_2O \rightarrow CHAp + 9\ H_2O \quad (13)$$

Multiply emulsion technique for the synthesis of CHAp was developed by Kimura [132]. The multiple emulsion was made of dipotassium hydrogen phosphate solution as an inner aqueous phase, benzene as an oil phase, and calcium nitrate solution as an outer aqueous phase. The interface reaction was carried out at ~50 °C for 24 h and at the pH = 12 of the inner aqueous phase. Final product was composed of spherical particles of ~3 μm in size.

Electrodeposition technique was used to obtain an ultrafine-grained, nanophase CHAp coatings from dilute electrolytes of $Ca(NO_3)_2$ and $NH_4H_2PO_4$.

Electrodeposition was carried out at physiological pH, and sodium nitrate was used to enhance the electrolytes ionic strength [133].

Biomimetic deposition technique was used to synthetize nanosized, carbonated and "bone-mimic" CHAp at physiological pH and temperature using $Ca(NO_3)_2 \cdot 4H_2O$ and $(NH_4)_2HPO_4$ dissolved in synthetic body fluid (SBF). The average grain sizes of these powders after sintering remained sub-microne [134].

Hydroxyapatite nanorods, bowknot-like and flower-like nanostructures have been directly synthesized under microwave irradiation. In the synthesis of CHAp, high-purity $CaNO_3 \cdot 4H_2O$ and Na_2HPO_4 were used as the starting materials. EDTA served as the complexing reagent. NaOH was used to adjust pH to 9–13. Clear aqueous solution was put into the household type microwave oven of 700 W power for 0.5 h and later washed with deionized water. The crystal morphology depends on the pH: CHAp nanorods with typical width of 150 nm and lengths up to 1–2 μm were formed at pH = 11; leaf-like flakes of 150–200 nm width and of 1–2 μm length prepared in the solution of pH = 13 [135]. In the microwave-assisted synthesis of pure CHAp and Si-substituted CHAp, $Ca(NO_3)_2 \cdot 4H_2O$, $(NH_4)_2HPO_4$ and $Si(OCH_2CH_3)_4$(-TEOS) were used as the starting reagents. The amount of reagents was calculated according on the assumption that silicate would substitute phosphate. Ammonium hydrogen phosphate $(NH_4)_2HPO_4$ was dissolves in water, the pH of the solution was kept higher than 11 by the addition of NH_4OH. To this appropriate amount of hydrolyzed TEOS (dil. HNO_3 used as catalyst) solution was added and stirred. A 0.25 M solution of $Ca(NO_3)_2 \cdot 4H_2O$ added to the above solution and the reaction mixture was stirred for 0.5 h keeping the pH above 11. A suspension of precipitated hydroxides were obtained and irradiated with microwaves at 900 W for 0.5 h using a programmable microwave oven. The resulting precipitates were filtered, dried at 70 °C overnight. The dried powders were ground using in a mortar and subsequently calcined at 900 °C for 2 h in air [136].

A mixture of 6 mol of $CaHPO_4 \cdot 2H_2O$ and 4 mol of $Ca(OH)_2$ was reacted to produce hydroxyapatite by spark plasma system (SPS). The reaction was carried out at 300–1200 °C under pressure of 20–670 MPa for 10 min in a vacuum. CHAp formation started at 300 °C at 600 MPa and was completed at 500 °C at 670 MPa. The same product being obtained at 1200 °C in air using a furnace. The temperature of the CHAp formation increased with decreasing pressure and was 1150 °C under 20 MPa. There was a linear relationship between the reaction temperature and pressure. The crystal size of the CHAp prepared at 500 °C at 670 MPa and that at 600 °C at 600 MPa by SPS were less than 1 and 2 mm, respectively [137].

The hydroxyapatite has been produced in a sonicated pseudo-body solution. The sonication time (15 min sonication resulted in the most pure hydroxyapatite phase) was found effective in the formation of nanoparticles. Also it was shown that growth temperature is a crucial factor and hydroxyapatite crystallizes only at 37 °C. The particles formed by sonication were generally smaller and more spherical than those obtained without sonication. Sonication increased the hydroxyapatite crystal growth rate up to 5.5 times compared to non-sonication conditions. The comparison between the specific surface areas of hydroxyapatite nanoparticles obtained by sonication and without sonication demonstrated that sonication increased the specific surface area from 63 m^2/g to 107 m^2/g and decreased the size of nanoparticles from 30 nm to 18 nm [138].

3.2.2 Substitution effects

CHAp is capable of accommodating several substituents, while still maintaining its basic apatitic structure. Ca^{2+} can be substituted by various cations, such as, monovalent (Na^+, K^+), divalent (Mg^{2+}, Sr^{2+}, Ba^{2+}, Pb^{2+}) and trivalent (Y^{3+}) cations [80]. Significant anionic substitutions, include the replacement of OH^- by CO_3^{2-}, F^-, Cl^-, and PO_4^{3-} by CO_3^{2-}, AsO_4^{3-} and VO_4^{3-}. Some substitutions are coupled with

others to maintain the charge balance in the apatite, such as, CO_3^{2-} for PO_4^{3-} coupled with Na^+ for Ca^{2+} [139]. Possible substitutions for each sublattice listed in Table 5.

Table 5. The possible chemical compositions of apatite structures.

$M_{10}(ZO_4)_6X$	
M	Ca^{2+}, Sr^{2+}, Fe^{3+}, Al^{3+}, Cr^{3+}, La^{3+}, Ba^{2+}, Cd^{2+}, Mg^{2+}, Na^3, K^+, H^+, D^+
ZO_4	PO_4^{3-}, CO_3^{2-}, SiO_4^{4-}, VO_4^{3-}, AsO_4^{3-}
X	OH^-, CO_3^{2-}, O^{2-}, BO_2^-, Cl^-, F^-, Br^-, vacancies

Substitutions influence CHAp characteristics, such as the degree of crystallinity, morphology, lattice parameters, the stability of CHAp structure, and ultimately it exhibit different mechanical properties, as well as influence the biological response in the final applications. As bone minerals are considered to be Ca-deficient, thus non-stoichiometric minerals, with many incorporations within the apatitic lattice, it is rational to modify synthetic CHAp and achieve desirable properties, such as solubility, osteoconductivity and bioactivity.

Zinc, as the most abundant trace metal in bone mineral, is an essential element that has stimulatory effects on bone formation in vitro and in vivo as well as inhibitory effects on osteoclastic bone resorption in vivo. It can also promote bone metabolism and growth, increase bone density and prevent bone loss. Synthesis of Zn-substituted CHAp nanocrystals as an alternative material in autograft and allograft bone replacements is an interesting objective in biomaterials research [140]. Typically Zn-CHAp have been synthesized by using the reagents of $Ca(NO_3)_2$, $CaCl_2$, $(NH_4)_3HPO_4$, and $Zn(NO_3)_2$. Thus some incorporations of NO_3^- or Cl^- into the apatite structure are available. Miyaji and co-workers employed $Ca(CH_3COO)_2 \cdot H_2O$, $Zn(CH_3COO)_2 \cdot 2H_2O$, and $(NH_4)_2HPO_4$ as chemical reactants to prepare Zn-CHAp samples via precipitation method. The substitution amount is ~15–20 at. % as the apatite structure does not sustain higher Zn incorporation [139, 141].

Magnesium is known to be an important trace element in bone and teeth. Indeed, despite its low concentration (generally between 0.5 and 1.5 wt. %), it plays a key role in bone metabolism, in particular during the early stages of osteogenesis where it stimulates osteoblast proliferation, and its depletion causes bone fragility and bone loss [142]. Mg-CHAp was found to exhibit the highest release of ions into the culture medium and the highest relative cell densities were found on Mg-CHAp and Zn-CHAp. Unfortunately the most cell apoptosis was also found on Mg-CHAp although cell viability was good [79].

It was suggested that the smaller and less perfect CHAp crystals with the higher Mn content should be more resorbable thus more biocompatible. The coatings of Mn-doped carbonated CHAp on Ti substrates was found to promote human osteoblast proliferation, activation and differentiation [139, 143]. The Mn^{2+} ions has an inhibitory effect on CHAp crystallization. Mn^{2+} enters the structure of β-TCP more easily than CHAp.

Sr-CHAp beneficial of low doses of Sr in the treatment of osteoporosis has been known and recently has been shown to reduce the incidence of fracture in osteoporotic patients [139]. Sr can replace Ca in the structure of CHAp over the whole range of composition as it has similar ionic radius. However, Sr concentration in the range of 3–7 at. % significantly stimulates osteoblasts activity and differentiation, moreover, even 1 at. % Sr substitution is sufficient to affect osteoclast proliferation, which reduces with increasing Sr content.

Silver presenting in the hydroxyapatite increases the solubility of the apatite as well as reduces the thermal stability. A preliminary in vitro study found that the silver ions leeching out of the apatite led to an antimicrobial effect on E. coli [79]. Photo-stimulated luminescence of biocompatible materials is an appealing approach in observing the distribution of bioactive compounds in surgery, tissue engineering or bone re-modelling [144]. It was demonstrated that Ce^{3+} containing CHAp exhibits also antibacterial properties. The improved antibacterial effects of

Ce-CHAp nanoparticle on *Lactobacillus* showed its potential ability to anti-caries [145].

The optical properties of compounds with apatitic structure have been studied as well. The Sb^{3+} and Mn^{2+} co-doped fluorapatite was applied in fluorescent lamps. Activated by trivalent rare earth (RE^{3+}) ions, such as Nd^{3+}, Yb^{3+}, Er^{3+}, Pr^{3+}, Tb^{3+} and Eu^{3+}, apatites exhibited favorable spectroscopic properties for use in laser applications [146].

Silicon in particular has been found to be essential for normal bone and cartilage growth and development. Synthetic CaP-based materials that include trace levels of Si in their structures can improve the bioactivity of hydroxyapatite in the same way that it influences the bioactivity of bioactive glasses and glass-ceramics [104, 136]. The CO_3-CHAp could be named as biomimetic CHAp as the bone contains significant content of carbonate ions. Carbonate substitution can occur on two atomic sites within the hydroxyapatite lattice: A type (substitution of hydroxyl ions for carbonate ions) and B-type (substitution of phosphate ions for carbonate ions). The B-type substitution is the preferential carbonate substitution found in the bone [79]. Fluoroapatites have been produced with the fluorine ions substituting for the hydroxyl groups in the CHAp lattice. Substituting fluorine into the CHAp lattice increases crystallinity, decreases solubility and improves thermal stability. F-CHAp is known to delay caries and enhance mineralization process [79, 147]. It has been suggested that this effect is due to the formation of hydroxy-fluorapatite in teeth, which has a higher acid resistance than CHAp [148].

3.3 CALCIUM ORTHOPHOSPHATES

Calcium orthophosphates might be classified into three major structural types: (1) the apatite type, $Ca_{10}(PO_4)_6X_2$, which includes CHAp, CFAp, CDHA, OCP and TTCP; (2) the glaserite type, named after the mineral glaserite, $K_3Na(SO_4)_2$, which includes all polymorphs of TCP and, perhaps, ACP; (3) the $Ca–PO_4$ sheet-containing compounds, which include DCPD, DCPA, MCPM and MCPA.

MCPM is both the most acidic and water-soluble compound. It precipitates from highly acidic solutions. At temperatures above 100 ºC, it releases a molecule of water and transforms into MCPA. Due to high acidity and solubility, MCPM is never found in biological calcifications. Moreover, pure MCPM is not biocompatible with bone. However, MCPM is used in medicine as a component of several self-hardening calcium orthophosphate cements. Occasionally, MCPM is added to toothpastes. MCPA is the anhydrous form of MCPM. It crystallizes under the same conditions as MCPM. MCPA also never appears in calcified tissues and is not biocompatible due to its acidity. There is no current application of MCPA in medicine; its hydroscopic properties reduce its commercial applications. DCPD can be easily crystallized from aqueous solutions at pH < 6.5. It transforms into DCPA at temperatures above 80 ºC. DCPD is of biological importance because it is often found in pathological calcifications (dental calculi, crystalluria, chondrocalcinosis and urinary stones) and some carious lesions. In medicine, DCPD is used in calcium orthophosphate cements and as an intermediate for tooth remineralization. DCPD is added to toothpaste both for caries protection (in this case, it is coupled with F^- containing compounds such as NaF and/or Na_2PO_3F) and as a gentle polishing agent. DCPA is the anhydrous form of DCPD. It is less soluble than DCPD due to the absence of water inclusions. DCPA can be crystallized from aqueous solutions at 100 ºC. Unlike DCPD, DCPA occurs in neither normal nor pathological calcifications. It is used in calcium phosphate cements. Other applications include uses as a polishing agent and a toothpaste component. Tri-calcium phosphate (TCP) has four polymorphs: α; β; γ; and super α. The γ polymorph is a high pressure phase, and the super α polymorph is observed at temperatures above ~1500°C. Therefore, the most common polymorphs in bioceramics are α- and β-TCP. The β-form of TCP is thermodynamically stable at room temperature, and its stability ranges between 25 °C and 1120 °C; while α-TCP is thermodynamically stable between 1140 and 1470 °C. At temperatures above ~1125 ºC, β-TCP transforms into a high-temperature phase α-TCP. Being the stable phase at room temperature, β-TCP is

less soluble in water than α-TCP. The β-form has better reactivity with the surrounding tissues compared with α-TCP. In combination with CHAp, β-TCP forms a biphasic calcium phosphate (BCP). Both β-TCP and BCP are widely used as a bone substitution bioceramics and α-TCP – as bone cements. Pure β-TCP is added to some brands of toothpaste as a gentle polishing agent. β-TCP is an efficient bioresorbable ceramic, whereas α-TCP is the major constituent of bioactive pastes applied as bone filling materials. The "silicon stabilized α-TCP" is used as a starting material to produce bioresorbable porous ceramic scaffolds. Pure α-TCP and β-TCP never occur in biological calcifications. Only the Mg-substituted β-TCP is found in dental calculi and urinary stones, dentinal caries, salivary stones, arthritic cartilage, as well as in some soft-tissue deposits. OCP is often found as an unstable transient intermediate during the precipitation of the thermodynamically more stable calcium orthophosphates in aqueous solutions. The full hydrolysis of OCP into CDHA occurs within 6 h. A similarity in the crystal structures of OCP and CHAp is the reason that the epitaxial growth of these phases is observed. OCP is of a great biological importance because it is one of the stable components of human dental and urinary calculi. It plays an important role in *in vivo* formation of apatitic biominerals. In surgery, OCP is used for implantation into bone defects. ACP is often encountered as a transient phase during the formation of calcium orthophosphates in aqueous systems. ACP is thought to be formed at the beginning of the precipitation due to a lower surface energy than that of OCP and apatites. The chemical composition of ACP strongly depends on the solution pH and the concentrations of mixing solutions. Biologically it is found in soft-tissue pathological calcifications. In medicine, pure ACP is used in calcium orthophosphate cements and as a filling material in dentistry. CDHA can be easily prepared by simultaneous addition of calcium and orthophosphate-containing solutions into boiling water, followed by boiling the suspension for several hours. During this time, the initially precipitated ACP is restructured and transformed into CDHA. Therefore, there are many similarities in the structure, properties and

application between the precipitated in alkaline solutions (pH > 8) of ACP and CDHA. On heating above 700 ºC, dry CDHA with Ca/P = 1.5 will convert to β-TCP and that with 1.5 < Ca/P < 1.67 will convert into a mixture of HA and β-TCP (biphasic calcium phosphate - BCP). Due to a lack of stoichiometry, CDHA usually contains other ions. Unsubstituted CDHA does not exist in biological systems. The ion-substituted CDHA (Na^+, K^+, Mg^{2+}, Sr^{2+} for Ca^{2+}; CO_3^{2-} for PO_4^{3-} or HPO_4^{2-}, F^-, Cl^-, CO_3^{2-} for OH^-) plus some water forms biological apatite – the main inorganic part of animal and human normal and pathological calcifications. Therefore, CDHA is a very promising compound for industrial manufacturing of artificial bone substitutes. TTCP is the most basic calcium orthophosphate. However, its solubility in water is higher than that of CHAp. TTCP is not very stable in aqueous solutions: it slowly hydrolyses to CHAp and calcium hydroxide and consequently, TTCP is never found in biological calcifications. In medicine, TTCP is widely used for the preparation of various self-setting calcium phosphate cements [20, 84, 149-153]. It was claimed that CHAp loses its OH^- groups gradually and transforms into oxyapatite at 1200 °C. When being heated to 1450 °C, oxyapatite was found to decompose into β-TCP, $Ca_2P_2O_7$ and $Ca_4P_2O_9$ [154].

The most widely studied CaP ceramics are TCP, CHAp, and tetracalcium phosphate (Figure 7) [155]. It is important to mention that secondary phase of CaO has been demonstrated to be harmful to the biocompatibility of CHAp [156, 157].

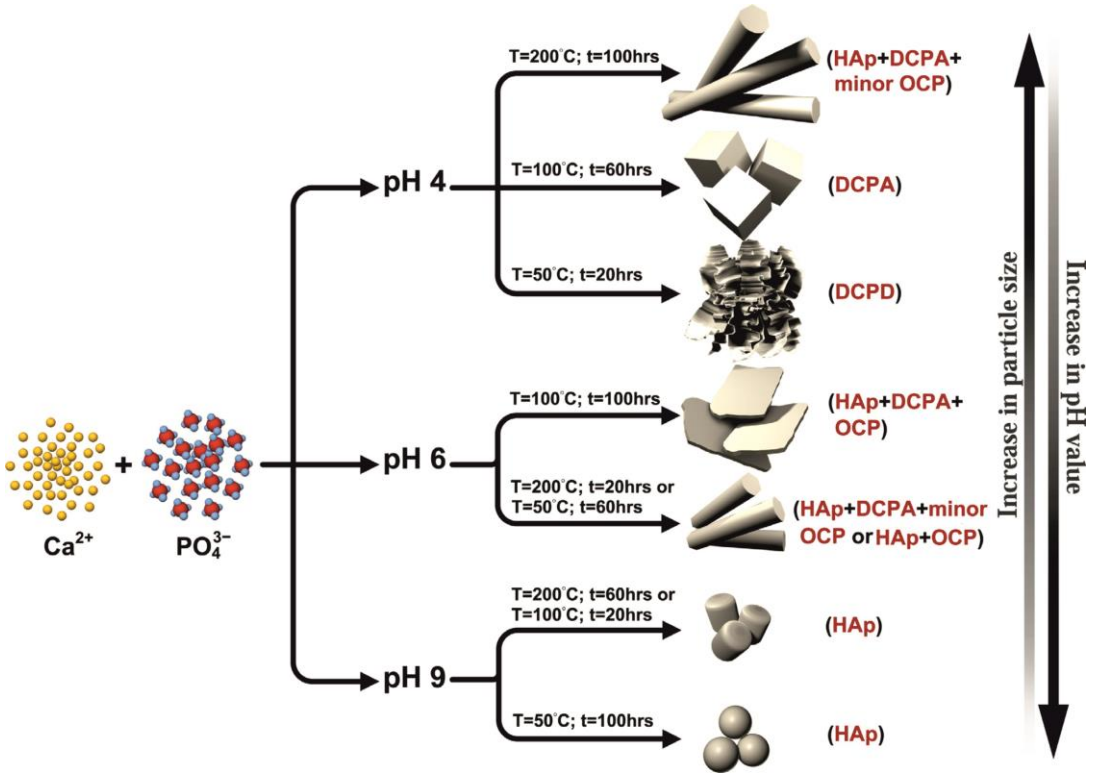

Figure 7. Effect of pH, temperature and duration of hydrothermal treatment on phase purity, morphology, and particle size of the CaP powder [156].

All calcium phosphate ceramics biodegrade. The rate of biodegradation increases as surface area increases, crystallinity decreases, crystal perfection decreases, crystal and grain size decrease, and if there are ionic substitutions of CO_2^{-3}, Mg^{2+}, and Sr^{2+} in CHAp. Factors that tend to decrease the rate of biodegradation include: (1) F^- substitution in CHAp; (2) Mg^{2+} substitution in β-TCP; and (3) lower β-TCP/CHAp ratios in biphasic calcium phosphates [5]. The degree of crystallinity of calcium phosphates influences osteoblastic differentiation, and CHAp with low crystallinity was shown to exhibit higher level of mineralization, and greater Ca release [158].

Bioceramics made of dense CHAp would be a good example of a bioactive material, while porous scaffolds made of BCP (i.e., β-TCP + CHAp, α-TCP + CHAp) or bone grafts made of CDHA and/or ACP appear to be the examples of

bioresorbable materials. Calcium orthophosphates (both non-substituted and ion-substituted) fall into the categories of bioactive and bioresorbable materials [152]. Table 6 presents composition of various phases of calcium phosphates [20, 150, 159-163].

Table 6. Calcium phosphates with corresponding Ca/P ratio.

Compound	Formula	Ca/P ratio
Monocalcium phosphate anhydrous (MCPA)	$Ca(H_2PO_4)_2$	0.5
Monocalcium phosphate monohydrate (MCPM)	$Ca(H_2PO_4)_2 \cdot H_2O$	0.5
Dicalcium phosphate dehydrate (DCPD), mineral brushite	$CaHPO_4 \cdot 2H_2O$	1.0
Dicalcium phosphate anhydrous (DCPA), mineral monetite	$CaHPO_4$	1.0
Octacalcium phosphate (OCP)	$Ca_8(HPO_4)_2(PO_4)_4 \cdot 5H_2O$	1.33
α-Tricalcium phosphate (α-TCP)	$\alpha\text{-}Ca_3(PO_4)_2$	1.5
β-Tricalcium phosphate (β-TCP)	$\beta\text{-}Ca_3(PO_4)_2$	1.5
Amorphous calcium phosphate (ACP)	$Ca_xH_y(PO_4)_z \cdot nH_2O$, n = 3–4,5; 15–20% H_2O	1.2–2.2
Calcium deficient hydroxyapatite (CDHA)[(1)]	$Ca_{10-x}(HPO_4)_x(PO_4)_{6-x}(OH)_{2-x}$[(2)] (0<x<1)	1.51–1.67
Hydroxyapatite (CHAp or HA)	$Ca_{10}(PO_4)_6(OH)_2$	1.67
Fluorapatite (CFAp or FA)	$Ca_{10}(PO_4)_6F_2$	1.67
Tetracalcium phosphate (TTCP ot TetCP), mineral hilgenstockite	$Ca_4(PO_4)_2O$	2.0

[(1)] Occasionally, CDHA is named as precipitated CHAp

[(2)] In the case x=1 (Ca/P = 1.5), the chemical formula is $Ca_9(HPO_4)(PO_4)_5(OH)$.

CHAPTER 4 ALUMINOSILICATES

This chapter will provide you an overview on the aluminosilicates that are used in dentistry and optics.

4.1 FELDSHPATHS IN DENTISTRY

Since the basic development of Weinstein *et al.* in 1962 [164], dental ceramics can generally be fused to various metal alloys. The CTE of these materials heavily depends on the content of leucite ($KAlSi_2O_6$) that has been identified by many authors as the main crystalline phase in the standard dental porcelain. CTE of tetragonal leucite (low-temperature form) is close to 22.3×10^{-6}/°C [165, 166]. Leucite containing porcelains (17–25 mass %) were first developed in the early 1960s for metal-ceramic systems, taking advantage of earlier observations regarding the role of crystalline leucite in the nonlinear thermal expansion of high-potassium feldspar ($KAlSi_3O_8$) glasses. Leucite raises the composite coefficient of thermal expansion of the porcelain (to match that of casting alloys) owing to both its high thermal expansion coefficient and its martensitic tetragonal-cubic transition (400–500 °C) [2]. Leucite is also added for dispersion strengthening at concentrations 40 to 55 mass %. In a nutshell, beyond thermal expansion/contraction behavior, leucite possess refraction index close to feldshpathic glass (important for translucency), and creates multiple tiny features for resin to enter and make good micromechanical bond [167].

IPS Empress ceramic contains leucite crystals only a few microns in size that are produced by means of controlled crystallization with special glass-containing nucleating agents. The leucite crystals are the crystalline component (35–55%) of the feldspathic rock used in dental porcelains [168].

The combination of two different crystal phases was achieved in glasses from the SiO_2–Al_2O_3–K_2O–Na_2O–CaO–P_2O_5–F system [169]. IPS d.SIGN (Ivoclar Vivadent AG, Schaan, Liechtenstein) is a new type of feldspathic-based ceramic

containing dispersed fluorapatite ($Ca_{10}(PO_4)_6F_2$) and leucite crystals ($K_2O \cdot Al_2O_3 \cdot 4SiO_2$) in a feldspathic glassy matrix. The chemical composition of leucite-fluorapatite ceramic is: SiO_2 50–65, Al_2O_3 8–20, Na_2O 4–12, K_2O 7–13, CaO 0.1–0.6, P_2O_5 0.0–0.5, F 0.1–3.0 (in wt. %). Fluorapatite crystals, 2−5 μm in length and 0.3 μm in diameter of needle-like morphology, are known to be enclosed in natural bone and teeth [170].

Fredericci et al. [171] has determine the effect of temperature and heating rate on the densification of four leucite-based dental porcelains: two low-fusion (Ceramco Finesse and Ivoclar) and two high-fusion commercial porcelains (Ceramco I and Ceramco II). In clinical dentistry, it is very important to obtain dental restorations that are as dense as possible, since this will lead to better clinical performance on the long term. No significant difference in densification was observed by increasing the heating rate from 10 °C /min to 55 °C /min, for low-fusing (800 °C and 875 °C) and high-fusing (1000 °C) porcelains.

Based on the microstructure, dental ceramics fall within three basic classes. (1) Predominantly glassy ceramics best mimic the optical properties of enamel and dentine. These glasses are derived from feldspar group and are based on silicon oxide and aluminum oxide (hence – aluminosilicates). The 3-D network of bridges formed by Si–O–Si bonds is broken up by modifying cations that provide non bridging oxygen atoms. This group of glasses are resistant to crystallization. (2) Particle-filled glasses contain either crystalline phase or higher melting glasses in order to improve mechanical properties and optical effects. Common crystalline phase is leucite that allows create porcelains fired (fused) onto metal substrates. (3) Polycrystalline ceramics have no glassy components thus are the densest. Sadly, those are highly opaque and must be veneered with glassy ceramics to bring the pleasing aesthetics [167].

4.2 LEUCITE

Leucite $KAlSi_2O_6$ is a characteristic mineral of young volcanic rocks, relatively poor in silica and rich in potassium. It forms by incongruent melting in feldspathic glasses having a K_2O content higher than approximately 12 mass %. The crystal structure of leucite is based on the isometric aluminosilicate framework of the ANA (ANA – Analcime, irregular distorted 8-rings [172]) topology, which is typical for analcime, pollucite [173], wairakite and some other natural and synthetic compounds. The main secondary building units (SBU) of this framework are four- and six-membered rings of $[(Al,Si)O_4]$ tetrahedra. Potassium atoms are situated in the W positions with the 6 + 6 coordination. The S positions are vacant and blocked by potassium atoms in leucite. A system of channels can be recognized in the framework along [001] direction bounded by strongly distorted eight-membered rings [174, 175]. Natural leucite crystallizes at high temperature in a cubic form, space group Ia3d. Below 665 °C it transforms to tetragonal phase and at room temperature leucite has space group $I4_1/a$ [176]. The differences between two leucite polymorphs are shown in Figure 8. Transition temperatures vary from sample to sample, but the transition of cubic leucite (point group, *m3m*) to tetragonal (point group, *4/mmm*) is at about 665 °C. The transition to the *4/m* form occurs at about 630 °C. Palmer *et al*. measured the cell parameters with temperature, to illustrate thermal contraction and phase changes with decreasing temperature [177].

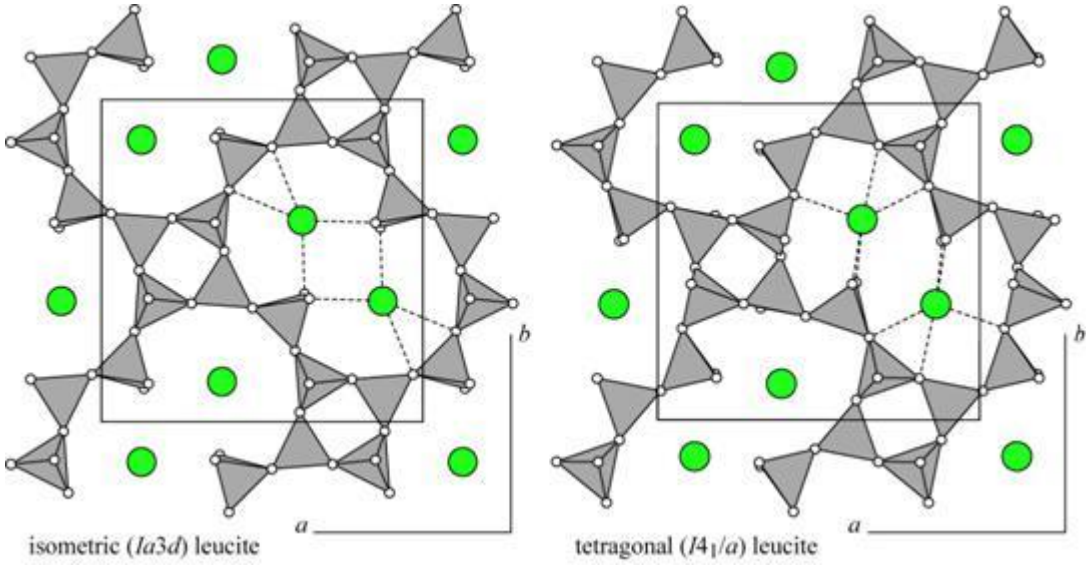

Figure 8. The differences between two leucite polymorphs [178].

The synthesis of monophasic leucite powders is an attractive subject and it was done by co-precipitation, salt bath, sol-gel, hydrothermal and solid state methods. Leucite has high melting point 1693 °C [179], which makes the synthesis of pure leucite at relative low temperature difficult. Moreover, kalsilite and glass phase are the common impurities of chemically derived leucite. Besides, sanidine can also crystallize from the leucite dental porcelain after multiple firing, which may cause a negative effect on the mechanical and esthetic properties of dental porcelain [180-182].

Zhang et al. [183] have prepared leucite and dental porcelain. Hydrothermally derived leucite was prepared from silica sol, $Al(NO_3)_3 \cdot 9H_2O$, and KNO_3. The HNO_3 was added to silica sol (pH~1–2) and mixed with aluminum and potassium nitrates according to stoichiometry K/Al/Si at ratio 1:1:2. Urea was added to mixture (urea/$Al(NO_3)_3$ ratio 2:1) before autoclaving. Reaction was carried out at 200 °C for 3 h and product was sintered at 1100 °C to obtain leucite. The porcelain was prepared from frit (wt. %): 59 % SiO_2, 13 % Al_2O_3, 9 % K_2O, 10 % Na_2O, 2 % CaO, 2 % CeO, 1.5 % Li_2O, 1 % CaF, 2,1 % MgO, 1 % BaO and 0.5 % ZrO_2. A mixture of 20 mass % leucite and 80 mass % low fusing temperature frit was ball-milled in ethanol for 1 h and heated to 850 °C at 60 °C/min rate.

The crystallization of leucite from frits are reported in [184-187]. The composition of the starting glass was wt. %: 64.2 % SiO_2, 16.1 % Al_2O_3, 10.9 % K_2O, 4.3 % Na_2O, 1.7 % CaO, 0.5 % Li_2O and 0.4 % TiO_2. Fine leucite crystal with size 1.2 μm^2 was obtained after sintering. Crystal and matrix microcracking have been linked to the cubic to tetragonal leucite transformation when the unit cell expands in the c-axis and contracts in the a-axis, with a resultant anisotropic stress distribution. A leucite particle diameter of less than 4 μm recommended to minimize microcracking in leucite containing dental porcelain [188]. Fine leucite powders with average particle size of 0.2 μm were synthetized by low temperature synthesis method using natural mineral potash feldspar as raw material [179]. The same authors prepared leucite from kaolin. Reagent grade $Al_2(SO_4)_3$ and K_2SO_4 and 2–10 μm Chinese kaolin were mixed and treated. Although, the pure leucite phase was obtained al lower temperature after heating at 900 °C for 3 h. Spherical leucite crystals having a diameter of approximately 50 μm were obtained.

The synthesis of leucite by hydrothermal reaction was reported [189] as well. The same reaction was used to synthetize leucite from analcime. All syntheses were carried out in autoclaves at a temperature of 200 °C. After the hydrothermal treatment, the content of the autoclave was washed with boiling distilled water, vacuum filtered and dried in an oven at 100 °C [190].

The precursor for the preparation of $KAlSi_2O_6$ was synthesized by sol-gel method when KNO_3, $Al(NO_3)_3 \cdot 12H_2O$ and TEOS were used as raw materials. After doping with 1.5 wt. % CaF_2, the leucite synthesized at 850 °C had a crystal size of 0.8 μm, and its calculated coefficients of thermal expansion (20 °C to 400 °C) reached 29.50×10^{-6}/°C, which is very close to the theoretical value of pure leucite [180].

4.3 GLASSES FOR OPTICAL APPLICATIONS

Glass is a promising host to investigate the influence of chemical environment on the optical properties of the rare earth ions as it affords considerable flexibility

in size and shape, good optical properties, and can be doped at very high concentrations of activator ions with excellent uniformity [18, 19]. The optical properties of rare earth ions in vitreous matrices have been widely investigated because of their basic interest and potential applications as lasers and phosphors [191]. The alkaline earth aluminosilicate glasses possess wide band gap energies around 5.0 eV. It makes them as suitable host materials to study $4f^n \rightarrow f^{n-1}5d$ transition interactions in dopant rare-earth ions [192]. Several researchers have noted that co-doping with Al^{3+} is effective for the dispersing of rare earth ions in silica gel and silicate glass matrices. Subsequently, the spacing among RE elements is larger in the alumina-doped silica host rather than in the non-alumina-containing host [193]. Among the rare earths, Tb^{3+} ions in different hosts could show an intense green emission and hence those have been used in the development of efficient green emitting phosphors and scintillator materials. Several reports have also confirmed the use of Tb^{3+} as an active ion in laser glasses [192]. The Eu^{3+} doped in the Al–Si–O matrix can be used for red phosphors [194].

CHAPTER 5 THERMAL PLASMA SYNTHESIS METHOD

5.1 INTRODUCTION TO RF THERMAL PLASMA SYNTHESIS METHOD

In recent years, radio frequency (RF) induction thermal plasma technology has emerged as a novel technique for the manufacturing of modern and enhanced materials, such as preparation of various kinds of nanoparticles in metallic and ceramic systems. This enabling technique adds value to conventional materials making them high-quality and high-performance materials [195, 196]. Plasma, considered the fourth state of matter, consists of a mixture of electrons, ions and neutral species, but is electrically neutral. “Hot” or “equilibrium” plasmas can be characterized by the approximate equality between heavy particle and electron temperature. Such plasmas are known as thermal plasmas [197]. Arc discharge, which is also often called thermal plasma, has proven to be of beneficial use in the

synthesis and surface modification of a broad range of metals and inorganic materials. Its basic advantages can be summarized as follows. Firstly, thermal plasmas have high temperatures (up to <15000 K). Because the plasmas are generated at relatively high pressures (close to atmospheric pressure), they have high densities and are considered to be at local thermal equilibrium (LTE). Other advantages are rapid quenching (from ~10^5 to ~10^6 K/s), high enthalpy of reaction kinetics and high chemical reactivity (high concentrations of chemically reactive radicals enhance the reactivity of thermal plasmas). Large volume with low velocity, oxidation and reduction atmospheres are able as well [198]. Microsized or nanosized spherical powders, depending on the morphology of the starting compounds [199] with narrow particle size distribution can be formed using thermal plasma processing [200]. Thermal plasma treatment also allows the transformation of irregularly shaped ceramic particles into spherical ones. These powders are more likely to be amorphous with small fractions of crystalline material. The scheme of the rf thermal plasma experimental set-up is shown in Figure 9.

Many methods have been used to produce nano-sized powders and one of the most efficient physical methods to produce nano-particles is the thermal plasma technique. During plasma processing, the raw materials are melted or partially melted, and even evaporated instantaneously in a high-temperature flame. The melting or vaporized particles will quench or condense into ultra-fine particles by subsequent rapid cooling [201].

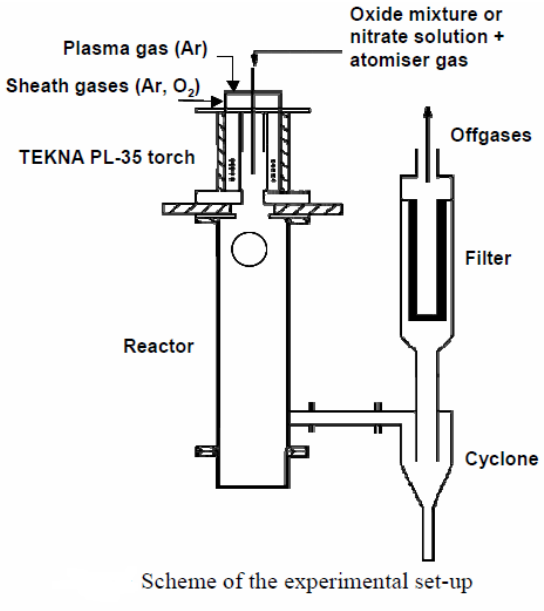

Figure 9. Scheme of the rf thermal plasma experimental set-up [197].

5.2 RF THERMAL PLASMA SYNTHESIS FOR ALUMINOSILICATES

Inductively coupled (RF) thermal plasma technique is important for utilizing municipal solid waste by recycling glass or inorganic fractions into an inert silicate slag or glass [202]. The idea not only recycle but synthetize glass or ceramic materials with potential appliance is very important as this method suggests good properties, such as high melting temperature and fast quenching, as well as sub-microne to nano-sized usually spherical powders [203]. There are reports on the synthesis and spheroidization of SiO_2 and Al_2O_3 ceramics [204-206], alumina/silica core-shell particles [207], glass powders [208], glass powders from waste in the system of Na–Ca–Al–Si–O [209] and zeolite [210]. But there was no data on leucite DC or feldshpathic GC synthesis employing RF-thermal plasma reactor.

RF-sputtering/spraying can be performed on either metals or ceramics, making it ideal for the coating of low toughness ceramic substrates such as dental porcelain [211, 212]. As an alternative for adhesion enhancement in dental ceramic bonding,

atmospheric pressure plasma treatment has been suggested. It enhances adhesion by producing carboxyl groups on the ceramic surface and improves the surface hydrophilicity [213].

5.3 RF THERMAL PLASMA SYNTHESIS FOR CALCIUM HYDROXYAPATITE

Variety of techniques are followed for the formation of biocompatible CHAp coatings on artificial implants. Plasma spraying is one of the recent and successful methods to fabricate functional biocompatible coatings on implants. In the recent years, the preparation of microspherical particles through plasma processing has attracted much attention for the production of free flowing feed stock powders for thermal spray applications. Hydroxyapatite was obtained from bovine bones through calcination process (850 °C) and was plasma processed to obtain flow quality powders. Also, calcium phosphate silicate glass ceramic was obtained when the CHAp-borosilicate glass (50 wt. %) mixture was melted in the plasma and crystallization of the melt occurred while cooling down at a much faster rate [214]. The SEM micrographs of obtained samples are shown in Figure 10.

The CHAp feedstock were prepared from mixture of 0.6 mol H_3PO_4 with 1 mol of $Ca(OH)_2$. The precipitation reaction was performed at 40 ± 5 °C and pH = 9. The so-formed CHAp suspension was spray dried kept in an oven at 60 °C for 12 h to remove any absorbed moisture. The spray-dried HA powders were sieved and powders with a particle size less than 20 μm were heat-treated at 1000 °C for 5 h to increase the thermal stability of the CHAp feedstock. Finally, CHAp was utilized in an inductively coupled plasma torch to obtain spherical and nano-sized particles [201].

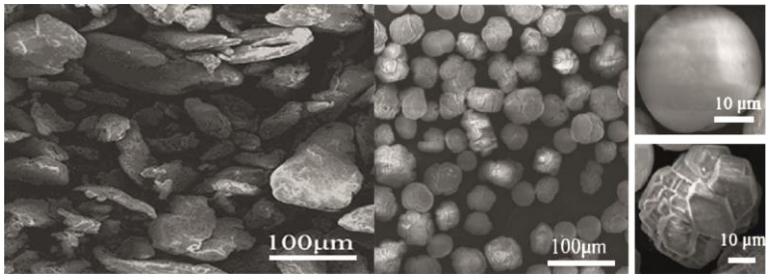

Figure 10. SEM images of CHAp powders from the left: the calcined CHAp are non-uniform morphology with coarser structure, next three images represent spherical particles with smaller size distribution after rf plasma treatment with average 30 µm particle size [214].

CHAPTER 6 INTRODUCTION TO SOL-GEL SYNTHESIS METHOD

The sol-gel process has great versatility: bioactive glasses can be made as microporous powders or monoliths, or as nanoparticles simply by changing the pH of the process. Metal alkoxides are popular precursors because they react readily with water. The reaction is called hydrolysis, because hydroxyl ion becomes attached to the metal atom [215]. The most studied example is sol-gel processing using tetraethoxysilane TEOS, $Si(OC_2H_5)_4$.

$$Si(OR)_4 + H_2O \longrightarrow HO{-}Si(OR)_3 + ROH \quad (14)$$

Depending on the water amount and catalyst hydrolysis may go to complete:

$$Si(OR)_4 + 4H_2O \longrightarrow Si(OH)_4 + 4ROH \quad (15)$$

Or molecules could be partially hydrolyzed:

$$Si(OR)_{4-n}(OH)_n \quad (16)$$

Two partially hydrolyzed molecules can link together in a condensation reaction:

$$Si(RO)_3{-}OH + HO{-}Si(OR)_3 \rightarrow (RO)_3Si{-}O{-}Si(OR)_3 + H_2O \quad (17)$$

or

$$Si(RO)_3{-}OR + HO{-}Si(OR)_3 \rightarrow (RO)_3Si{-}O{-}Si(OR)_3 + ROH \quad (18)$$

During condensation a small molecules, such as water or alcohol liberate. This type of reaction can continue to build larger and larger silicon-containing molecules by the polymerization. There are few types of condensation. The condensation process in which a hydroxyl bridge ("ol" bridge) is formed between two metal centres is called olation. Olation occurs by an S_N mechanism where the hydroxyl group is the nucleophile and H_2O is the leaving group:

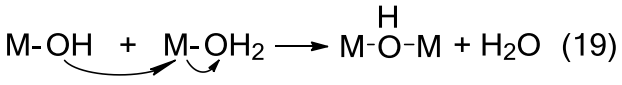

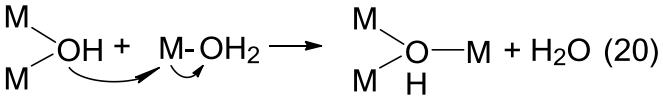

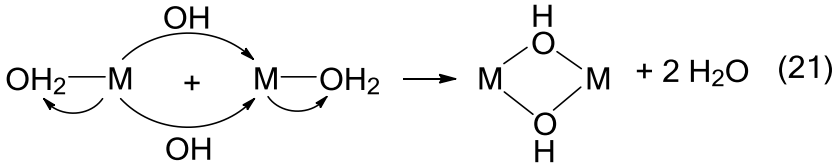

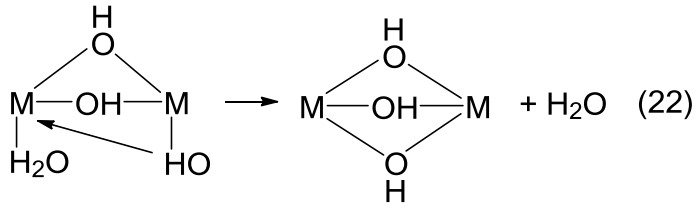

Condensation reaction in which an oxo bridge (–O–) is formed between two metal centres is named oxolation.

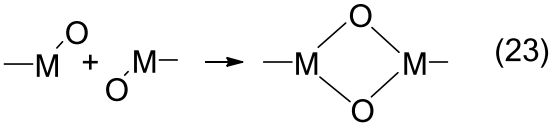

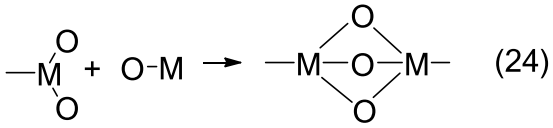

If the leaving group is water, the process is called oxolation; if the leaving group is alcohol – alcoxolation.

Hydrolysis and condensation reactions lead to the growth of clusters that eventually collide and link together into a gel. Then the polymerized network is forming. During drying (slow evaporation of solvent) procedure the xerogels or

aerogels are forming. Afterwards, xerogels are calcined to obtain a dense ceramic or crystalline oxides. The principle scheme of the sol-gel processing is presented in Figure 11.

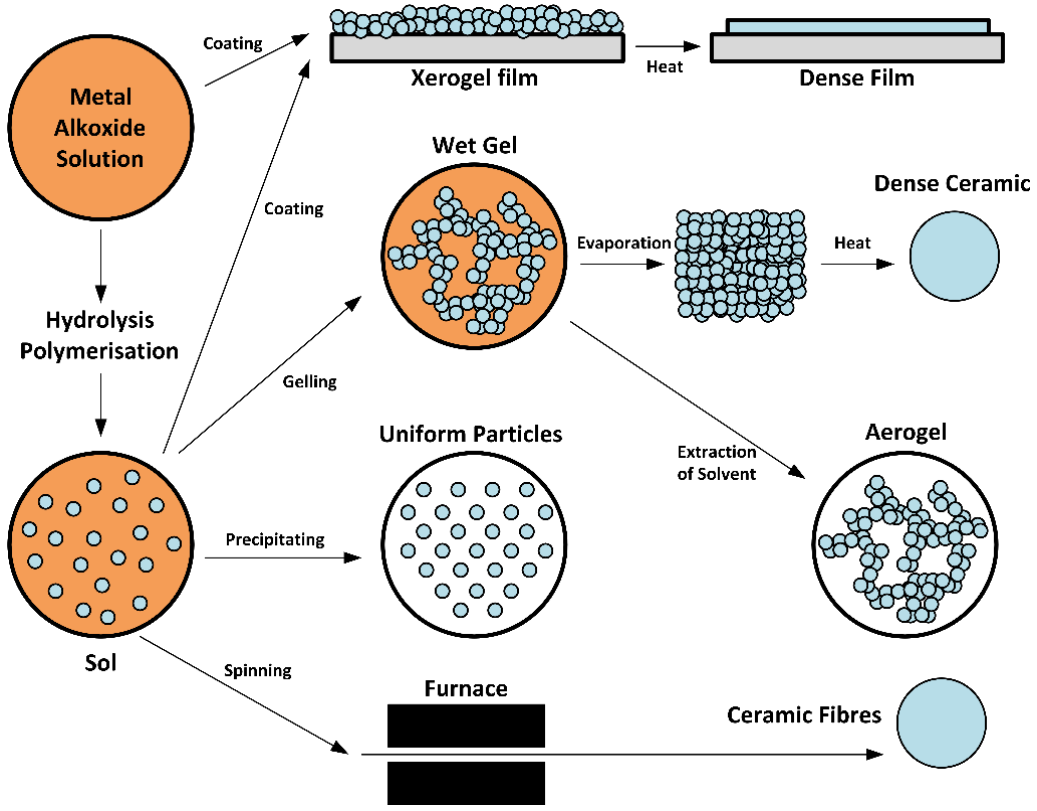

Figure 11. The principle scheme of the sol-gel processing.

The aqueous sol-gel technique was utilized to prepare CHAp and Le samples. As mentioned in previous chapters, the sol-gel approach allows to achieve effective mixing of precursors that increase the homogeneity and purity of the final materials.

CHAPTER 7 EXPERIMENTAL PART

This chapter is devoted to explaining the materials used, including suppliers and the product details, the synthesis schemes and/or equipment set-up, the material characterization techniques used in this work.

7.1 CHEMICALS AND REAGENTS

The starting materials were as follows:

For the synthesis of Le, Le:Re and aluminosilicates: Sm_2O_3 (99.9 % Alfa Aesar), Eu_2O_3 (99.9 % Alfa Aesar), Tb_4O_7 (99.9 % Alfa Aesar), $Ce(NH_4)_2(NO_3)_6$ (≥99 % Fluka), $Al(NO_3)_3 \cdot 9H_2O$ (≥98 % Aldrich), SiO_2 (fumed, >99 % Merck), KOH (≥85 % Czechoslovakia), $C_2H_6O_2$ (EG) (99,0 % Alfa Aesar), HNO_3 (67 % Reachem), SiO_2 (, < 45 micron (325 mesh)), SiO_2 (99.998 % Alfa Aesar, 1–20 micron), Al_2O_3 (99 % Aldrich, < 10 micron), KOH (90 % Aldrich) and for the synthesis of CHAp, $Ca(CH_3CO_2)_2 \cdot H_2O$ (99.9 % Fluka), $Mn(CH_3COO)_2 \cdot 4H_2O$ (98 % Russia), $Ce(NO_3)_3 \cdot 6H_2O$ (99.9 % Merck), $C_{14}H_{22}N_2O_8 \cdot H_2O$ (DCTA) (99 % Alfa Aesar), $C_4H_6O_6$ (TA) (99.5 % Aldrich), $C_{10}N_2H_{16}O_8$ (EDTA) (99,0 % Alfa Aesar), $C_2H_6O_2$ (EG) (99.0 % Alfa Aesar), $C_6H_{15}NO_3$ (TEA) (99.0 % Merck), $(NH_4)_2HPO_4$ (99 % Merck), H_3PO_4 (85 % Merck) were used.

7.2 SYNTHESIS METHODS

The synthesis and investigated samples in this work are listed in Table 7.

Table 7. Description of prepared samples

Sample	Formula (phase)	Composition (dopant concentrations expected in samples (mol %))	Method
Le	$KAlSi_2O_6$	-	Sol-Gel
Le:Eu	$KAlSi_2O_6:Eu^{3+}$	0.5; 1.0; 2.5; 5.0; 10.0	
Le:Ce	$KAlSi_2O_6:Ce^{3+}$	0.5; 1.0; 2.5; 5.0; 10.0	
Le:Sm	$KAlSi_2O_6:Sm^{3+}$	0.5; 1.0; 2.5; 5.0; 10.0	
Le:Tb	$KAlSi_2O_6:Tb^{3+}$	0.5; 1.0; 2.5; 5.0; 10.0	

KAS6	K-Al-Si-O	-	Rf-Thermal plasma
KAS40	K-Al-Si-O	-	
CHAp	$Ca_{10}(PO_4)_6(OH)_2$	-	Sol-Gel
Nano-CHAp	$Ca_{10}(PO_4)_6(OH)_2$		
CHAp:Ce	$Ca_{10-x}Ce_x(PO_4)_6(OH)_2$	0.005; 0.025; 0.05; 0.075; 0.1; 0.25; 0.5; 0.75; 1.0; 3.0; 5.0; 10.0	
CHAp:Mn	$Ca_{10-x}Mn_x(PO_4)_6(OH)_2$	1.0; 3.0; 5.0; 10.0	

7.2.1 Synthesis of calcium hydroxyapatite

For the preparation of $Ca_{10}(PO_4)_6(OH)_2$ having different morphological features four sol-gel synthesis routes (see Table 8) were selected.

Table 8. The overview of synthesis CHAp and precursors

Synthesis	Ca source	P source	Complexing agent	Dopant
I	$Ca(CH_3COO)_2 \cdot H_2O$	H_3PO_4	TA	-
II		H_3PO_4	EDTA, EG, TEA	-
III		$(NH_4)_2HPO_4$	TA	-
IV		H_3PO_4	DCTA	-
(I) Ce^{3+}		H_3PO_4	TA	$Ce(NO_3)_3 \cdot 6H_2O$
(I) Mn^{2+}		H_3PO_4	TA	$Mn(CH_3COO)_2 \cdot 4H_2O$

Synthesis I: In the sol-gel process, calcium acetate monohydrate, $Ca(CH_3COO)_2 \cdot H_2O$, and phosphoric acid, H_3PO_4, were selected as Ca and P sources, respectively, in Ca/P mole ratio 1.67. Firstly, calcium acetate monohydrate was dissolved in distilled water under continuous stirring at 65 °C. After stirring at 60–65 °C for 1 h, the appropriate amount of H_3PO_4 was added to the above solution. Finally, 1.1255 g of tartaric acid dissolved in 50 ml of distilled water was added. The obtained solution was stirred in a beaker covered with watch glass for 10 h at the same temperature. After evaporation of solvent the transparent white gels were obtained. The gels were dried in an oven for 10 h at 110 °C. The obtained powders

were grinded in agate mortar and heated at 800 °C for 5 h, and repeatedly 2 times at 1000 °C for 5 h. Synthesis II: In the sol-gel process the same starting materials as in the Synthesis I were selected. The mixture of calcium acetate and phosphoric acid was stirred at 60–65 °C for 1 h. Instead of tartaric acid, the 1,2- ethanediol, ethylenediaminetetraacetic acid (EDTA) and triethanolamine (TEA) were selected as complexing agents. To the above solution 4 ml of 1,2- ethanediol and 8.767 g of EDTA dissolved in distilled water were added. Then 5 ml of TEA was added dropwise to dissolve precipitates. Obtained mixture was vigorously stirred for 12 h at 60–65 °C in a beaker covered with a watch glass. After evaporation of solvent the transparent white gels were obtained. The gels were dried in an oven for 10 h at 110 °C. The obtained powders were grinded in agate mortar and heated at 800 °C for 5 h, and repeatedly 2 times at 1000 °C for 5 h. Synthesis III: In the sol-gel process, calcium acetate monohydrate, $Ca(CH_3COO)_2 \cdot H_2O$, and ammonium hydrogen phosphate, $(NH_4)_2HPO_4$, were selected as Ca and P sources, respectively, in Ca/P mole ratio 1.67. The following synthesis steps were the same as during Synthesis I. Synthesis IV: In the sol-gel process, calcium acetate monohydrate, $Ca(CH_3COO)_2 \cdot H_2O$, and phosphoric acid, H_3PO_4, were selected as Ca and P sources, respectively, in Ca/P mole ratio 1.67. In order to obtain water soluble calcium complexes and thereby avoid undesirable crystallization of calcium phosphates, 1,2-diaminecyclohexanetetraacetic acid monohydrate (DCTA) (11.2 g) was dissolved in distilled water, and afterwards added to the initial solution. Finally, after slow evaporation under continuous stirring at 65 °C, the Ca–P–O sols turned into transparent gels. The oven dried (100 °C) gels powders were ground in an agate mortar, heated up to 800 °C and calcined two times at 1000 °C for 5 h in air. Figure 12 shows the CHAp synthesis route systematically.

$Ca_{10-x}Ce_x(PO_4)_6(OH)_2$ and $Ca_{10-x}Mn_x(PO_4)_6(OH)_2$ samples were prepared by using Synthesis I route. The scheme of sol-gel preparation of CHAp samples is

presented in Figure 12. Ce concentration was in the range of 0.005–10 mol %, whereas manganese 1–10 mol %.

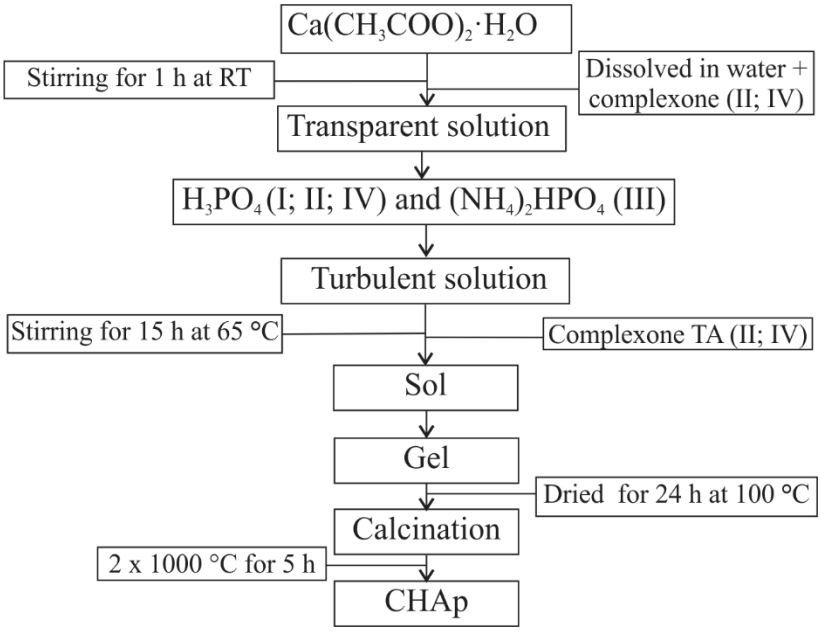

Figure 12. The overview of CHAp sol-gel synthesis route

For the fabrication of well-dispersed and homogeneous nano-hydroxyapatite particles the sol-gel derived CHAp powders were additionally milled. Milling was conducted at room temperature under air atmosphere in a vertical planetary using hardened ZrO_2 balls with a diameter of 1 μm and a stainless steel cell. The milling cell was loaded with 14 g of hydroxyapatite powder together with 160 g of ZrO_2 balls and was sealed by using a Vitron O-ring. The duration of the milling process for preparing of well-dispersed nano-hydroxyapatite crystallites was 1 h using 5000 rpm. The prepared nano-CHAp were examined for bone 3D scaffold design and tooth remineralization applicability.

As shown in Figure 13, the nano-CHAp powders were mixed with interpolymer complex (IPC). This technique highly resembles the versatile microsphere sintering route that provides porous ceramic scaffolds. This method involves mixing ceramic materials, water, monomers and dispersing agents, as well as initiators and catalyst

to promote polymerization. After all the mixture is placed into the pressureless sintering furnace to avoid density variations in final product.

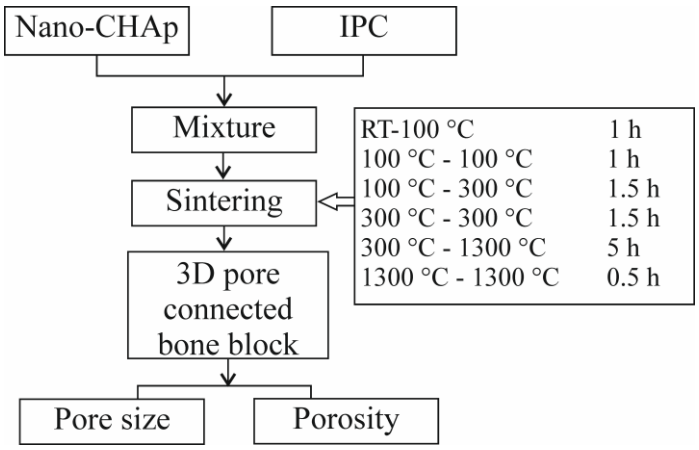

Figure 13. The flow chart of 3D Bone Blocks preparing details

CHAp has the tendency to agglomerate, which resulted in rapid sedimentation and consequently limited mobility in aqueous or solvent environment. Especially the nano-scaled particles agglomerate too quickly. Basically, we need to avoid sedimentation and flocculation, if it's suspension, and coalescence and creaming, if it's emulsion. The two main mechanisms for colloid stabilization involve steric and electrostatic modifications. The main aim of this experiment is to prepare a stabile colloid suspension/dispersion in aqueous and perhaps non-aqueous environments. The desirable pH ranges 8–9, as acidic solution etches CHAp. Narrow dispersion in water: for this procedure we need to make a dispersion of 10 % (wt.) in water, alkaline environment, about 8-9 pH, using ammonia. First step involves a ball milling. Conditions: ZrO particle size 50 μm. 7000 rpm, for 10 and 15 min. A sonificated CHAp sample for 2 min. The disadvantages: cannot be sure about the final concentration and consistence (weather the zirconia is totally centrifuged and removed from the solution as the ZrO_2 can improve micro hardness of tooth enamel. In order to evaluate the remineralization of enamel by using nano-CHAp, nano-

CHAp was applied on the surface of teeth samples for 3 times and 10 minutes for each treatment. Figure 14 shows the procedure of tooth remineralization.

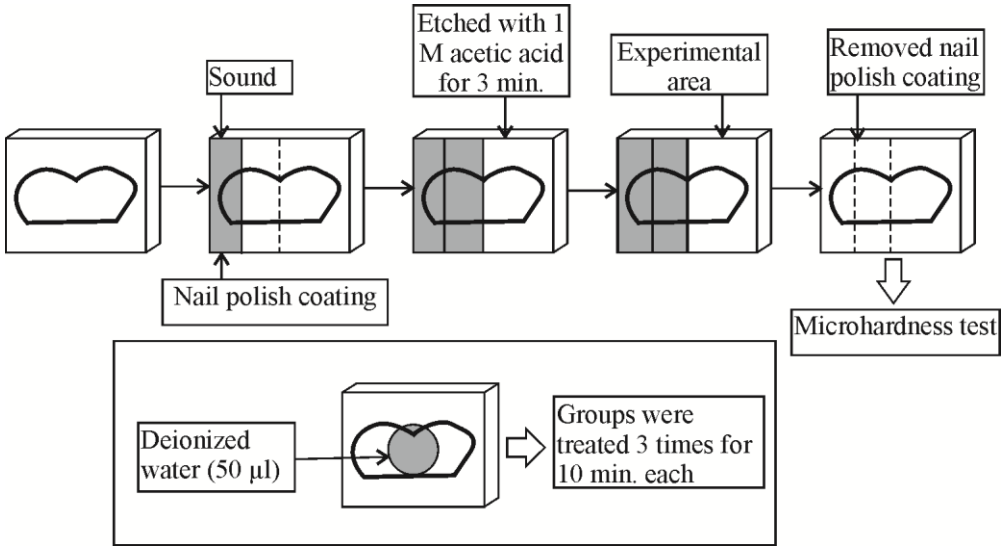

Figure 14. The experimental sequence of tooth remineralization test

Each extracted tooth was divided into 4 pieces and imbedded into methylmetacrilate blocks. Then polished to open the tooth enamel surface. The Knoope's microhardness measurements were performed at baseline, after demineralization with 1M CH_3COOH and after remineralization treatments. The first measures were performed before and after remineralization, using nano-CHAp. For the comparison, the remineralization of five groups were considered:

1. CHAp with nano-dispersion & centrifugation for 10 min;

2. CHAp with nano-dispersion & centrifugation for 15 min

3. As received CHAp

4. GC Moose® (main ingredient of CPP-ACP, casein phosphopeptide – amorphous calcium phosphate)

5. Artificial saliva

For the calculation of teeth remineralizationthe following equation was used:

$$\text{Remineralization (\%)} = \frac{KHN_{Treated} - KHN_{Etched}}{KHN_{Sound} - KHN_{Etched}} \times 100$$

7.2.2 Synthesis of leucite

For the synthesis (Figure 15), a stoichiometric amount of analytical grade reagents were used. Firstly, fumed silicon dioxide (SiO_2) was dissolved in 100 ml of distilled water under continuous stirring for 24 h at 65 °C. Potassium hydroxide (KOH) and aluminium nitrate nonahydrate ($Al(NO_3)_3 \cdot 9H_2O$) were separately dissolved in a small amount of distilled water. Both solutions were slowly added to the starting homogenized sol. In the next step, prepared sol was mixed for 1 h at the same temperature. To prevent crystallization of aluminium hydroxide during gelation processing, 1,2-ethanediol as a complexing agent (2 ml) was added. The sol was concentrated by slow evaporation of water at the same temperature in an open beaker. Obtained gels were dried in an oven for 24 h at 100 °C and then calcined in furnace at 700 °C for 5 h. Finally, after intermediate grinding ceramic materials were annealed in corundum crucible at higher temperatures. Annealing temperatures were ranking between 750 and 1000 °C, at heating rate of 5 °C/min. The scheme of sol-gel preparation of Le samples is presented in Figure 15.

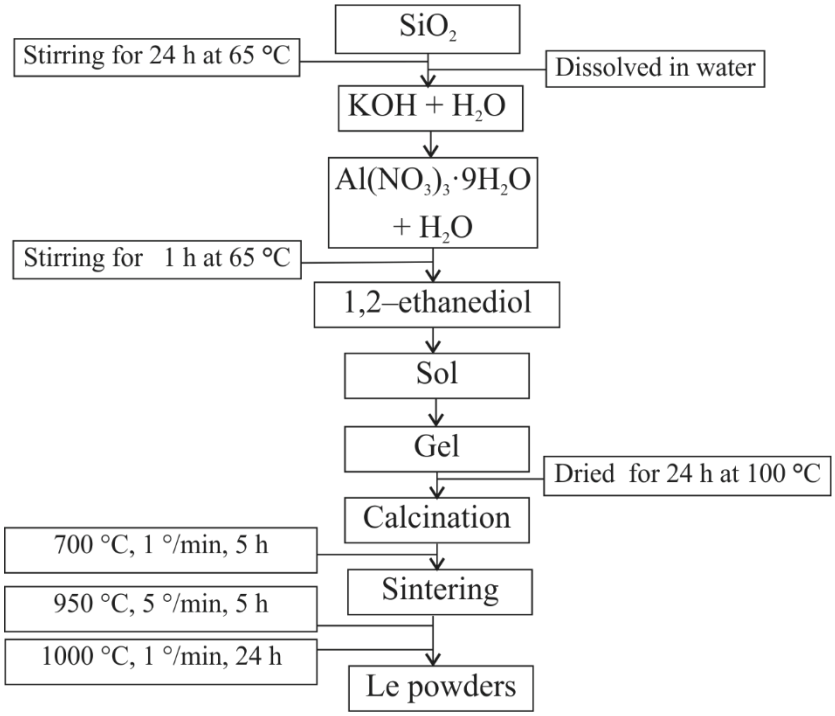

Figure 15. The overview of Le sol-gel synthesis route

For the synthesis of Le:Re we used the same silicon, potassium and aluminium sources were used. The Eu, Ce, Tb and Sm rear earth ions were selected as dopants in the Le matrix. The samples with different amounts of dopants (as shown in Table 7) were prepared by using the same sol-gel synthesis technique. The scheme of sol-gel preparation of Le:Re samples is presented in Figure 16. After dispersing fumed silicon dioxide in small amount (~50 ml) of distilled water the potassium hydroxide was added, previously dissolved in 25 ml distilled water with complexing agent EG. After few hours of stirring the opaque solution formed. The rear earth oxides were dissolved in nitric acid to form soluble compounds and mixed with EG. After 1 hour, the Al source dissolved in water with EG was slowly added to the sol. The 1,2-etahendiol was added in all steps to avoid precipitations and ensure the homogeneity of the final sol. The calculations were made assuming that dopant ions

would substitute potassium in the matrices, nevertheless they also can occupy vacancies or voids as in glass system.

The sol was then turned to gel by slow evaporation at ~70 °C and then dried for 24 h at 100 °C. The dried gels were calcined at 500 ºC for 5 h with a heating rate of 1 ºC/min to remove organic and nitrate components from the residual K_2O–Al_2O_3–SiO_2 glass powders. In order to convert the glass powder to glass-ceramic powder, calcined powders were heated at 900 ºC for 24 h with a heating rate of 5 ºC/min and at 1000 ºC for 24 h with a heating rate of 5 ºC/min. The glass-ceramic samples were named using following labels Le:Eu – **E-1**005, **E-1**01, **E-1**02, **E-1**05, **E-1**10, Le:Ce – **Ce-2**005, **Ce-2**01, **Ce-2**02, **Ce-2**05, **Ce-**210, Le:Tb – **Tb- 3**005, **Tb-3**01, **Tb-3**02, **Tb-3**05, **Tb-3**10, Le:Sm – **Sm-4**005, **Sm-4**01, **Sm-4**02, **Sm-4**05, **Sm-4**10. The first number indicates rear earth ion and the following the concentration, e.g. **Sm-4**10 indicates that samarium concentration is 10 mol % in the Le matrix.

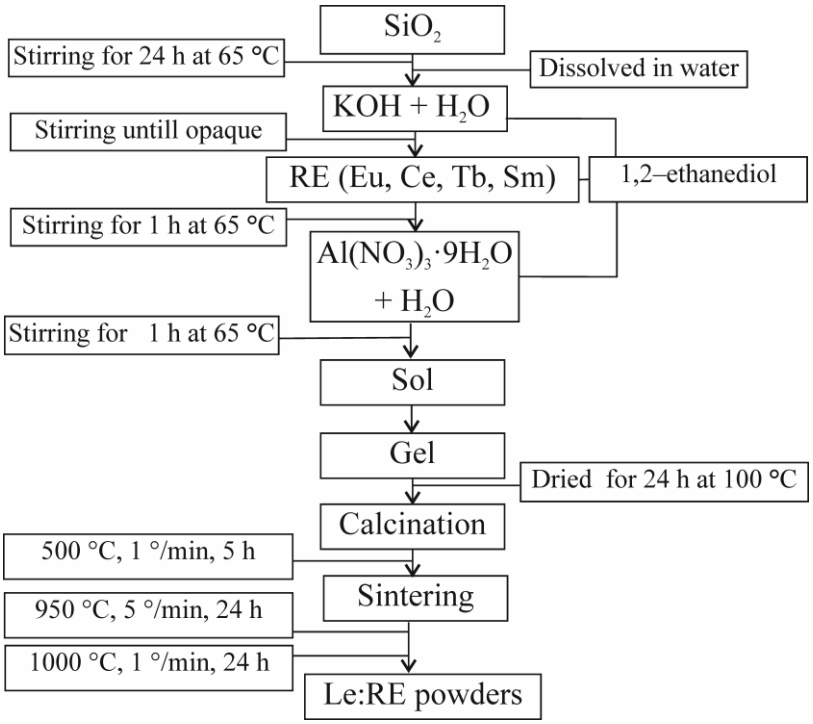

Figure 16. The overview of Le:RE sol-gel synthesis route

7.2.3 Synthesis of aluminosilicates

For the preparation of precursors, two differently sized crystalline silicon dioxide powders (~6 μm and ~40 μm) were used. Al_2O_3 (~10 μm) and KOH were source of aluminum and potassium, respectively. The molar ratio of silica/alumina was 4 and the potassium/alumina ratio was equal to 1. To form a ternary system of K–Al–Si–O, the initial compounds were grinded in an agate mortar until a homogeneous mixture was obtained and placed under an IR lamp for about 1 h to get rid of the adsorbed moisture from the air. The obtained precursor mixtures were placed in to a sample feeder. The synthesis experiments were carried out in an apparatus consisting of an RF inductively coupled plasma torch (TEKNA PL 35) connected to a reactor (3–5 MHz, max 35kW plate power), a cyclone, a filter unit and a vacuum pump (as shown in Figure 9). For the plasma torch, different mixtures of Ar and He as central and sheath gases were used. He was chosen as the carrier gas because of its high thermal conductivity and enthalpy, compared to other inert gases [216]. As several attempts showed, the plasma gases and their debit are very important for the successful synthesis of ceramic materials and should be optimized. The parameters of experiments are listed in the Table 9.

Table 9. Parameters of the rf thermal plasma reactor

Sample	Sheath gas (l/min)	Plasma gas (l/min)	Carrier gas (l/min)	Probe position (mm)
KAS6[x]	Ar – 29,5 He –18,55	Ar – 15,5 He – 7,95	He – 5.83	100 mm In the middle of the coil
KAS40[y]	Ar – 26 He –18,55	Ar – 13 He – 2,65	He – 5.83	100 mm In the middle of the coil

[x] where size of the SiO_2 particles is 6 nm

[y] where size of the SiO_2 particles is 40 nm

Both samples were injected into the hottest spot of the plasma flame. After reaction, the cooled particles were collected from the cylindrical steal reactor. The

resulting materials prepared from SiO_2 powders with particle sizes of 6 μm and 40 μm were designated KAS6 and KAS40, respectively.

7.3 MATERIALS CHARACTERIZATION

Powder X-ray diffraction analysis (XRD) has been carried out using Bruker D8 Advanced, Philips PW 1730, Rigaku MiniFlex II (with the Bragg-Brentano (θ/2θ) geometry) and PANalytical X'Pert diffractometers. The data was collected using CuK_α radiation. The functional groups were characterized by FTIR technique using Perkin-Elmer FTIR Spectrum BX II and Interspectrum 2000 FTIR spectrometers, pressing materials with KBr. The functional groups were characterized by Raman spectroscopy using DongWoo Optron spectrometer. The PerkinElmer STA 600 instrument used for simultaneous TG and DTA analysis. In order to study the morphology and microstructure of the ceramic samples scanning electron microscopes EVO 50 XVP, JEOL JSM 8404 and JSAM 6700F were used. The TEM images were recorded on a JEM 200 CX transmission electron microscope. The morphology of the resulting particles was determined with a field emission scanning electron microscope FE-SEM, Hitachi SU-70. The transmission electron microscopy study and energy-dispersive X-ray microanalysis were performed using a FEI (S)TEM Titan 80-300 microscope, operated at 300 kV and equipped with an EDAX system. For the TEM study an ethanol suspension of each sample was prepared and kept in an ultrasonic bath for 5 minutes and then a drop of this suspension was put onto a holey carbon film supported on a Cu grid.The average particle size of the powdered samples was determined from granulometric analysis data using a Malvern Nanosizer equipment. The specific surface area of hydroxyapatites was measured by nitrogen adsorption/desorption using Barrett-Emmett-Teller (BET) method (Micromeritics ASAP 2020). Mettler-Toledo MP220 pH-meter was used to determine pH of the solutions. The enamel microhardness test was carried out using HMV-2 Shimadzu micro hardness tester. The

photoluminescence excitation and emission spectra were measured with PerkinElmer (LS 55 Fluorescence) spectrometer.

CHAPTER 8 RESULTS AND DISCUSSIONS

8.1 SOL-GEL SYNTHESIS AND CHARACTERIZATION OF CALCIUM HYDROXYAPATITE

8.1.1 Sol-gel design of calcium hydroxyapatite

As was already mentioned in the Experimental part, for the preparation of $Ca_{10}(PO_4)_6(OH)_2$ having different morphological features four sol-gel synthesis routes (Synthesis I-IV) have been suggested. The results of characterization of obtained samples are presented herein.

8.1.1.1 X-Ray powder diffraction analysis

The XRD patterns of samples after calcination of different Ca–P–O gels obtained at 1000 °C are shown in Figure 17.

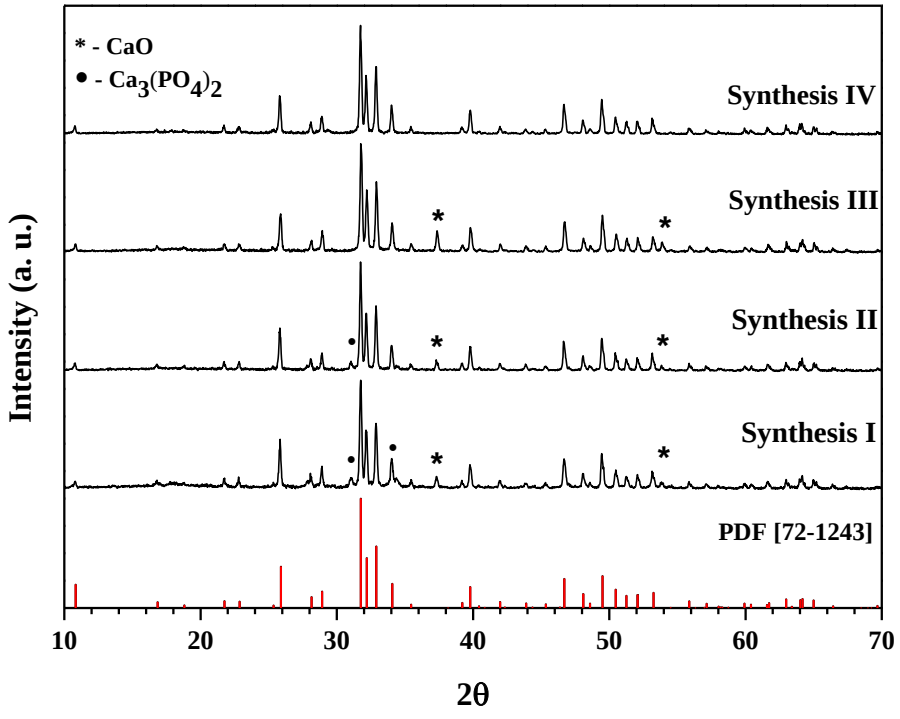

Figure 17. XRD patterns of the CHAp samples obtained after calcination of Ca-P- O precursor gel derived from different sol-gel syntheses. Impurity phases * - CaO, ● – $Ca3(PO_4)_2$

As seen, all four XRD diffraction patterns mostly contain diffraction lines attributable to calcium hydroxyapatite. The obtained results are in a good agreement with the reference data for $Ca_{10}(PO_4)_6(OH)_2$ (PDF [72–1243]). However, only Synthesis IV gave single-phase HAp product. XRD analysis results showed that the calcination products at 1000 °C of Ca–P–O gels obtained from Syntheses I-III besides desirable $Ca_{10}(PO_4)_6(OH)_2$ phase contain negligible amount of side $Ca_3(PO_4)_2$ or CaO phases, PDF [9-0169] and PDF [37-1497], respectively. The lattice parameters of the synthesized $Ca_{10}(PO_4)_6(OH)_2$ samples were obtained from the diffraction patterns by fitting the peaks of identified reflections. The hexagonal lattice parameters determined for the samples are very similar and were found to be a = 9.42(3) Å, and c = 6.86(2) Å that correspond to a stoichiometric hydroxyapatite.

8.1.1.2 SEM and TEM studies

Calcined Ca–P–O gel precursor powders were investigated by scanning electron microscopy, from which the grain size and typical morphologies of CHAp could be observed. The morphological features of the samples obtained from Synthesis I and II are given in the SEM pictures (Figure 18).

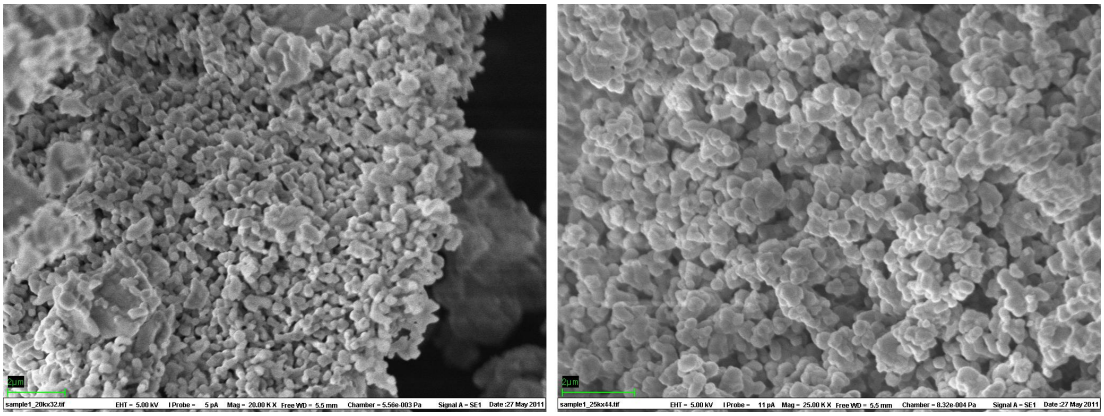

Figure 18. SEM micrographs of CHAp samples synthesized at 1000 ^{o}C from the Synthesis I (at left) and Synthesis II (at right)

The product of calcination derived from Synthesis I is made up of different size and shape particles. The particles are composed of agglomerates of elongated crystallites of 150–200 nm in size and necked to each other (see Figure 18, at left).

However, on the surface of CHAp nanocrystallites the larger plate-like particles of 0.5–1 μm in size are also seen. The EDX spectrum and appropriate area of CHAp sample taken for EDX analysis are shown in Figure 19.

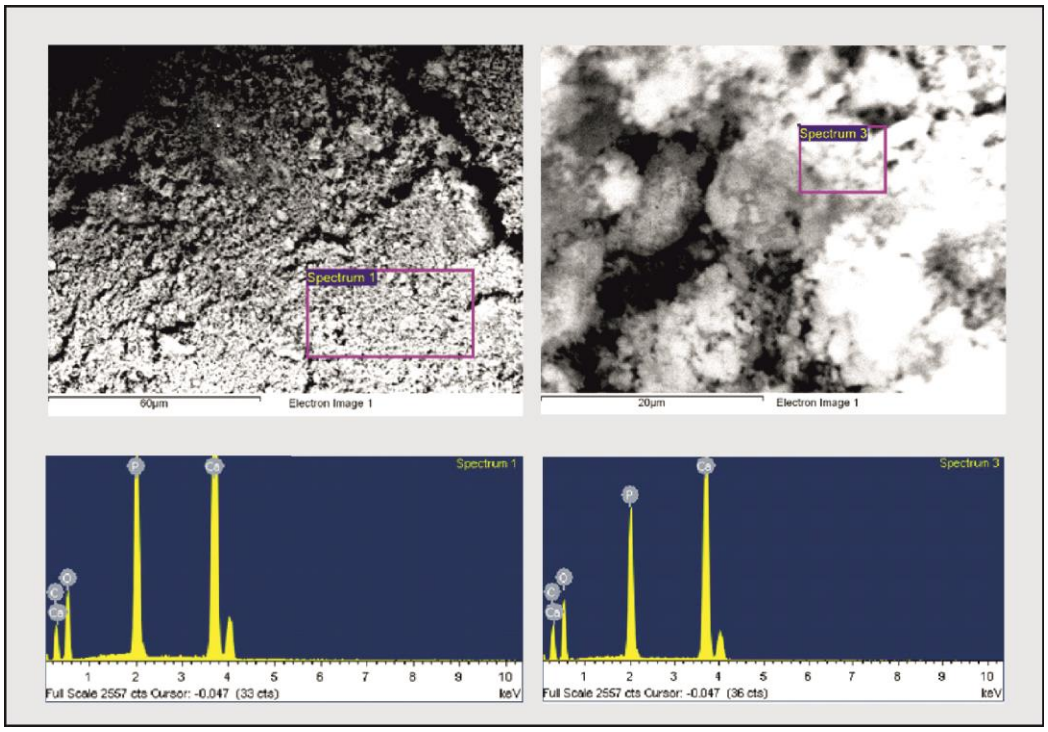

Figure 19. EDX spectrum and SEM micrograph of CHAp sample synthesized by the sol-gel chemistry route (Synthesis I) on the left and EDX spectrum and SEM micrograph of CHAp sample synthesized by the sol-gel chemistry route (Synthesis III) on the right

The EDX analysis showed that molar ratio of calcium and phosphor obtained from total area of CHAp sample derived from Synthesis I is Ca:P = 1.70:1.00, which is almost the same as nominal. However, the spot analysis of some crystallites gave molar ratio of Ca:P = 1.55:1.00, which corresponds to $Ca_3(PO_4)_2$ phase. The SEM micrograph of CHAp sample derived from Synthesis II (see Figure 18, at right) shows the formation of evenly distributed spherical nanoparticles with narrow size distribution. However, the particle aggregation phenomenon is also evident. The EDX analysis results of the CHAp sample derived from Synthesis II were Ca:P = 1.66:1.00.

The SEM micrographs of samples obtained from Synthesis III and IV are shown in Figure 20.

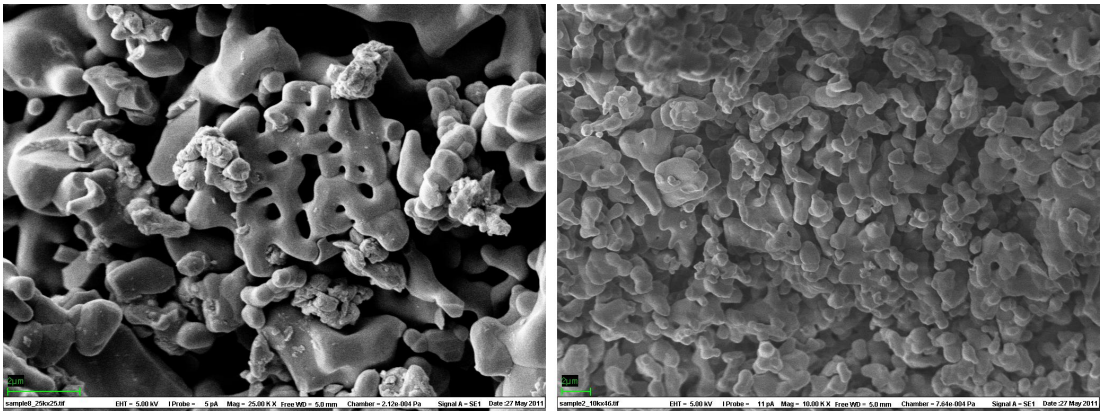

Figure 20. SEM micrographs of CHAp samples synthesized at 1000 °C from the Synthesis III (at left) and Synthesis IV (at right)

As seen, by changing phosphoric acid as phosphorus source to the ammonium hydrogen phosphate in the sol-gel processing quite different surface morphology of the final product has been obtained (see Figure 20, at left). The crystallites with highly symmetric ornaments instead of particles having smooth, uniform and small grained microstructure have formed. The EDX analysis showed, however, that molar ratio of calcium and phosphor obtained from total area of CHAp sample derived from Synthesis III is Ca:P = 1.69:1.00. The EDX spectrum and appropriate area of CHAp sample taken for EDX analysis are shown in Figure 19.

The CHAp powders synthesized using DCTA as complexing agent are composed of mixture of spherical nano- and submicron grains (~200–400 nm in size). The results showed that CHAp powders are composed of crystallites of broad size distribution. The EDX analysis results of the CHAp sample derived from Synthesis IV were approximately the same as in the case of Synthesis II, Ca:P = 1.66:1.00. In conclusion, the CHAp samples having slightly different surface morphology were obtained by changing starting materials or complexing agents in the sol-gel processing. However, in all of the cases, the highly agglomerated materials of differently shaped crystallites were formed. Interestingly, the global measurements

performed with granulometer revealed the variation of average crystal size of CHAp samples from ~7 μm to ~20 μm (Figure 21).

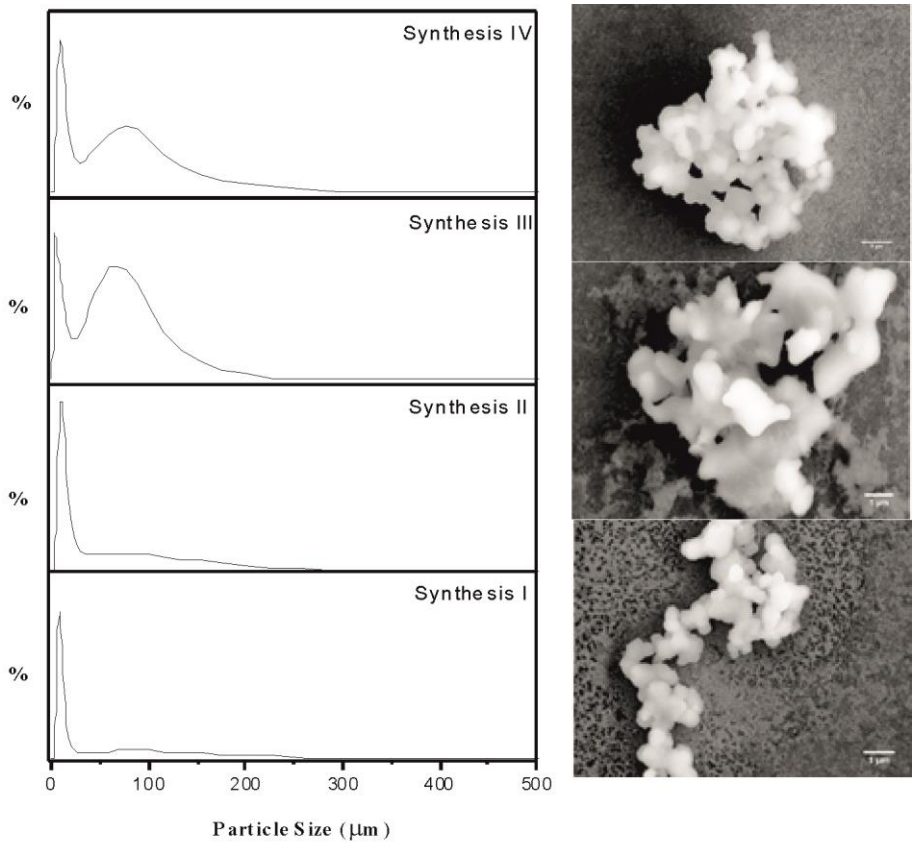

Figure 21. Granulometric analysis data (on the left) and TEM micrographs (on the right) of CHAp samples synthesized by different sol-gel methods

This figure also displays that CHAp crystallites synthesized using Synthesis I and II routes possess very narrow size distribution. On the other hand, the broad attendant bands let us to conclude that performed granulometric analysis gave average sizes of particle aggregates but not separate crystallites. The analogous conclusions from TEM measurements could be drawn, as was indicated by granulometric investigations. The transmission electron micrographs of a representative CHAp samples show the powders to consist of nano- and submicrocrystalline particles less than 1000 nm (Figure 21). The samples show a strong agglomeration of particles possibly due to the initial presence of organic residues, which can act as ‘binder’ for the crystallites.

8.1.1.3 FTIR spectroscopy studies

IR spectroscopy is highly sensitive to the impurities and substitutions in the structure of apatite. The IR spectra of CHAp samples obtained by sol-gel process using different synthesis parameters are shown in Figure 22.

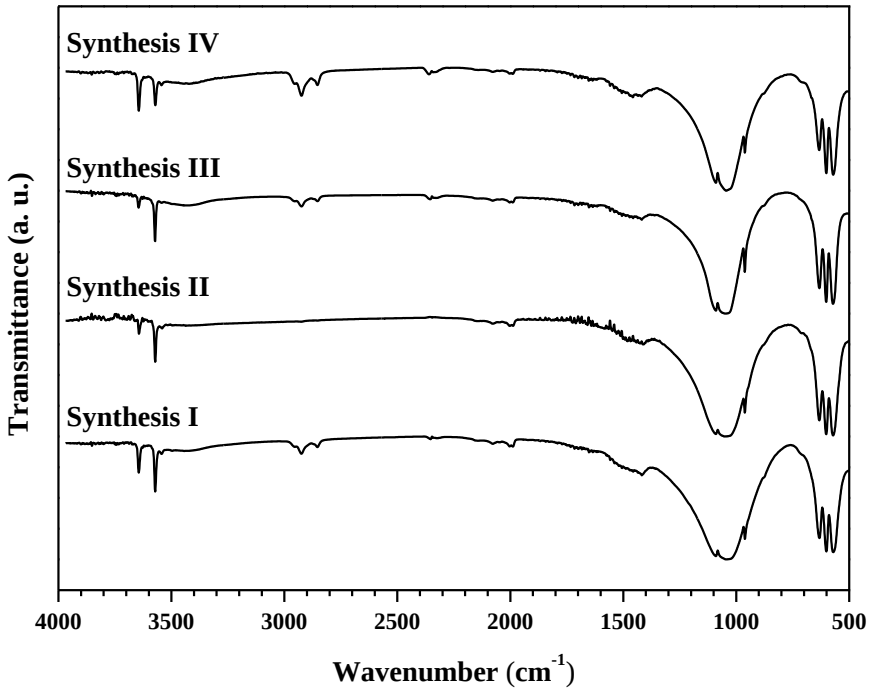

Figure 22. IR spectra of HAp samples synthesized using different routes of the sol-gel processing

In the IR spectra of calcined samples a complex band of the asymmetric stretching vibration of the phosphate group at 1000–1100 cm^{-1} dominates. In the region of symmetric stretching vibration of phosphate group at 940–970 cm^{-1} is seen. For the samples obtained from the gels with pH 11–12 a peak at 963 cm^{-1}, characteristic for CHAp, is observed. The peaks at 3570–3600 cm^{-1} could be assigned to the stretch vibration of OH^- group in the hydroxyapatite. The peaks assigned for carbonate substitution in apatite structure at 1400–1550 cm^{-1} are weakly expressed that is characteristic for apatites calcined at 1000 °C. Libration mode of OH^- appear at 3571 and 634 cm^{-1}. The presence of two characteristic bands (see Figure 23) around 572 and 602 cm^{-1} correspond to ν_4 (O–P–O) bending mode;

the 961 cm^{-1} band in the spectra was assigned to ν_1 (P–O) symmetric stretching and the doublet in the range 1100–1000 cm^{-1} was assigned to ν_3 (P–O) antisymmetric stretching mode. These bands indicate the characteristic molecular structures of the polyhedrons of PO_4^{3-} in the apatite lattice [217-219]. Therefore the IR spectra prove the results of XRD analysis about the formation of two or more phases due to calcination of the gels.

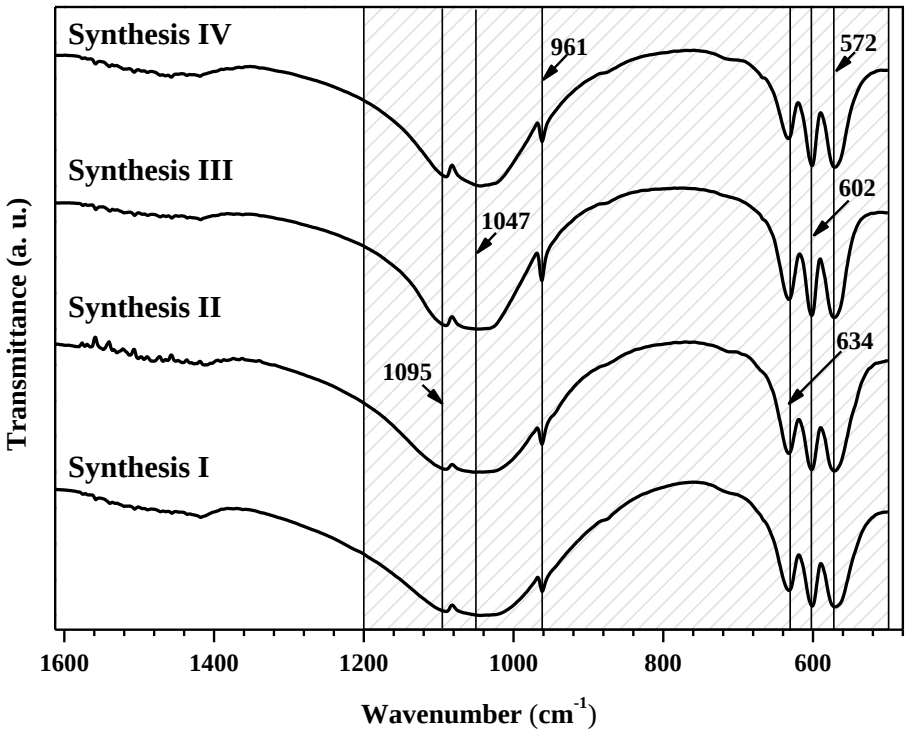

Figure 23. The FTIR spectra of CHAp samples in the region of 1200–500 cm^{-1}

8.1.2 Two-steps preparation technique for nanocalcium hydroxyapatite

The formation of nano-hydroxyapatite from sol-gel derived CHAp samples was performed using milling procedures. Milling was conducted at room temperature under atmosphere in a vertical planetary using hardened ZrO_2 balls with a diameter of 1μm and a stainless steel cell. Measurements of electrophoretic mobility were

implemented in order to investigate the dispersion profiles from milling process. Figure 24 shows the dependence of the zeta potential for hydroxyapatite.

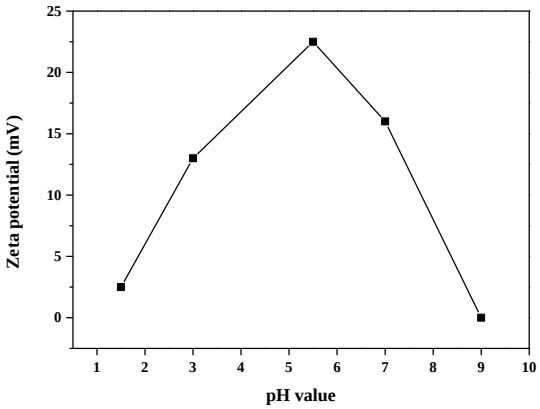

Figure 24. The dependence of the zeta potential with various pH values for hydroxyapatite

It can be found that the zeta potentials reaches the maximum value of 25 mV at pH = 6. It can be seen that the powder before milling had a broad particle size distribution up to 1283 nm. After milling, the particle size distribution reduced to 20 nm for nano-hydroxyapatite. Figure 25 shows visual surface observation of hydroxyapatite before and after milling. Before miling the precipitates of CHAp are seen on the bottom of the bottle. After shaking the turbid aqueous suspension of CHAp was obtained. However, the sedimentation of particles of CHAp obtained after milling was not observed. Moreover, almost transparent solution remained after shaking.

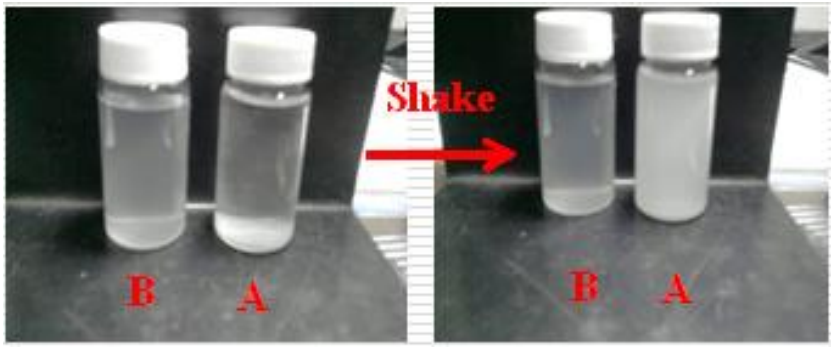

Figure 25. The observation of hydroxyapatite before milling (A) and after milling (B)

Figure 26 illustrates the Raman spectra of sol-gel derived calcium hydroxyapatite powders obtained before and after milling.

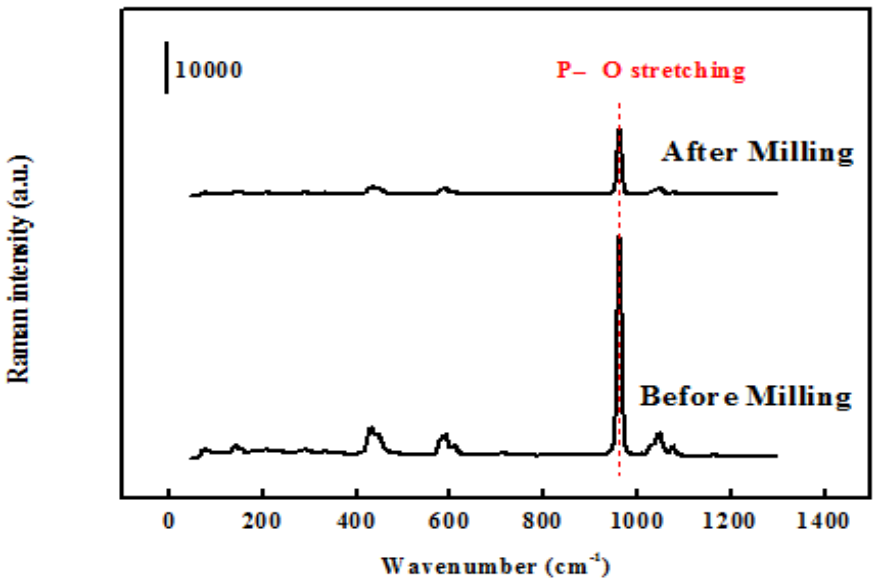

Figure 26. Raman spectra of calcium hydroxyapatite powders before milling and after milling

The main signal of P–O stretching in Raman spectrum of is found to be much weaker for the CHAp sample obtained after milling. Thus, Raman spectra clearly indicate that particles size decreases after milling procedure.

Figure 27 contains SEM micrographs of sol-gel derived calcium hydroxyapatite powders obtained before and after milling.

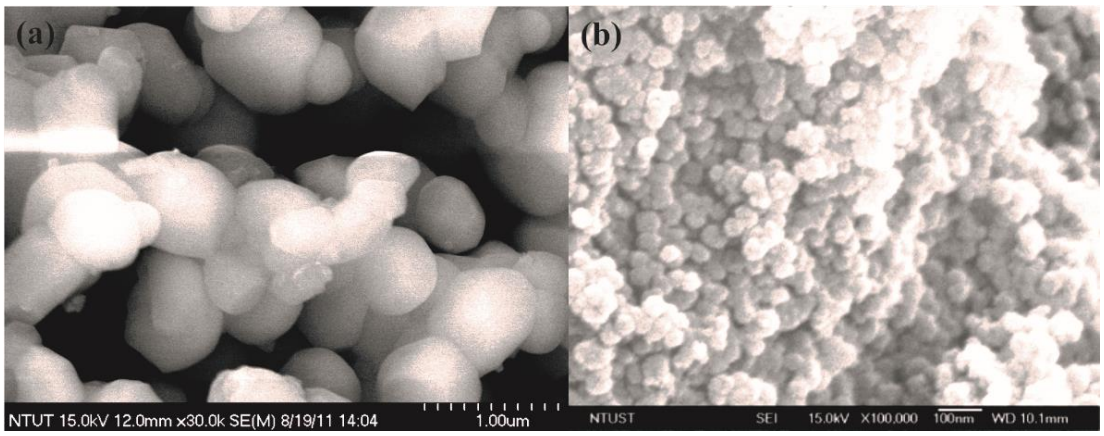

Figure 27. SEM micrographs of calcium hydroxyapatite samples: before milling (a) and after milling (b)

Compared with the initial powder, the morphology of the milled powders have changed significantly. The spherical particles of CHAp with uniform size distribution (about 20 nm) have formed during the second step of preparation of nano-hydroxyapatite. As was mentioned previously, the initial hydroxyapatite powders before milling showed high degree of agglomeration. The milled powders are also agglomerated, however, the milling resulted in a uniform distribution of hydroxyapatite crystallites.

Barrett-Emmett-Teller (BET) method was utilized to calculate the surface area. The pore volumes and pore size distributions were derived from the absorption branches of the isotherms using Barrett-Joyner-Halenda (BJH) analysis. The specific surface areas of samples are listed in Table 10.

Table 10. Summary of surface areas, pore volume, average pore size

Sample	S_{BET} (m^2/g)	Pore volume (cm^3/g)	Average pore size (nm)
Before Milling	0.96	0.000985	5.3
After Milling	1.91	0.004853	5.6

The surface area of hydroxyapatite samples increased after milling for 1 h from 0.96 to 1.91 m^2/g, which is consistent with the SEM results. Average pore size, however, remained almost unchanged.

8.1.3 Possible medical applications of obtained materials

The possible bone graft material as 3D scaffold was prepared in this study. The surface observation of the CHAp blocks showed in Figure 28, left. The porous HAp samples were also examined by SEM (Figure 28, right).

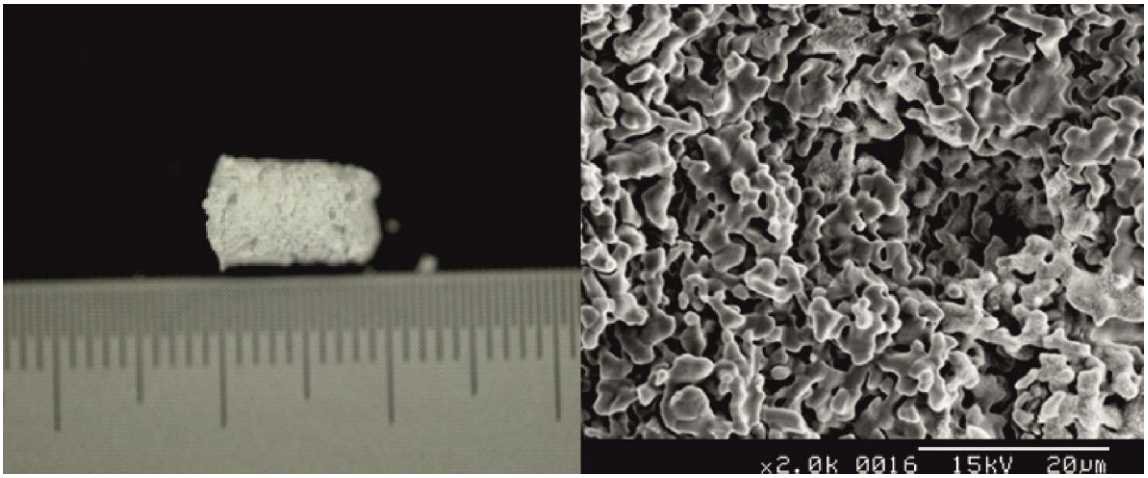

Figure 28. Surface observation of the CHAp blocks (left) and SEM micrograph of the HAp blocks showing the interconnected porosity (right)

The total porosity estimated by measure of the blocks density was 92.4 ± 2.2 % approximately, and the case of pore size, 384 ± 74 μm. The SEM micrograph of CHAp blocks revealed the formation of interconnected porosity. Such microstructure of synthetic CHAp is very applicable in the bone surgery for orthopaedic purposes.

The other possible medical application of CHAp as dental material for teeth remineralization was also evaluated. Dental erosion is a localized loss of the tooth surface by a chemical process of acidic dissolution of nonbacterial origin. Excessive consumption of acidic food and beverages promotes the softening and demineralization of enamel. The efficient remineralization after each food would be preferable. The remineralization test result of suspension consisted of 5 % Nano-CHAp is presented in Table 11.

Table 11. Summary of teeth remineralization

KHN	5 % Nano-CHAp
Sound	359.0 ± 30.0
Etched	214.6 ± 19.5
Treated	261.5 ± 18.8
Remineralization (%)	31.3 % ± 13.9 %

Five testing groups were examined as described in paragraph 7.2.1 and Figure 14. The composition of artificial saliva that was used as the controlling agent is listed in Table 12.

Table 12. Composition of artificial saliva

Component	Quantity
Methyle-p-hydroxybenzoate	2.00 g/l
Na Carboxymethylecellulose	10.0 g/l
$MgCl_2 \cdot 6H_2O$	0.29 mM
$CaCl_2 \cdot 2H_2O$	1.13 mM
K_2HPO_4	2.40 mM
KCl	8.38 mM
F^-	0.05 ppm
pH	7.2

The other controlling agent was commercial GC Mousse® with main ingredient casein phosphopeptide – amorphous calcium phosphate.

The visual representation of Knoop's microhardness test used is shown in Figure 29. The KHN results of all five groups are plotted in respect of the percentage difference from baseline and etched samples (as noted 100 %). As given in Figure 30.

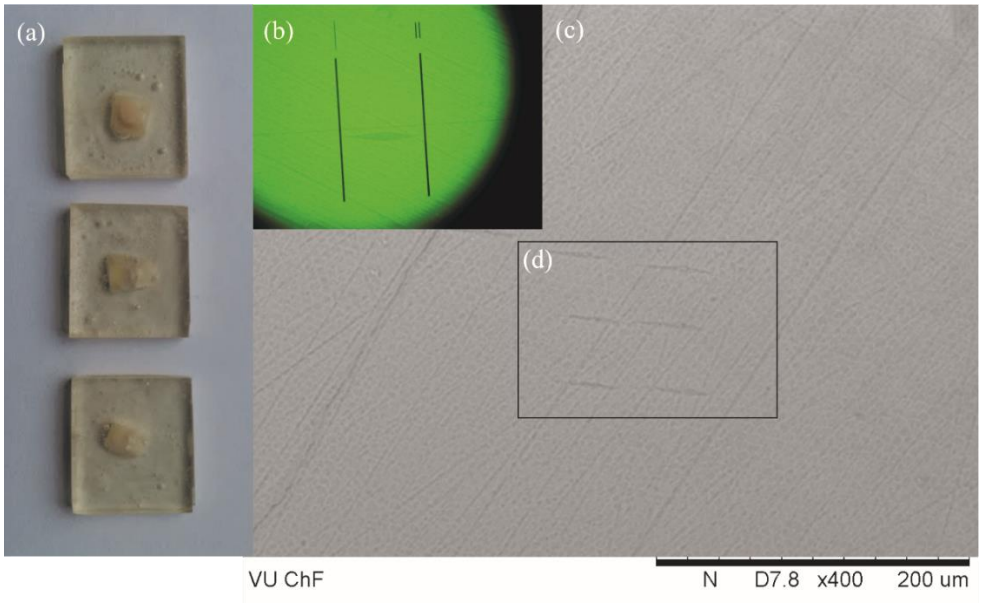

Figure 29. The visuals for KHN test where (a) shows the prepared specimens; (b) the view of the indentation form microhardness tester objective; (c) SEM image with detected 6 indentations (d) in the selected region

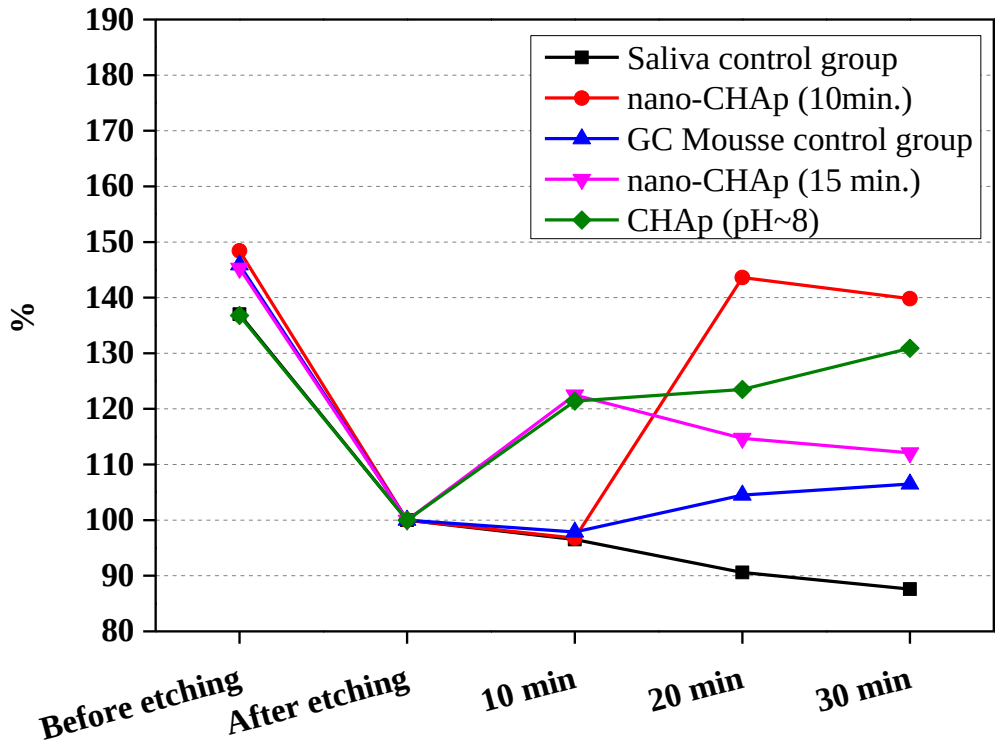

Figure 30. The relative microhardness values for human enamel exposed to two controlling groups and three 10 % CHAp containing groups

As given in Figure 30 only saliva controlling group gives negative response although it usually has remineralising effect in enamel self-repair process. In other words, according to this data, saliva increases demineralization of samples. The CHAp and GC Mousse gives the best response as the enamel microhardness increase after each emersion. Both nano-CHAp (10 min.) and nano-CHAp (15 min.) give good response after 20 min and after 10 min respectively. But sadly, later the microhardness decreases that suggest either the unsatisfying absorption at the enamel surface or the unimproved suspension. It is worth to mention that the experiment should be repeated for better data interpretation. Overall this data only suggest the potential use of the CHAp in teeth remineralization improvement.

Figure 31 shows enamel surfaces of all five examined groups.

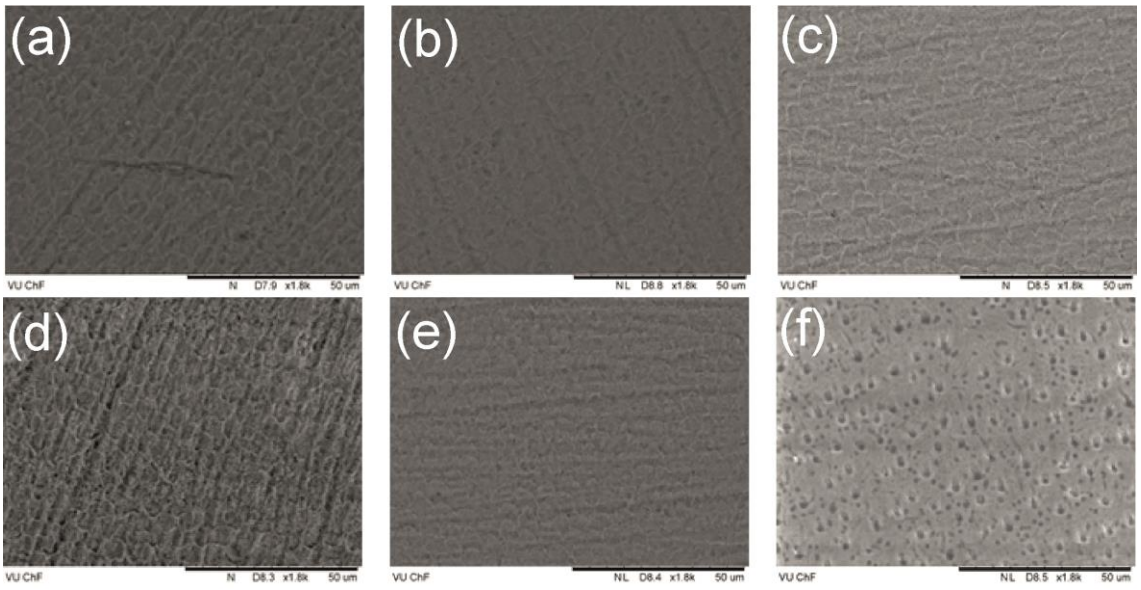

Figure 31. The SEM images of examined teeth surfaces of: saliva (a), nano-CHAp (10 min.) (b), GC Mousse (c), nano-CHAp (15 min.) (d), CHAp (e) and dentine (f)

Surface labeled (f) indicates severely damaged enamel with well pronounced holed indicating dentine structure. Other images indicates smooth surface, although not thick enough as the needle like rods of apatite crystals can be seen.

The remineralization process involves diffusion of calcium and phosphate ions into the body of the enamel lesion. The suspension should provide the localization of CHAp on the surface helping to maintain a state of supersaturation with respect to the enamel by suppressing demineralization and enhancing remineralization. These calcium and phosphate species increase the activities of the calcium and phosphate ions, thereby increasing the degree of supersaturation with respect to the hydroxyapatite crystals. The formation of hydroxyapatite in the lesion would lead to the generation of acid and phosphate, which would diffuse out of the lesion and down a concentration gradient. The dynamic equilibrium with free calcium and phosphate ions, would maintain the concentrations of the species involved in diffusion into the lesion. Efficient remineralizing solutions consume the acid generated during enamel lesion and aid in remineralization by generating more calcium and phosphate ions, thus maintaining their high concentration gradients into the lesion. The uneven curves in Figure 30 suggest that the suspensions might cause the demineralization of remineralized layers by simply washing away the Ca and P species and shifting the equilibrium towards a higher concentration gradient.

8.1.4 Mn and Ce substitution effects in calcium hydroxyapatite

The CP biomaterials doped with Mn ions should exhibit better resorbability and biocompatibility whilst doped with Ce ions – antibacterial properties, as suggested by literature data and is described in 3.2.2. Therefore, the manganese and cerium substitution effects in CHAp have been investigated in this study. The XRD patterns of $Ca_{10-x}Ce_x(PO_4)_6(OH)_2$ are presented in Figure 32. All the XRD patterns obtained have characteristic peaks that correspond to stoichiometric CHAp, PDF [72-1242]. Some impurities of CaO, CeO_2 and $Ca_3(PO_4)_2$ have been identified in differently substituted samples. By increasing the dopant concentration from 1 to 10 %, the characteristic CHAp peaks are weaker and the secondary phases become predominant. Utilizing these results, lower dopant concentrations were selected to avoid secondary phases.

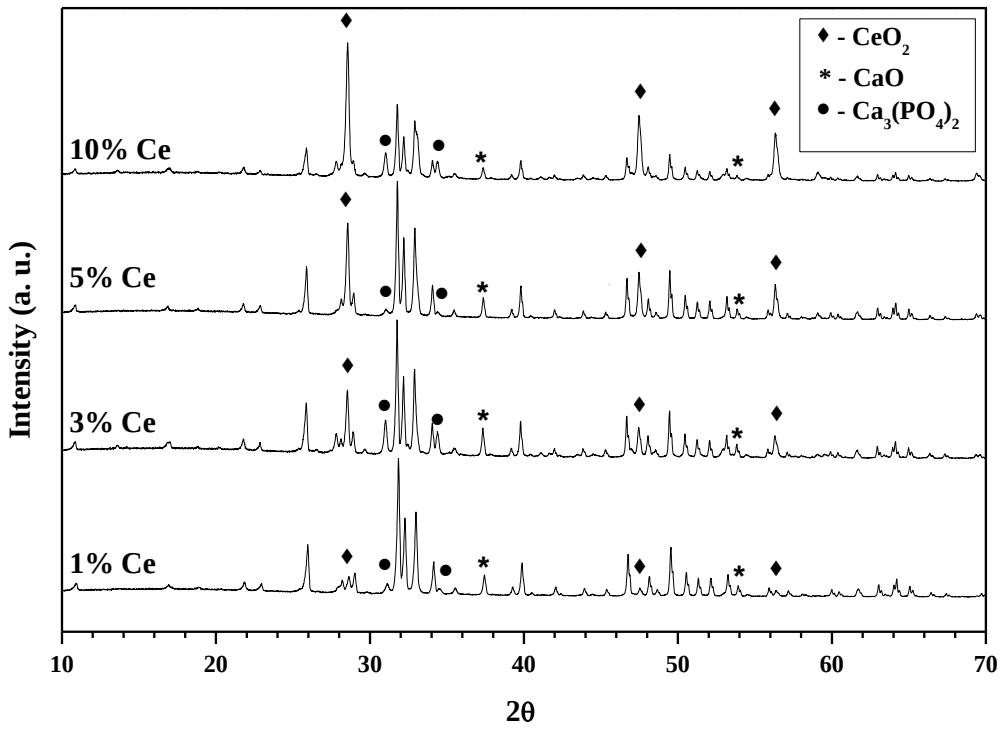

Figure 32. XRD patterns of $Ca_{10-x}Ce_x(PO_4)_6(OH)_2$, where Ce contents is 1, 3, 5 and 10 mol %

The XRD patterns of $Ca_{10-x}Ce_x(PO_4)_6(OH)_2$ specimens having smaller cerium concentrations (x = 0.1, 0.25, 0.5 and 0.75 %) are shown in Figure 33. Evidently, the predominant phase is CHAp with some traces of CeO_2 and CaO crystalline phase. It is worth to mention that $Ca_3(PO_4)_2$ has not formed in all synthesized samples.

It was decided to decrease dopant concentration again, to get rid of trace of CeO_2 phase. The XRD patterns of $Ca_{10-x}Ce_x(PO_4)_6(OH)_2$ samples where x = 0.005, 0.025, 0.05 and 0.075 % are shown in Figure 34. The only one secondary phase of CaO can be determined in these XRD patterns. The same impurity has formed in stoichiometric CHAp samples, utilizing Synthesis I (see Figure 17).

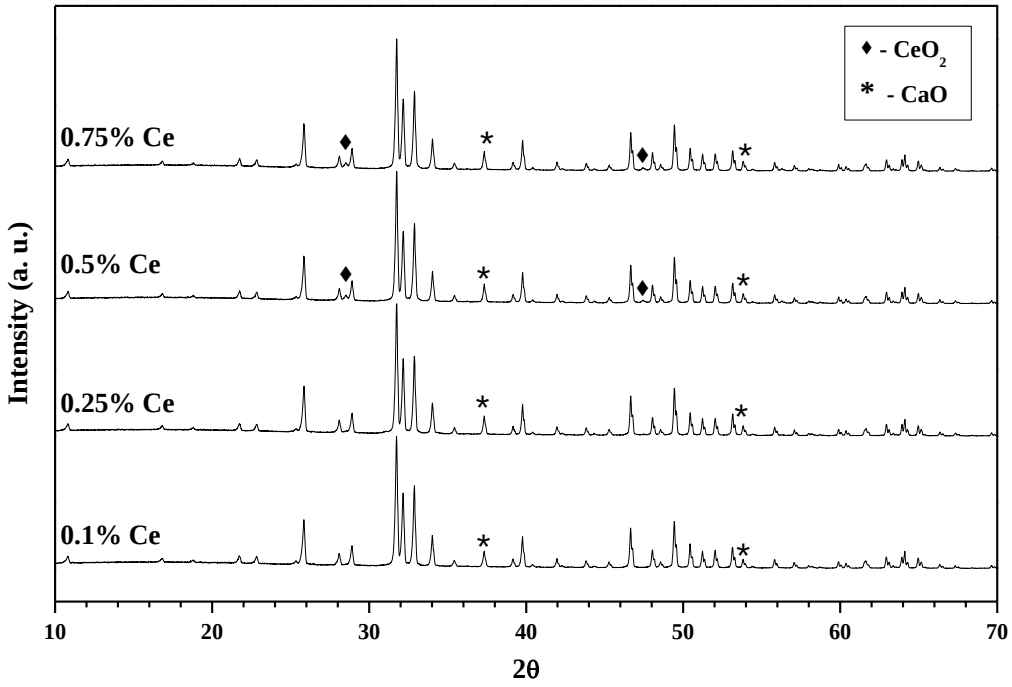

Figure 33. XRD patterns of $Ca_{10-x}Ce_x(PO_4)_6(OH)_2$, where Ce contents is 0.1, 0.25, 0.5 and 0.75 mol %

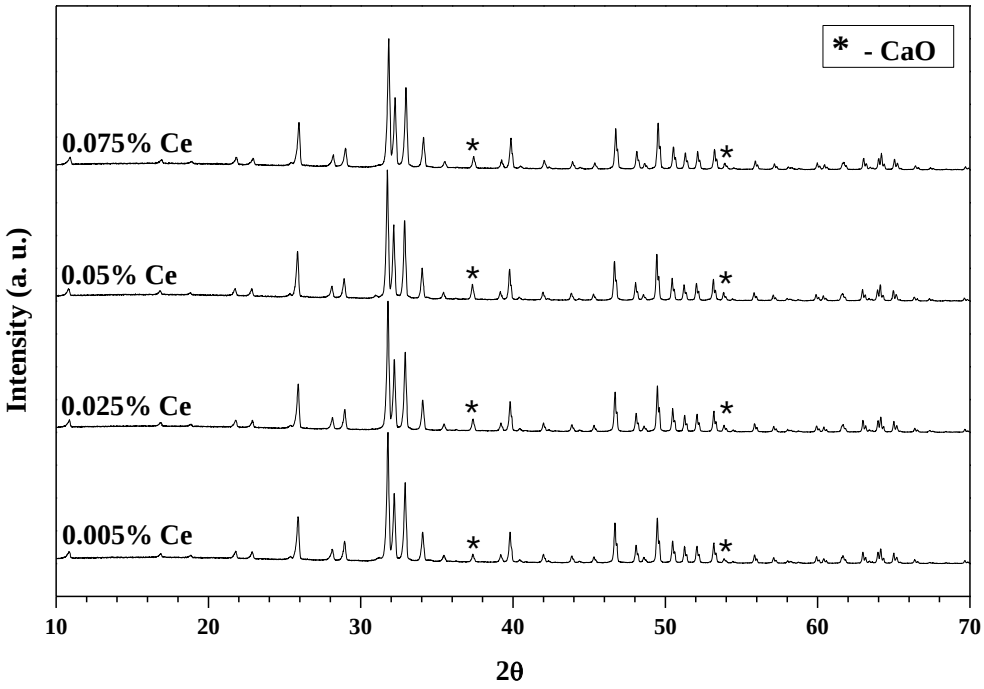

Figure 34. X-ray diffraction patterns of $Ca_{10-x}Ce_x(PO_4)_6(OH)_2$, where Ce contents is 0.005, 0.025, 0.05 and 0.075 mol %

So, the Ce concentration has no influence on the formation of CaO side phase, which depends on the synthesis route used.

XRD patterns of manganese-substituted $Ca_{10-x}Mn_x(PO_4)_6(OH)_2$ samples where x = 1, 3, 5 and 10 mol % are shown in Figure 35.

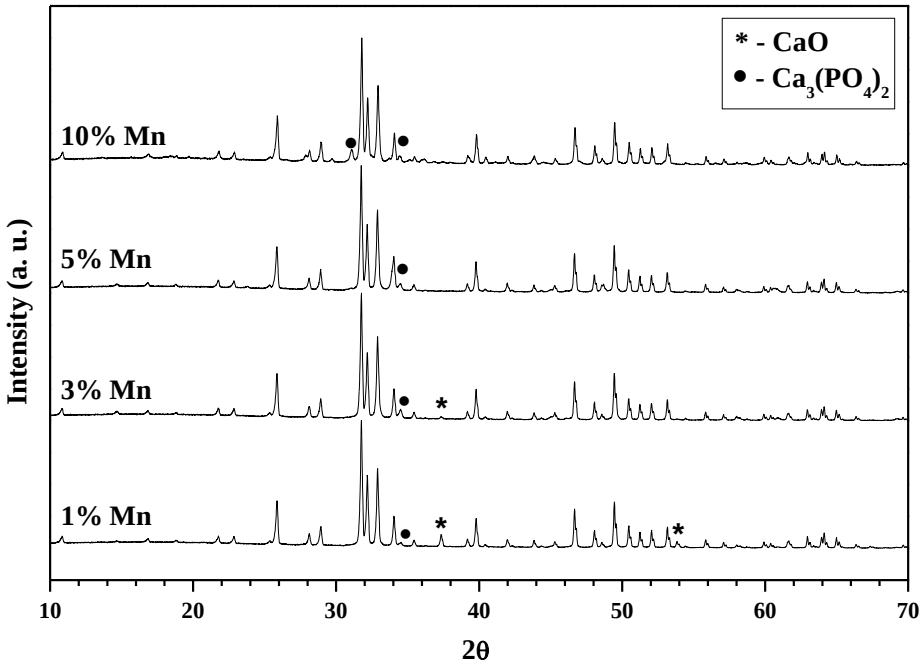

Figure 35. XRD patterns of $Ca_{10-x}Mn_x(PO_4)_6(OH)_2$, where Mn contents is 1, 3, 5 and 10 mol %

The CHAp is the main phase observed in all samples regardless the dopant concentration. Nevertheless, all prepared samples have impurities of $Ca_3(PO_4)_2$ and some of them contain CaO. Apparently, higher amount of manganese in comparison with cerium could be introduced instead of Ca to CHAp without destroying the crystalline structure of apatite.

The SEM images of $Ca_{10}(PO_4)_6(OH)_2$ with Ce concentrations 1–10 mol % are sown in Figure 36. The overall morphology of $Ca_{10-x}Ce_x(PO_4)_6(OH)_2$ samples does not depend on Ce concentration. The formation of particles having different size and shape can be seen. The bright parts in micrographs correspond to the cerium oxide.

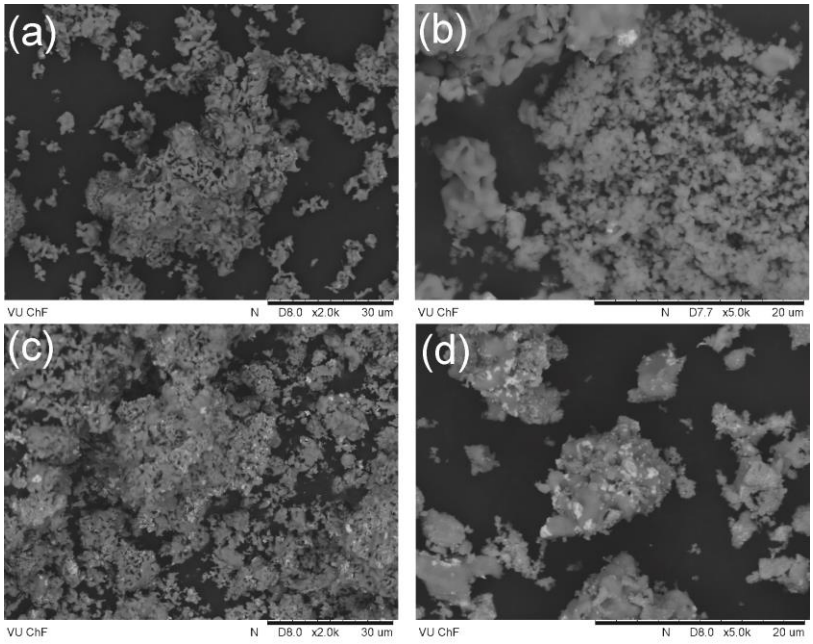

Figure 36. SEM micrographs of $Ca_{10}(PO_4)_6(OH)_2$, with different Ce content, SEM images: 1 % Ce – (a); 3 % Ce – (b); 5 % Ce – (c) and 10 % Ce – (d).

The bright parts, however, were not observed in the SEM images of samples with 0.025–0.75 mol % of Ce (Figure 37). These results are in a good agreement with XRD results. As seen, the submicron sized particles are obtained.

The SEM images of $Ca_{10}(PO_4)_6(OH)_2$ specimens with Mn concentrations of 1– 10 mol % are presented in Figure 38. Again, the Mn concentration like Ce does not influence morphology of the $Ca_{10-x}Mn_x(PO_4)_6(OH)_2$ samples.

Figure 39 and Figure 40 shows FTIR spectra of CHAp samples having different Ce and Mn substitution amount, respectively. All samples are generally assigned to CHAp, due to the presence of four PO_4^{3-} vibration modes at: 963 (PO_4^{3-} mode v_1), 470 (PO_4^{3-} mode v_2), 1029 and ~1095 (PO_4^{3-} mode v_3), and 601–561 cm^{-1} (PO_4^{3-} mode v_4), as well as the presence of OH^- stretching and libration modes at 3571 and 634 cm^{-1}, respectively.

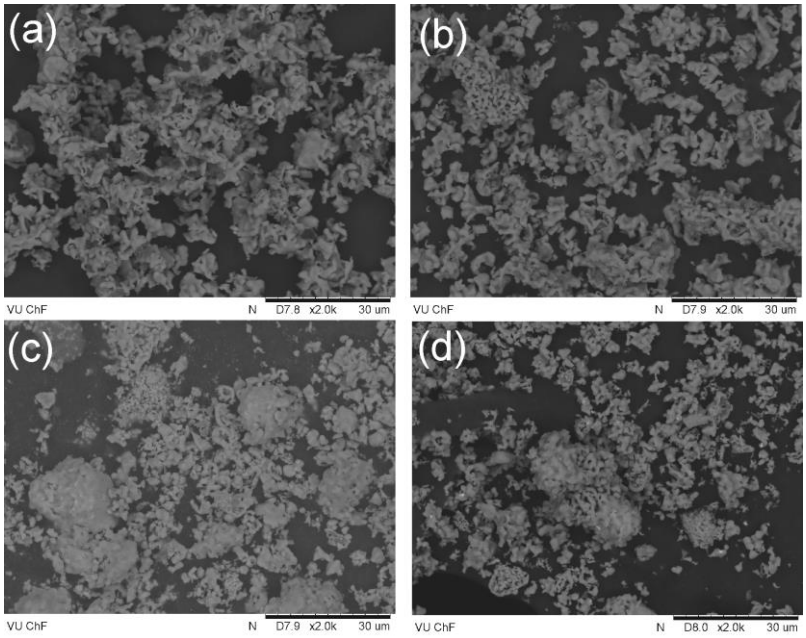

Figure 37. SEM micrographs of $Ca_{10}(PO_4)_6(OH)_2$, with different Ce content, SEM images: 0,025 % Ce – (a); 0,075 % Ce – (b); 0,25% Ce – (c) and 0,75 % Ce – (d).

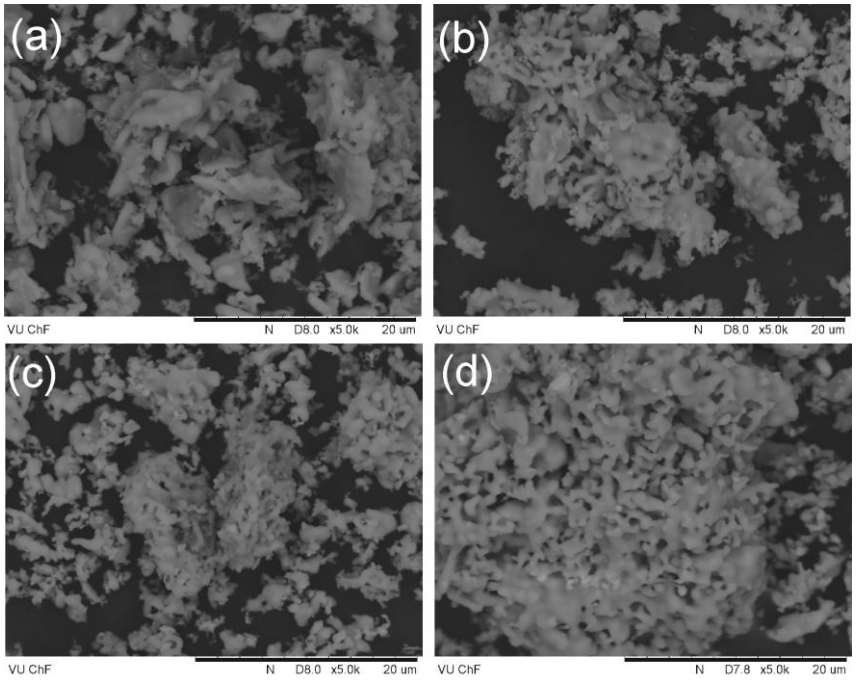

Figure 38. SEM micrographs of SEM images of $Ca_{10}(PO_4)_6(OH)_2$, with different Mn content,: 1 % Mn – (a); 3 % Mn – (b); 5 % Mn – (c) and 10 % Mn – (d).

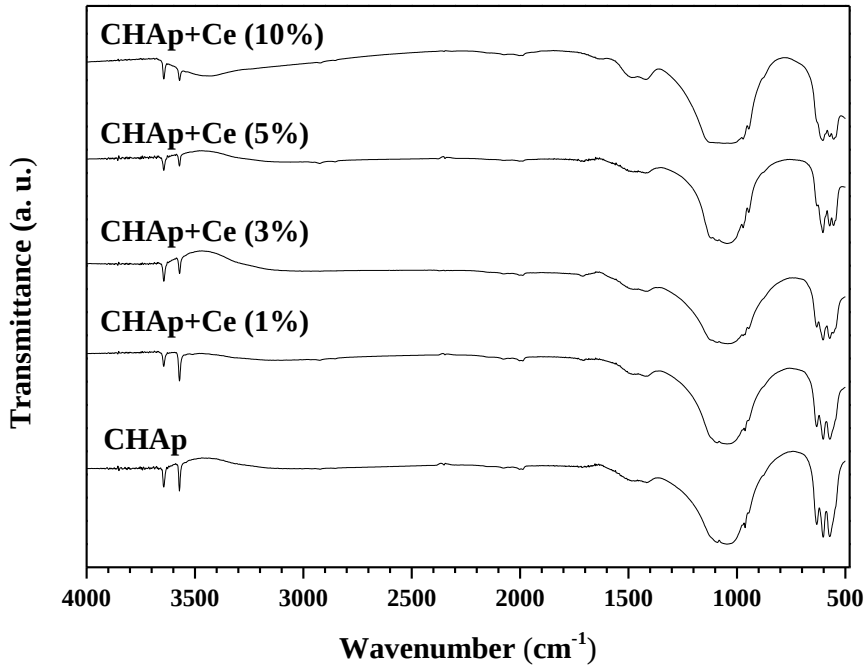

Figure 39. FTIR spectra of five different CHAp:Ce samples: Ce concentration from 0 to 10 mol %

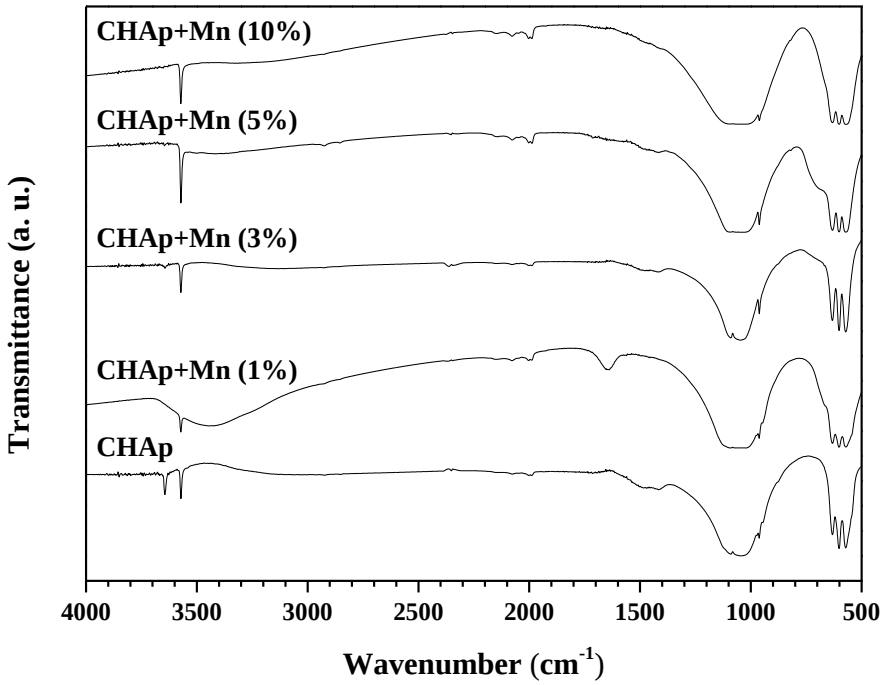

Figure 40. FTIR spectra of five different CHAp:Mn samples: Mn concentration from 0 to 10 mol %

By increasing amount of Ce^{3+} substitution up to 5 and 10 mol % (see Figure 39) the O–P–O bending mode v_4 is less intensive, whereas in the samples with Mn (see Figure 40) all spectra's are similar and do not depend on the dopant concentration. The small absorption bands in the region of ~1410–1450 cm^{-1} that appear in CHAp:Ce samples are designated to CO_3^{2-} vibrations (B-Type CHAp). The peak at ~1641 cm^{-1} in the CHAp +Mn (1%) is attributed to the H_2O adsorption during the synthesis process.

8.2 SYNTHESIS OF LEUCITE USING SOL-GEL DERIVED MOLECULAR PRECURSOR

8.2.1 Sol-gel preparation of monophasic leucite

8.2.1.1 X-Ray powder diffraction analysis

The phase composition of synthesized products after heating of K–Al–Si–O gel precursors at different temperatures was determined by XRD analysis. These results showed, that after heating of K–Al–Si–O gel precursors at 700 °C for 2 h amorphous material was obtained. However, the situation was different with increasing the annealing temperature up to 950 °C (see Figure 41). The XRD pattern of sample synthesized at 950 °C shows the formation of crystalline leucite phase. However, a small impurity peak located at $2\theta \approx 28.64°$ confirms the formation of kalsilite phase as well. On the other hand, this peak is much weaker in comparison with the main leucite reflections and mainly indicates the unfinished crystallization of leucite, when presumptively kalsilite reacts with residue of SiO_2. The monophasic leucite has formed after increasing annealing temperature up to

1000 °C using 24 h duration of heat treatment. As it can be seen from Figure 41, the single phase leucite (reference data PDF [038-1423]) with strong and distinct peaks at 2θ ≈ 25.84 and 27.30 has formed and no even traces of impurity phase of kalsilite has been observed.

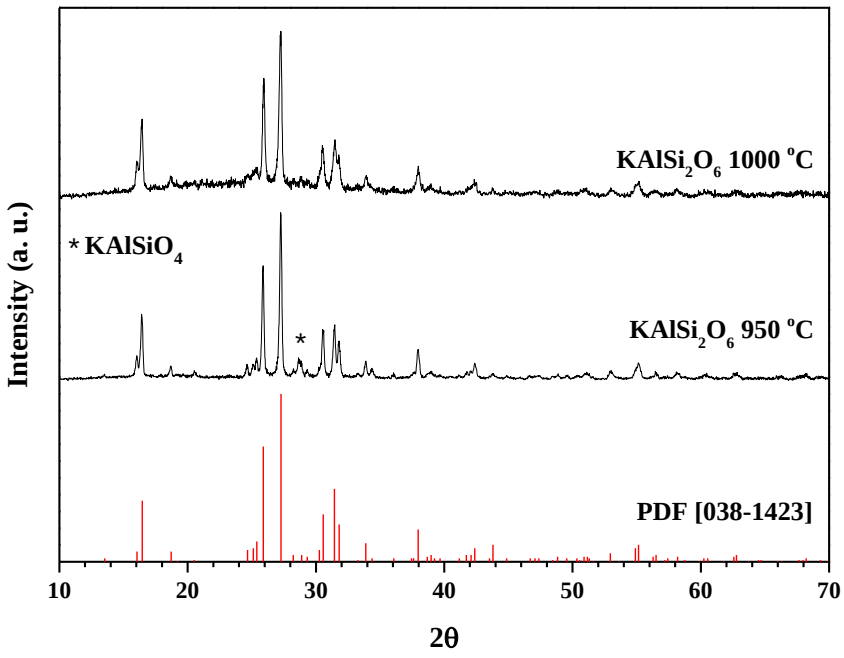

Figure 41. XRD patterns of K-Al-Si-O gel precursors annealed at 950°C for 5 h at 1000 °C for 24 h. Vertical lines represent standard XRD pattern of leucite

8.2.1.2 FTIR spectroscopy

Figure 42 represents IR spectra of ceramic powders obtained after calcination of K–Al–Si–O gel precursor at 950° C for 5 h (bottom) and 1000 ° C for 24 h (top). The broad bands located between 3500 and 3350 cm^{-1} and peaks in the region of 1620–1640 cm^{-1} correspond to adsorbed moisture from atmosphere. In both spectra, two characteristic for leucite structure peaks in the range of 1300–500 cm^{-1} are present. The most intensive peak of Si–O–Si groups located in 1034 – 1010 cm^{-1} region is due to asymmetric and symmetric stretching vibrations of the tetrahedral

network. The broad bands and peaks in the range of 850–630 cm^{-1} correspond to Al–O stretching vibrations of the AlO_x polyhedral units.

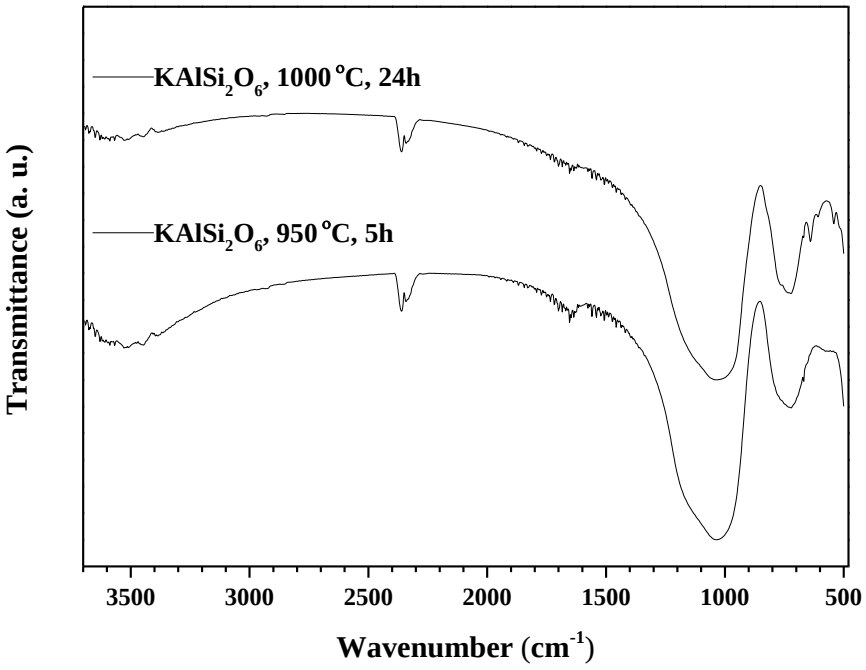

Figure 42. The IR spectra of leucite synthesized at 950° C for 5 h (bottom) and 1000° C for 24 h (top).

8.2.1.3 SEM analysis

The SEM images of synthesized leucite ceramics are shown in Figure 43. The pictures a, b and c, d are the SEM micrographs of leucite obtained after heat treatment at 950 ° C for 5 h and at 1000 ° C for 24 h, respectively. As seen in both cases, the crystalline particles with similar surface morphology have formed. Apparently, differently shaped particles with the size within a range of 0.5–5 μm can be observed. The synthesis products consist of clustered grains made up of several tiny crystallites with a defined structure. Besides, the $KAlSi_2O_6$ solids obtained at 1000 °C show slightly increased agglomeration of crystallites.

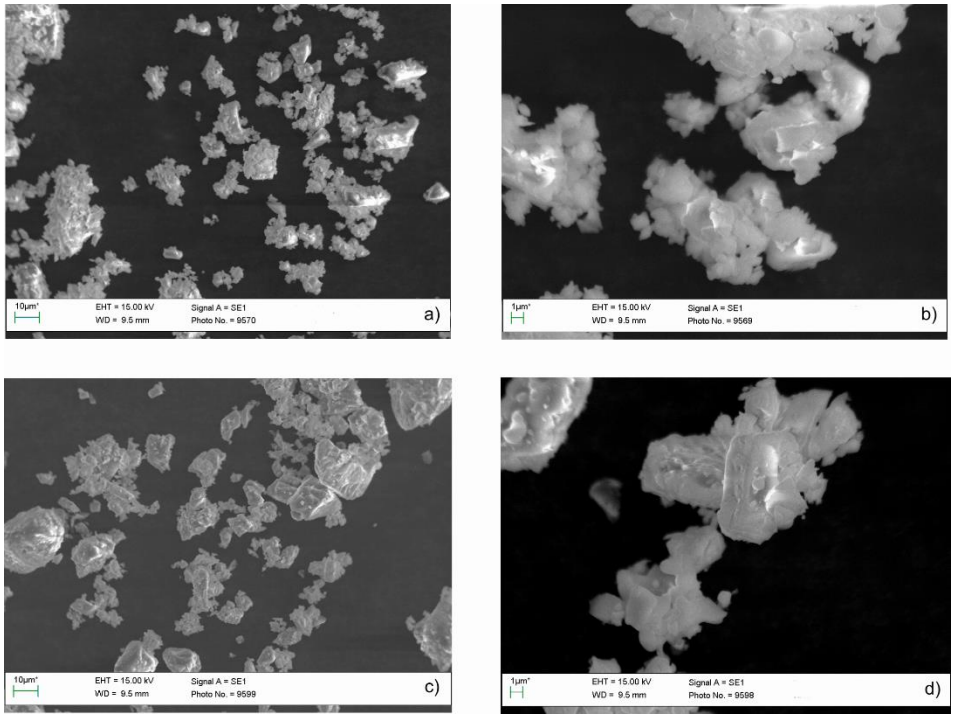

Figure 43. SEM micrographs of leucite ceramics synthesized at different temperatures: (a) and (b) – 950 °C; (c) and (d) – 1000 °C and obtained at different magnifications.

8.2.2 Lanthanide-metal substitution effects in leucite

In this study, we aimed to synthetize a series of Eu, Ce, Tb and Sm containing Le ceramic samples using an aqueous sol-gel method.

8.2.2.1 X-Ray powder diffraction analysis

XRD patterns of glass ceramics in the system of $K_2O–Al_2O_3–4SiO_2$ doped with different amount Eu^{3+}, Ce^{3+}, Tb^{3+} and Sm^{3+} ions and obtained at 1000 °C for 24 h are shown in Figure 44, Figure 45, Figure 46 and Figure 47, respectively.

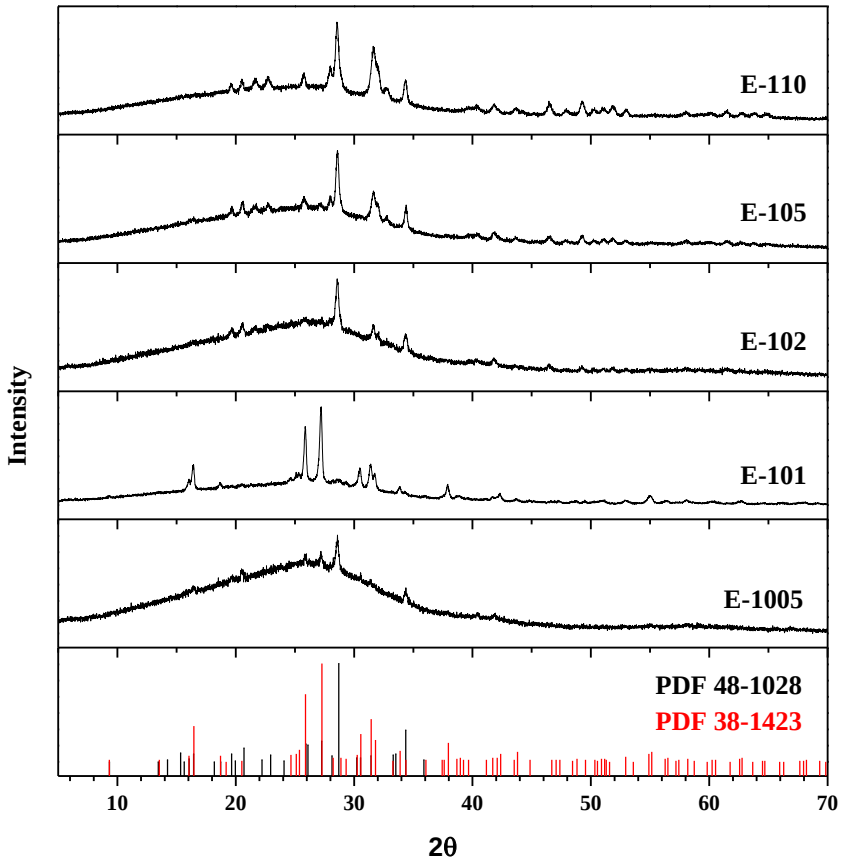

Figure 44. XRD patterns of aluminosilicate samples doped with different amount of Eu^{3+} and annealed at 1000 °C. Vertical lines represent standard XRD patterns of leucite and kalsilite

As seen from XRD pattern (Figure 44), at low concentration of europium (0.5 mol %) the synthesis product composed of two crystalline phases of kalsilite ($KAlSiO_4$) and leucite. By increasing concentration to 1 mol % the leucite phase becomes predominant and only traces of kalsilite could be identified. However, with further increasing concentration of Eu^{3+} to 10 mol % the mixture of kalsilite and leucite phases have formed.

Figure 45 shows the XRD patterns of cerium doped Le samples.

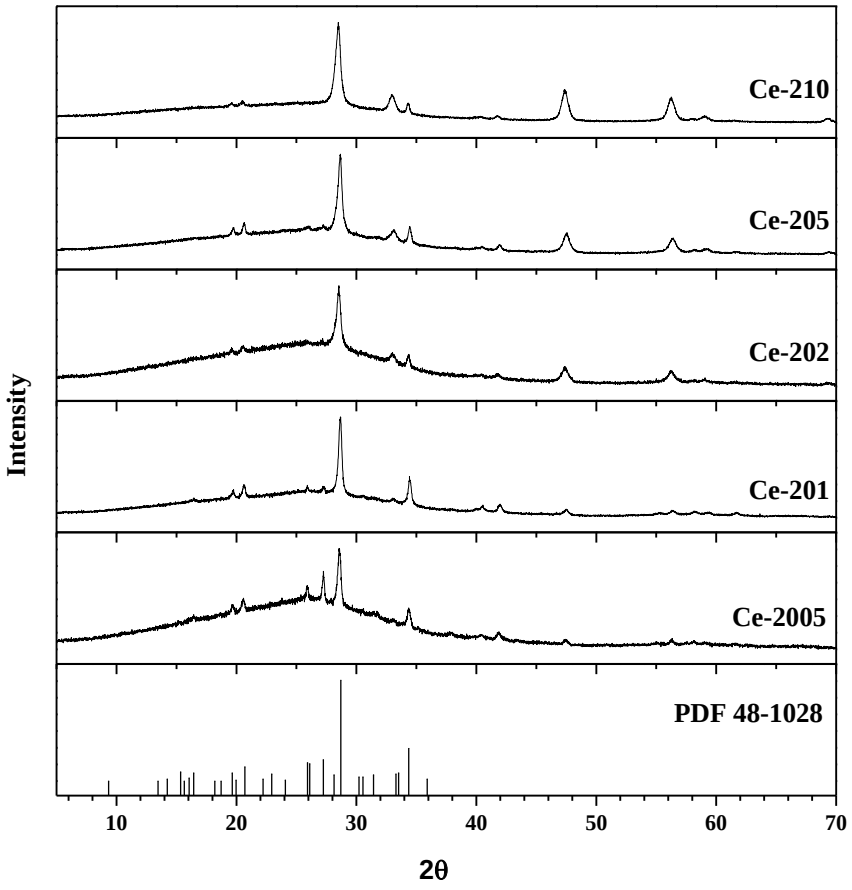

Figure 45. XRD patterns of aluminosilicate samples doped with different amount of Ce^{3+} and annealed at 1000 °C. Vertical lines represent standard XRD patterns of kalsilite

The XRD patterns of samples doped with Ce, however, mostly consist of diffraction lines attributable to the kalsilite phase with no diffraction peaks of leucite (see Figure 45). The crystallization of leucite could be achieved, possibly, by increasing the annealing temperature, although the glassification of kalsilite can also occur.

Doping with Tb and Sm gave very similar results as with Eu (see Figure 46 and Figure 47).

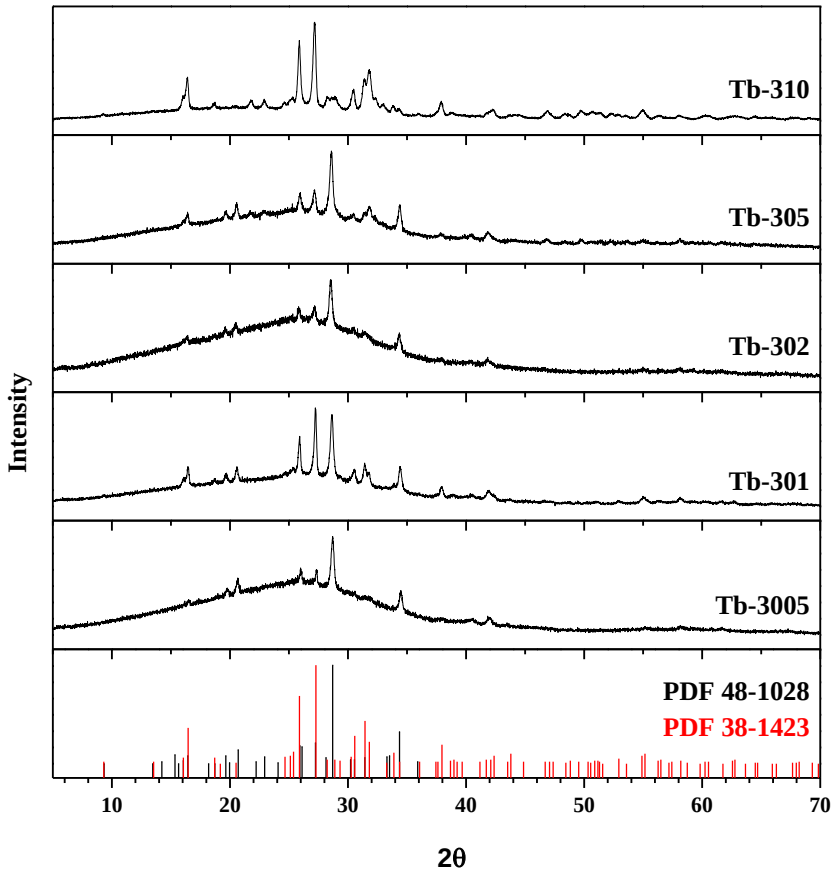

Figure 46. XRD patterns of aluminosilicate samples doped with different amount of Tb^{3+} and annealed at 1000 °C. Vertical lines represent standard XRD patterns of leucite and kalsilite

As seen, the leucite crystallizes along with kalsilite phase. The XRD patterns with dopant concentration of 0.5 mol % in both cases contain low intensity leucite and kalsilite peaks. By increasing concentration to 1 mol % the mixture of kalsilite and leucite phases could be easily identified. With increasing of Tb^{3+} and Sm^{3+} to 2.5 mol % the intensity of diffraction peaks decreases, whereas further addition of dopants to 5 and 10 mol % increased the intensity of peaks.

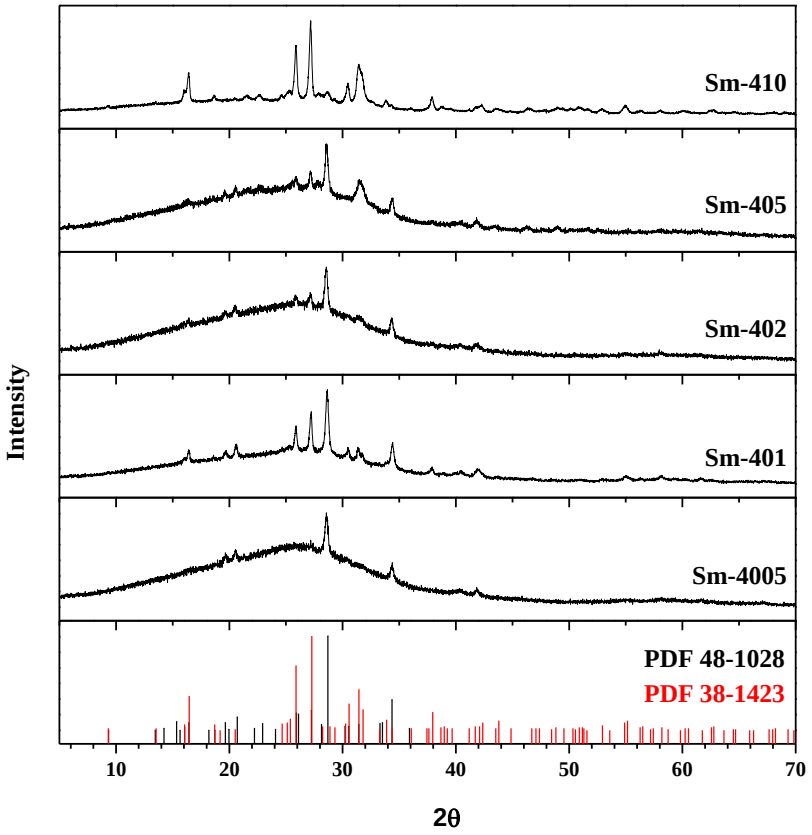

Figure 47. XRD patterns of aluminosilicate samples doped with different amount of Sm^{3+} and annealed at 1000 °C. Vertical lines represent standard XRD patterns of leucite and kalsilite

This could be due to the intermediate role of dopant in the formation of glass-ceramic structure. Lower concentrations of Eu_2O_3, Tb_4O_7 and Sm_2O_3 act as network formers while higher concentrations acts as structure modifiers and assist crystallization by weakening the glass network.

8.2.2.2 SEM and FTIR analysis

All lanthanide-doped aluminosilicate samples were analysed with scanning electron microscope. Since all samples possessed similar surface morphology, only representative SEM micrograph of Ce-doped sample is presented in Figure 48. The formation of irregular form and shape particles of mixed plates and stacks is typical feature for aluminosilicate glass-ceramics (see Figure 48). The grains are in

compact form to reduce the surface area by coalescing during the annealing procedure.

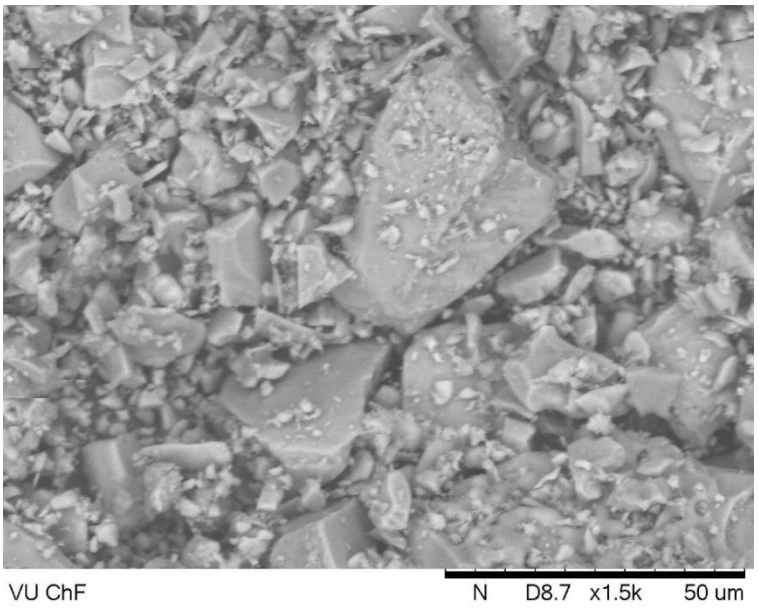

Figure 48. SEM micrograph of Ce-doped (2.5 mol %) alumosilicate sample

The representative FTIR spectra of lanthanide-doped aluminosilicate samples are given in Figure 49. It is obvious that FTIR spectra obtained for different metal doped specimens are very similar. The Si–O–Si stretching vibrations are located at around 970–1000 cm^{-1}, and the Si–O– (Si, Al) stretching vibrations are in the range of 670–580 cm^{-1}. Nevertheless, the negligible shift of the Si–O and Al–O vibration bands by changing the lanthanide element has been observed. Moreover, it was determined that dopant concentration has no influence to the qualitative view of FTIR spectra.

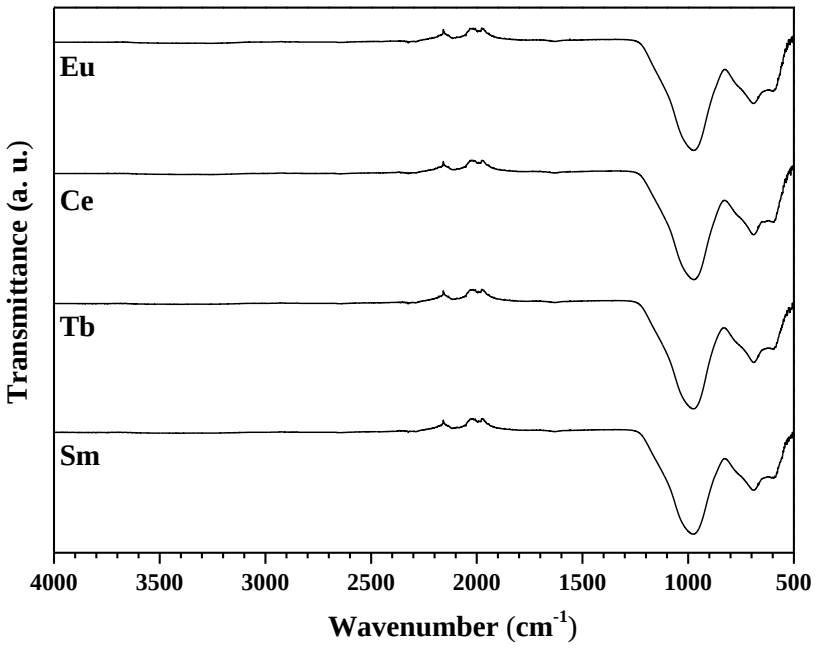

Figure 49. IR spectra of lanthanide-doped (5 mol %) alumosilicate samples

8.2.2.3 Luminescent spectroscopy studies

Figure 50 shows emission and excitation spectra of Eu^{3+}-doped (5 mol %) sample. The excitation spectrum was monitored by $^5D_0 \rightarrow {}^7F_2$ transition of Eu^{3+} ion at 616 nm. All europium containing samples exhibit a maximum excitation peak at ~394 nm along with 364, 374, 381, 414 and 464 nm. The broad and intensive band ranging from 250 to 350 nm is attributed to the charge transfer (CT) transition which can be written as $Eu^{3+} + O^{2-} \leftrightarrow Eu^{2+} + O^-$. Emission spectrum was obtained upon excitation at 265 nm. The luminescence spectrum consist of broad lines associated with $^5D_0 \rightarrow {}^7F_{0\text{-}4}$ transition (570–710 nm, orange-red region) of Eu^{3+} ions with the hypersensitive line at 616 nm.

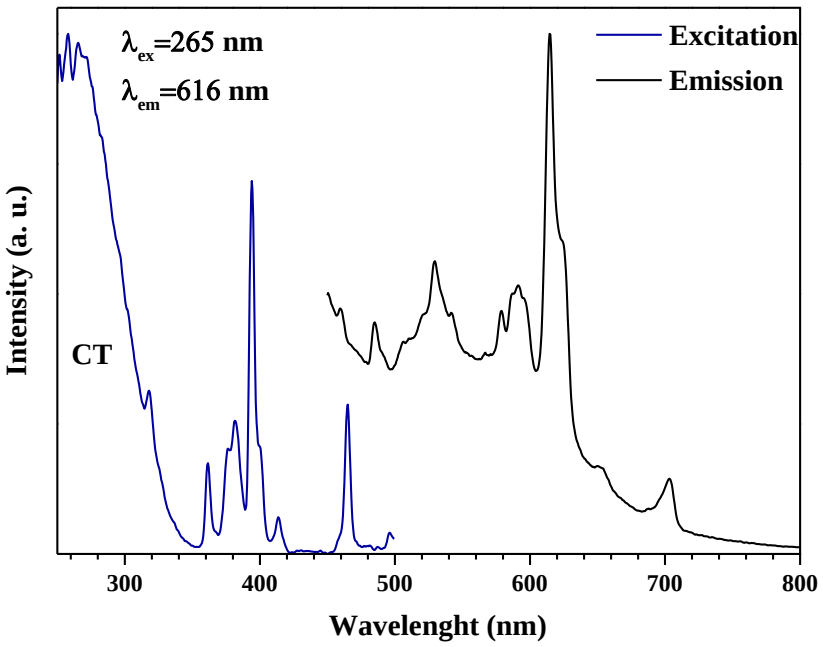

Figure 50. Excitation and emission spectra of Eu-doped (5 mol %) alumosilicate sample

The excitation and emission spectra of Tb^{3+}-doped ceramic are shown in Figure 51. The excitation spectra was measured by monitoring the green emission of Tb^{3+} ion at 547 nm. The range from 200 to 310 nm comprises of $[Xe]4f^8 \rightarrow [Xe]4f^75d^1$ transitions, which are spin and parity allowed and, therefore, very intensive. The range from 310 to 500 nm represents $[Xe]4f^8 \rightarrow [Xe]4f^8$ transitions. Emission spectra was obtained upon excitation at 260 nm. It indicates typical emission lines of Tb^{3+} ion at around 419, 440, 460, 487, 547, 550, 586 and 623 nm. The emission peak at 547 nm is dominant.

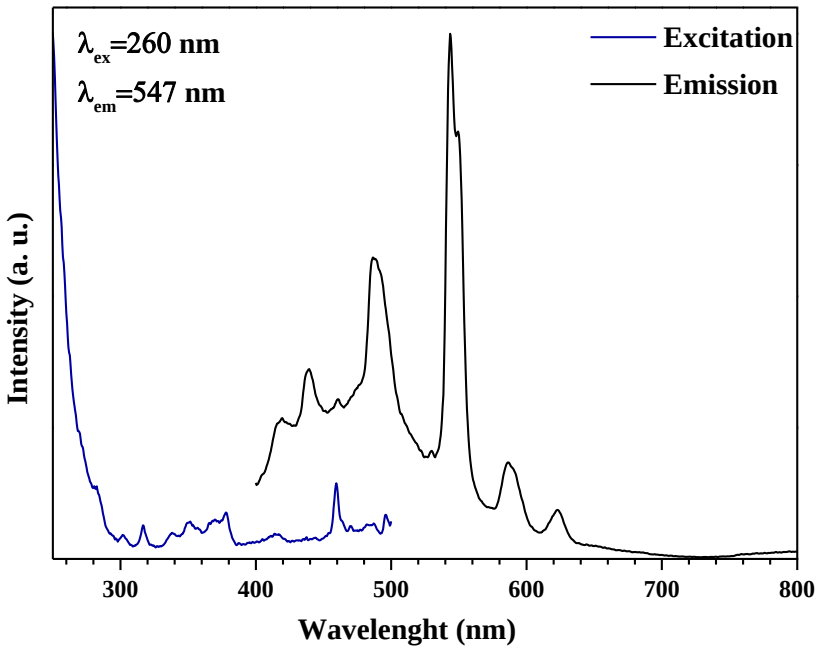

Figure 51. Excitation and emission spectra of Tb-doped (5 mol %) alumosilicate sample

Interestingly, the samples doped with cerium and samarium did not exhibit photoluminescence properties.

8.3 PREPARATION OF ALUMINOSILICATES BY RF THERMAL PLASMA SYNTHESIS ROUTE

8.3.1 Characterization of nanoscaled ceramics

8.3.1.1 Thermal analysis

Simultaneous TG and DTG analysis of treated K–Al–Si–O precursor was carried out in flowing air atmosphere in alumina crucibles in the temperature range of 50–900 °C. The measurements were made in order to evaluate the possible thermal decomposition processes of the materials obtained during the synthesis. The representative TG/DTG curves of the KAS6 material obtained after RF thermal plasma processing are presented in Figure 52.

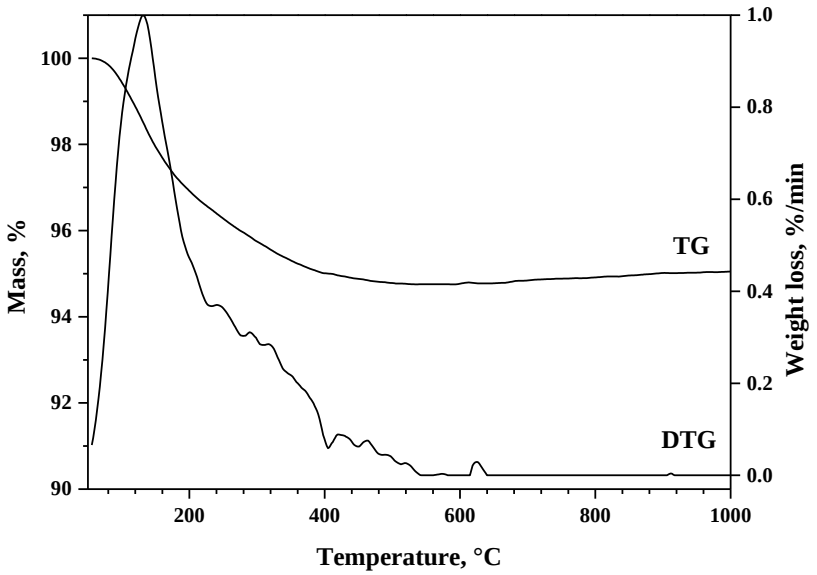

Figure 52. TG/DTG curves of the KAS6 sample obtained after RF thermal plasma processing. The heating rate was 10 °C/min

Only one weight loss attributed to the liberation of physically adsorbed and bonded water at about 100–400 °C could be detected in the TG curve. According to the DTG curve the mass loss is peaked at ~170 °C. A total weight loss of about 5 % was determined upon heating both KAS6 and KAS40 samples. The similar thermal behavior of both samples is not surprising, since they have no differences in chemical composition. In conclusion, the obtained TG/DTG results allow us to confirm that RF thermal plasma derived samples thermally stable ceramic silicates.

8.3.1.2 X-ray powder diffraction analysis

The powder X-ray diffraction analysis was performed for the qualitative determination of the phase composition of the synthesized products. The XRD patterns of both KAS6 and KAS40 samples were almost identical. A representative XRD pattern of the KAS6 sample is shown in Figure 53.

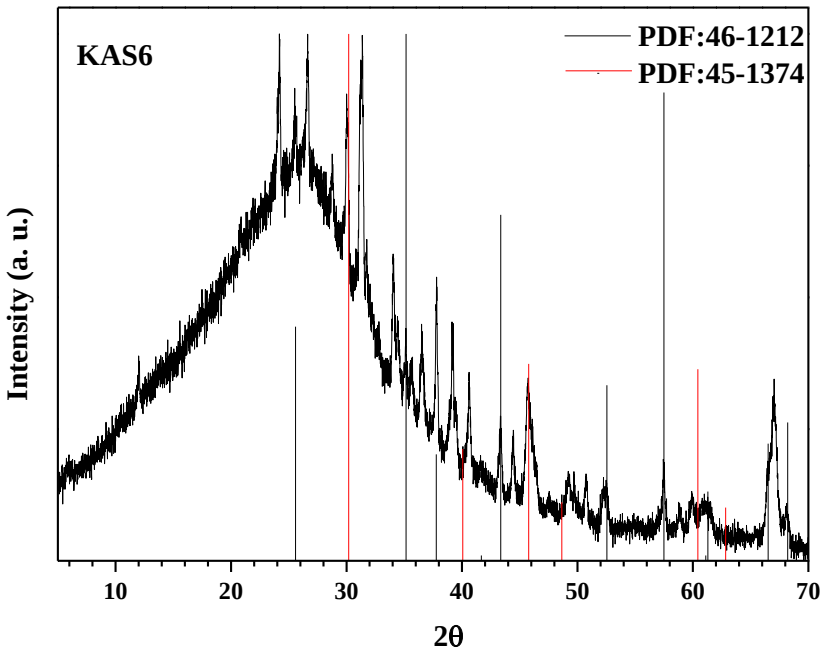

Figure 53. XRD pattern of the KAS6 powders obtained after RF thermal plasma processing. Vertical lines represent standard XRD patterns of alumina and silica

The XRD pattern displays a very high background and a broad hump at 2θ around 25 °. These features are indications of the amorphous structure of the obtained silicates [183, 220, 221]. At the same time we observe, that the yield of the solid-state reaction is not 100 %, since the diffraction lines attributable to the raw materials Al_2O_3 (PDF [46-1212]) and SiO_2 (PDF [45-1374]) are present in the same XRD patterns as well.

8.3.1.3 FTIR spectroscopy

The FTIR spectra of both KAS6 and KAS40 samples were recorded between 4000 and 500 cm^{-1} (see Figure 54). Again, the FTIR spectra of both samples have very similar absorption bands. The intense peak located in the region of 1034–1010 cm^{-1} is attributed to asymmetric and symmetric stretching vibrations of the Si–O–

Si groups. The absorption peaks corresponding to the Al–O stretching vibrations of AlO_x polyhedral units are located in the range of 850–630 cm^{-1}.

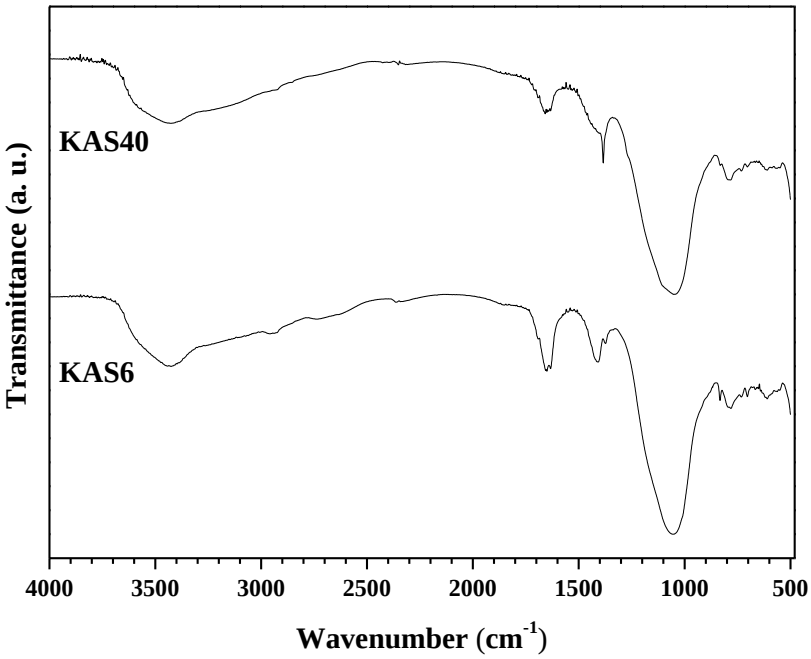

Figure 54. FTIR spectra of the KAS40 and KAS6 samples obtained after RF thermal plasma reaction

The sharp peaks which are seen in the FTIR spectra at around 1400 cm^{-1} could be attributed to ionic carbonate [222]. However, no traces of metal carbonates were determined in the samples by XRD analysis. Broad bands between 3600–3000 cm^{-1} and absorptions located at ~1640 cm^{-1} are due to water adsorbed from atmosphere.

8.3.1.4 SEM analysis

The surface morphologies of the resulting KAS6 and KAS40 samples were studied by SEM and TEM (8.3.2). The SEM micrographs of KAS6 and KAS40 samples obtained at different magnifications are shown in Figure 55. Both KAS6 and KAS40 solids consist of dispersed spherical particles. However, it is worth to take a closer look at the microstructure of both samples. Evidently, with increasing

particle size of the starting SiO_2 powders from 6 to 40 μm, smaller grains and a well-pronounced spherical shape of the synthesis products were achieved.

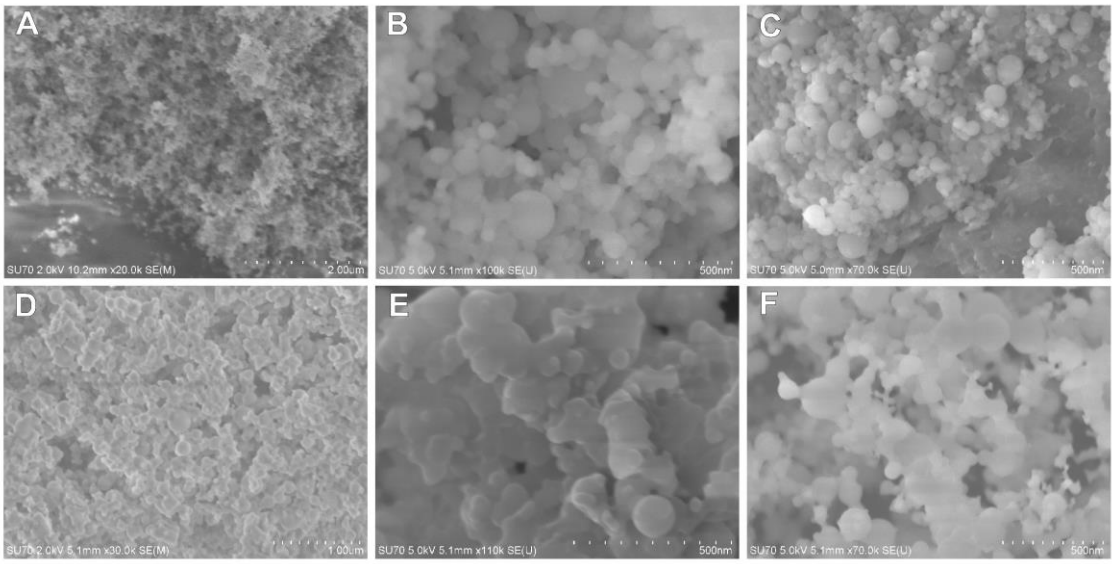

Figure 55. SEM images of the KAS40 powders at magnifications 20000x (A), 100000x (B), 70000x (C) and of the KAS6 powder at magnifications 30000x (D), 110000x (E) and 70000x (F)

Besides, the specimen KAS40 is less agglomerated, whereas KAS6 particles are strongly connected. Despite both samples being composed of spherical nanoparticles, the surface of the KAS6 sample displays a monolithic microstructure formed by agglomerated particles. On the other hand, the surface of the KAS40 sample is composed of well-pronounced smooth spherical particles that are slightly necked to each other.

8.3.2 The evidence of formation of core-shell structures

8.3.2.1 TEM analysis

The representative TEM images of the KAS6 and KAS40 samples are shown in Figure 56.

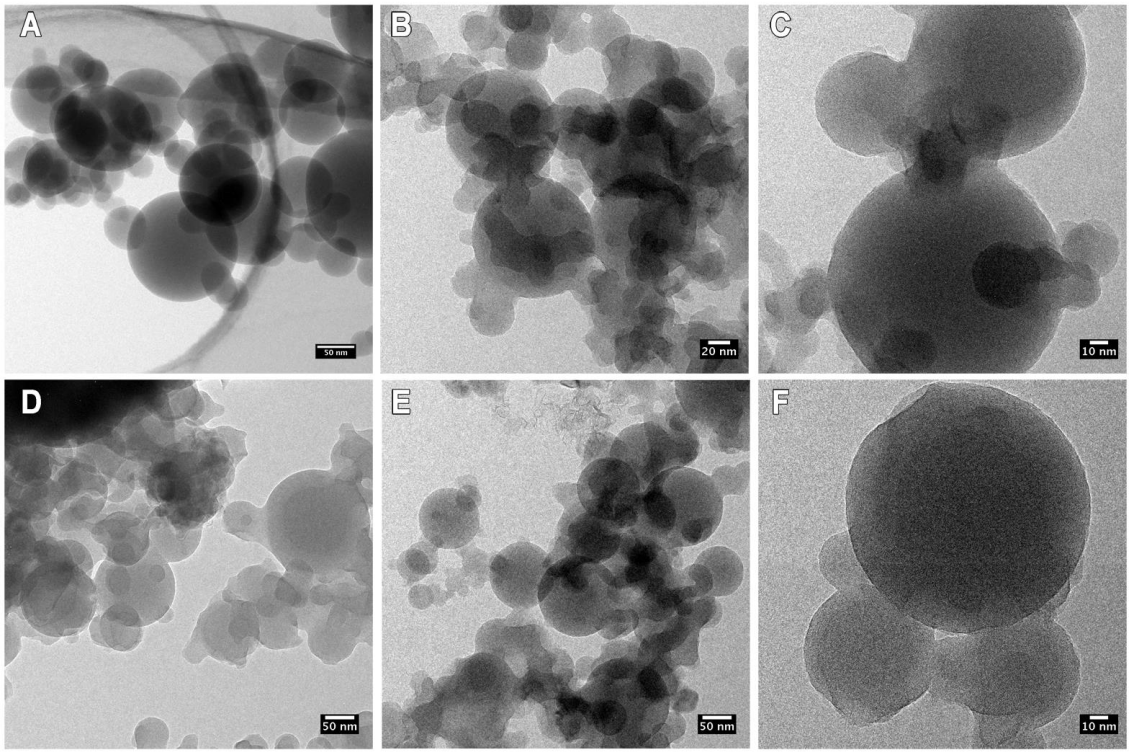

Figure 56. TEM images of the KAS40 (A, B, C) and the KAS6 (D, E, F) particles taken at different magnifications

Fine spherical particles are highly agglomerated, and almost no individual particles can be observed. The contrast of the images is mass-thickness contrast, which should vary smoothly with the diameter of the particles and should change sharply with a change in chemical composition. Since the average Z number of the core (assumed to be Al_2O_3) and the shell (assumed to be K–Si–O ceramics) are very close, the latter is not well pronounced. However, for some particles, especially in the case of the KAS40 sample, a sharp change in the contrast is observed, which can be attributed to core/shell structure [223-226] formation. The core and the shell are amorphous as can be seen from both electron diffraction patterns and TEM images (Figure 57). A high-angle angular dark field STEM image taken from the same agglomerate of the KAS40 sample is presented in Figure 57, providing additional evidence of the core-shell structure of the particles. It is unlikely that the

contrast appears from the overlapping of particles, even if the particles tend to form agglomerates.

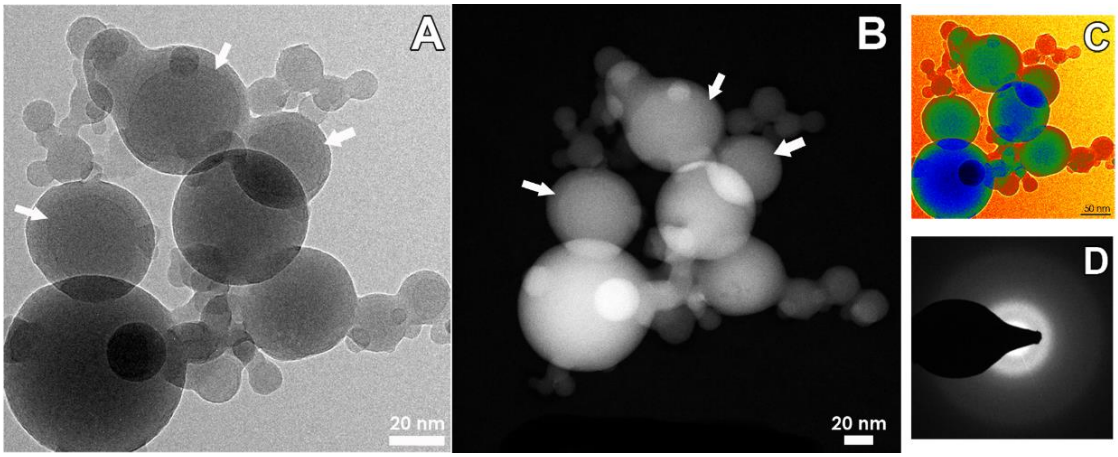

Figure 57. Images taken from the same agglomerate of particles of the KAS40 sample, using different types of contrast formation in (S)TEM (a) BF-TEM image, (b) HAADF-STEM image. Arrows indicate particles with a sharp change in contrast, which can be attributed to the core/shell structure formation. Temperature colour representation from BF-TEM helping to visualise sharp change in mass-thickness contrast (c). Diffraction pattern (d) clearly showing that the particles are amorphous

The EDX spectra confirmed the presence of Al, Si, K and O in the particles from both studied samples. The representative EDX spectrum of sample KAS40 is shown in Figure 58. However, the recorded point and line profile spectra taken along the diameter of some particles do not allow making a solid conclusion about the spatial distribution of these elements. Additional experiments should be performed to reveal the chemical composition of the core and the shell.

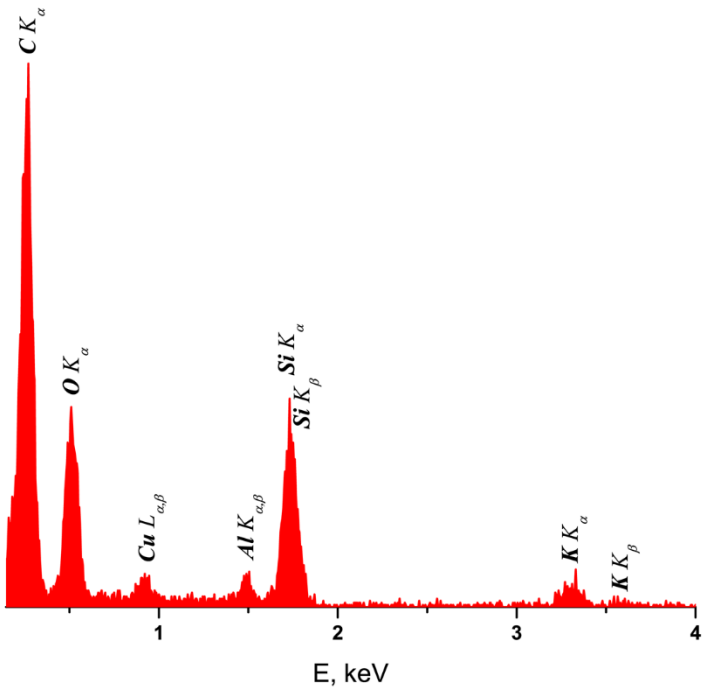

Figure 58. EDX spectrum of the KAS40 sample. The Cu and C signals come from the holey carbon film and the supporting grid

Particle size distributions for both samples were evaluated from TEM images. 150 particles were taken into consideration for each sample. The results of the particle size distribution are presented in histogram form and fitted to a log-normal distribution (see Figure 59). The average size of the KAS40 particles is found to be 48.00 ± 26.06 nm, the mode (maximum) of the log-normal distribution is 32.58 nm. The average size of the KAS6 particles is found to be 77.96 ± 61.43 nm, the mode (maximum) of the log-normal distribution is 37.71 nm. Thus, the KAS40 sample consists of smaller particles and has a more homogeneous particle size distribution than sample KAS6.

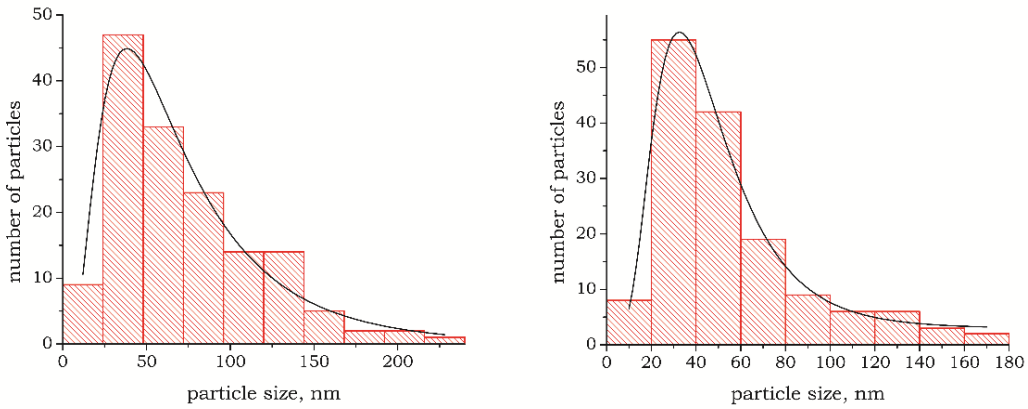

Figure 59. Particle size distribution for the KAS6 (*at left*) and KAS40 (*at right*) samples

The thermal plasma processing provides synthesis of spherical particles that are highly desirable due to large surface area. Silica and silica containing ceramics have many practical and potential applications [227]. To obtain particles of desirable size and uniformly distributed by changing parameters, such as precursor feeding rate or the flow rate of atomizing gases or the precursor concentration is already introduced and well understand [197]. The influence of one of the precursor (SiO_2) size was investigated in this work.

CHAPTER 9 CONCLUSIONS AND STATE OF THE ART

The following conclusions can be drawn from the investigations carried out in this thesis.

On the synthesis and characterization of calcium hydroxyapatite

1. CHAp was successfully synthesized using four different synthesis versions of sol-gel processing method. We developed and experimentally evaluated CHAp synthesis using aqueous sol-gel method with different starting materials (H_3PO_4 or $(NH_4)_2HPO_4$) and complexing agents (tartaric acid, ethylenediaminetetraacetic acid, 1,2-ethanediol and 1,2-diaminecyclohexanetetraacetic acid). The phase purity, as we demonstrated, was achieved after using newly proposed DCTA complexing agent.

2. Obtained CHAp samples were characterized using SEM: the particles were spherical and regular shaped, neck connected; grains are of submicron size (~200–400 nm). In conclusion, the CHAp samples having slightly different surface morphology were obtained by changing starting materials or complexing agents in the sol-gel processing. However, in all of the cases, the highly agglomerated materials of differently shaped crystallites were formed.

3. The nano-CHAp was obtained after mechanical treatment of the sol-gel derived CHAp samples using zirconia ball milling procedure. Raman spectra clearly indicated that particles size of CHAp decreased after milling procedure. The milled powders were also agglomerated, however, the milling resulted in a uniform distribution of hydroxyapatite crystallites. The grain size reduced to ~20 nm and the average surface are increased twice.

4. The interconnected bone blocks were obtained from nano-CHAp with density of 92.4 ± 2.2% and pore size of 384 ± 74 μm. This porous internal structure could provide a framework for cell growth and migration, consequently could be applicable in the bone surgery for orthopaedic purposes. The remineralization test

on human teeth was performed. The KNH results suggested that the nano-CHAp could be suitable for enamel lesions treatment.

5. In this work Ca ions in CHAp were successfully substituted with Ce and Mn ions. It was demonstrated, that higher amount of manganese (up to 10 mol %) in comparison with cerium (up to 0.25 mol %) could be introduced instead of Ca to CHAp without destroying the crystalline structure of apatite. With increasing Ce substitution concentration the CeO_2 phase could be identified in the XRD patterns. Moreover, the Mn and Ce amount did not influence morphology of the $Ca_{10-x}M_x(PO_4)_6(OH)_2$ samples.

On the synthesis and characterization of leucite using molecular precursor

6. The monophasic leucite ($KAlSi_2O_6$) ceramic was obtained using simple aqueous sol-gel synthesis route after annealing the K–Al–Si–O precursor gels at 1000 °C for 24 h. The synthesis products consisted of clustered grains made up of several tiny crystallites with a defined structure. Differently shaped particles of $KAlSi_2O_6$ with the size within a range of 0.5–5 μm have formed. Besides, the $KAlSi_2O_6$ solids obtained at 1000 °C showed slightly increased agglomeration of crystallites.

7. Utilizing this synthesis method, lanthanide-doped leucite samples were synthesized. The Ce^{3+} doped samples inhibited leucite formation favoring kalsilite ($KAlSiO_4$) crystallization. Contrary, during the sol-gel synthesis of Eu^{3+}-, Tb^{3+}- and Sm^{3+}-doped leucite samples the mixture of both leucite and kalsilite phases has formed.

8. Luminescent properties of lanthanide-doped leucite samples were investigated. Emission spectrum of Eu^{3+}-doped (5 mol %) sample was obtained upon excitation at 265 nm and consisted of broad lines associated with $^5D_0 \rightarrow {}^7F_{0-4}$ transition (570–710 nm, orange-red region) of Eu^{3+} ions with the hypersensitive line at 616 nm. The luminescence spectrum of Tb^{3+}-doped ceramic upon excitation at 260 nm showed the dominant emission peak at 547 nm. Thus, Eu^{3+} and Tb^{3+}

containing alumosilicate samples showed luminescence under UV radiation, however, the similarly obtained Ce^{3+}- and Tb^{3+}-doped samples did not exhibit any photoluminescence properties.

On the preparation of the aluminosilicates by RF thermal plasma synthesis route

9. In this study, an amorphous ternary system of alumina-silicate ceramic powders containing an alkaline earth metal was prepared by the RF thermal plasma processing route. For the preparation of precursors, Al_2O_3 (~10 μm), KOH and two differently sized crystalline SiO_2 powders (~6 μm and ~40 μm) were used as starting materials. The TG/DTG results confirmed that the RF thermal plasma derived samples were fine-structure K–Al–Si–O ceramics. The XRD and electron diffraction patterns of the obtained specimens showed that they are amorphous.

10. The SEM and TEM measurements revealed that the overall morphology of the synthesized products depends on the initial size of the SiO_2 powders used in the RF thermal plasma processing. With increasing particle size of the starting silica, the obtained spherical nanograins of the final powders were smaller and less agglomerated. Moreover, the synthesized alumo-silicate nanoceramics possess a core/shell structure. These nanoscaled core-shell particles could be attractive due to the possibly enhanced mechanical properties for different structural applications.

CHAPTER 10 LIST OF PUBLICATIONS

10.1 ARTICLES IN JOURNALS

1. **Audrone Jankeviciute** and Aivaras Kareiva, *Synthesis and Characterization of Leucite Ceramics Using Sol–Gel Derived Molecular Precursors,* Mendeleev Communications, **21** (2011) 287–288

2. **Audrone Jankeviciute**, Zoltán Károly, Nadezda V. Tarakina, János Szépvölgyi, Aivaras Kareiva, *Synthesis and Characterization of Spherical Amorphous Alumo-Silicate Nanoparticles Using RF Thermal Plasma Method*, Journal of Non-Crystalline Solids **359** (2013) 9–14

10.2 PUBLISHED CONTRIBUTIONS TO ACADEMIC CONFERENCES

1. **Audrone Jankeviciute** and Aivaras Kareiva, *Synthesis of Leucite from Molecular Precursor,* MOLMAT 2010: 4th International Conference on Molecular Materials: Montpellier (France), July 5-8 (2010) p. 215.

2. **Audrone Jankeviciute** and Aivaras Kareiva, *Synthesis of Leucite from Molecular Precursor,* Advanced Materials and Technologies and European Doctorate in Physics and Chemistry of Advanced Materials: Book of Abstracts of The 12-Th International Summer School-Conference, Palanga, Lithuania, (2010) p. 81

3. **Audrone Jankeviciute**, Zoltán Károly, Nadezda V. Tarakina, János Szépvölgyi, Aivaras Kareiva, *RF Thermal Plasma Synthesis of Core-Shell Alumina Amorphous Ceramics Nanosized Particles*, Chemistry 2011: 10th International Conference of Lithuanian Chemists, Vilnius, 14-15 October, (2011): Abstracts. ISBN 9789955634652 P. 55.

4. **Audrone Jankeviciute**, Zoltán Károly, Nadezda V. Tarakina, János Szépvölgyi, Aivaras Kareiva, *Thermal Plasma Synthesis of Core-Shell Amorphous Nanosized Alumina Ceramics Particles,* Advanced Materials and Technologies:

Book of Abstracts of The 13-Th International Conference-School, Palanga, Lithuania, 27-31 August (2011). ISSN 1822-7759 p. 105.

5. **Audrone Jankeviciute**, Zoltán Károly, Nadezda V. Tarakina, János Szépvölgyi, Aivaras Kareiva, *Synthesis and Characterization of Spherical Amorphous Alumo-Silicate Nanoparticles Using RF Thermal Plasma Method*, Nanochemistry and Nanomaterials: International Conference of Young Chemists, 7-9 December, (2012), Palanga, Lithuania : Conference Program and Book of Abstracts. ISBN 9786094591389 p. 26.

6. Olga Ščit, **Audronė Jankevičiūtė**, Irma Bogdanovičienė, Rimantas Ramanauskas, Aldona Beganskienė, Aivaras Kareiva, *Preparation and Characterization of Sol-Gel Derived Lathanide-Doped Calcium Hydrohyapatite Powders*, Advanced Materials and Technologies: Book if Abstracts if The 14-Th International Conference-School, Palanga, Lithuania, 27-31 August (2012). ISSN 1822-7759 p. 109.

7. Olga Ščit, Irma Bogdanovičienė, **Audronė Jankevičiūtė**, Aldona Beganskienė, Aivaras Kareiva, *Sol-Gel Processing and Characterization of Calcium Hydroxyapatite (CHA) Nanoparticles*, Nanotechnology 2012: 9th International Conference on Nanosciences and Nanotechnologies (NN12), 3-6 July (2012), Thessaloniki, Greece. p. 269.

8. Aivaras Kareiva, Živilė Stankevičiūtė, **Audronė Jankevičiūtė**, Jen-Chang Yang, Irma Bogdanovičienė, Karlis A. Gross, Thomas C-K. Yang, *Sol-Gel Design of Calcium Hydroxyapatite Nanostructures for Dental Applications*, Multifunctional, Hybrid and Nanomaterials: 3rd International Conference, 3-7 March (2013), Sorrento, Italy: [abstracts]. p. [A.1.12.1].

10.3 PUBLICATIONS NOT INCLUDED IN THE THESIS

1. Irma Bogdanovicienė, **Audronė Jankeviciutė**, Jiri Pinkas, Aldona Beganskienė, Aivaras Kareiva, *Sol-gel Synthesis and Characterization of Kalsilite-type Alumosilicates,* Materials Science (Medžiagotyra) **13, No. 3** (2007).

2. Irma Bogdanovicienė, **Audronė Jankeviciutė**, Jiri Pinkas, Aldona Beganskienė, Aivaras Kareiva, *Study of Alumosilicate Porcelains: Sol–gel Preparation, Characterization and Erosion Evaluated by Gravimetric Method*, Materials Research Bulletin **43** (2008) 2998–3007.

3. **Audrone Jankeviciute** and Aivaras Kareiva, $KAlSiO_4$ ir $K_{0.5}Na_{0.5}AlSiO_4$ sintezė zolių-gelių metodu bei tyrimai, Neorganiniai junginiai: sintezė, savybės ir panaudojimas, Vilniaus universiteto jaunųjų chemikų konferencija, (2006) p 15.

CHAPTER 11 REFERENCES

[1] J.A. Roether, A.R. Boccaccini, L.L. Hench, V. Maquet, S. Gautier, R. Jérôme, *Biomaterials* **23** (2002) 3871-8.
[2] J.R. Kelly, *Annual Review of Materials Science* **27** (1997) 443-68.
[3] D.F. Williams, *Biomaterials* **29** (2008) 2941-53.
[4] S.M. Best, A.E. Porter, E.S. Thian, J. Huang, *Journal of the European Ceramic Society* **28** (2008) 1319-27.
[5] L.L. Hench, S.M. Best, in: B.D. Ratner, A.S. Hoffman, F.J. Schoen, J.E. Lemons (Eds.), Biomaterials Science (Third Edition), Academic Press, 2013, pp. 128-51.
[6] L.L. Hench, R.J. Splinter, W.C. Allen, T.K. Greenlee, *Journal of Biomedical Materials Research* **5** (1971) 117-41.
[7] W. Bonfield, M. Wang, K. Tanner, *Acta Materialia* **46** (1998) 2509-18.
[8] K. De Groot, R. Geesink, C.P.A.T. Klein, P. Serekian, *Journal of Biomedical Materials Research* **21** (1987) 1375-81.
[9] T. Kokubo, *Thermochimica Acta* **280** (1996) 479-90.
[10] A. Ito, S. Nakamura, H. Aoki, M. Akao, K. Teraoka, S. Tsutsumi, K. Onuma, T. Tateishi, *Journal of Crystal Growth* **163** (1996) 311-7.
[11] M. Jarcho, C.H. Bolen, M.B. Thomas, J. Bobick, J.F. Kay, R.H. Doremus, *Journal of Materials Science* **11** (1976) 2027-35.
[12] D. Avnir, T. Coradin, O. Lev, J. Livage, *Journal of Materials Chemistry* **16** (2006) 1013-30.
[13] B. Cabal, F. Malpartida, R. Torrecillas, A. Hoppe, A.R. Boccaccini, J.S. Moya, *Advanced Engineering Materials* **13** (2011) B462-B6.
[14] M. Vallet-Regi, *Journal of the Chemical Society, Dalton Transactions* (2001) 97-108.
[15] A. Hoppe, N.S. Guldal, A.R. Boccaccini, *Biomaterials* **32** (2011) 2757-74.
[16] R.W. Phillips, C. Shen, H.R. Rawls, K.J. Anusavice, Phillip's Science of Dental Materials~ autofilled~, Elsevier Health Sciences, 2003.
[17] M.M. Barreiro, E.E. Vicente, *Journal of Materials Science-Materials in Medicine* **4** (1993) 431-6.
[18] M. Eslami, Z. Hamnabard, N. Ali, *Journal of Rare Earths* **31** (2013) 595-9.
[19] P. Chimalawong, J. Kaewkhao, C. Kedkaew, P. Limsuwan, *Journal of Physics and Chemistry of Solids* **71** (2010) 965-70.
[20] S.V. Dorozhkin, *Biomaterials* **31** (2010) 1465-85.
[21] D.F. Williams, *Biomaterials* **30** (2009) 5897-909.
[22] J.A. Planell, S. Best, D. Lacroix, A. Merolli, Bone repair biomaterials, Elsevier, 2009.
[23] L.L. Hench, J.M. Polak, *Science* **295** (2002) 1014-7.

[24] W. Höland, V. Rheinberger, M. Schweiger, *Philosophical Transactions of the Royal Society of London. Series A: Mathematical, Physical and Engineering Sciences* **361** (2003) 575-89.
[25] L.L. Hench, *Journal of the American Ceramic Society* **74** (1991) 1487-510.
[26] M. Vallet-Regí, C.V. Ragel, Antonio J. Salinas, *European Journal of Inorganic Chemistry* **2003** (2003) 1029-42.
[27] I.D. Xynos, A.J. Edgar, L.D.K. Buttery, L.L. Hench, J.M. Polak, *Journal of Biomedical Materials Research* **55** (2001) 151-7.
[28] D. Arcos, M. Vallet-Regi, *Acta Biomaterialia* **6** (2010) 2874-88.
[29] Q. Lin, X.H. Lan, Y.B. Li, Y.R. Ni, C.H. Lu, Y.X. Chen, Z.Z. Xu, *Materials Science & Engineering C-Materials for Biological Applications* **31** (2011) 629-36.
[30] W. Holand, V. Rheinberger, E. Apel, C. Ritzberger, F. Rothbrust, H. Kappert, F. Krumeich, R. Nesper, *Journal of the European Ceramic Society* **29** (2009) 1291-7.
[31] K. Franks, I. Abrahams, J.C. Knowles, *Journal of Materials Science: Materials in Medicine* **11** (2000) 609-14.
[32] I. Ahmed, M. Lewis, I. Olsen, J.C. Knowles, *Biomaterials* **25** (2004) 491-9.
[33] K.L. Skelton, J.V. Glenn, S.A. Clarke, G. Georgiou, S.P. Valappil, J.C. Knowles, S.N. Nazhat, G.R. Jordan, *Acta Biomaterialia* **3** (2007) 563-72.
[34] M. Bitar, V. Salih, V. Mudera, J.C. Knowles, M.P. Lewis, *Biomaterials* **25** (2004) 2283-92.
[35] T. Kokubo, M. Shigematsu, Y. Nagashima, M. Tashiro, T. Nakamura, T. Yamamuro, S. Higashi, *Bulletin of the Institute for Chemical Research, Kyoto University* **60** (1982).
[36] S. Huang, P. Cao, Y. Li, Z. Huang, W. Gao, *Crystal Growth & Design* **13** (2013) 4031-8.
[37] J. Juhasz, S. Best, *Journal of Materials Science* (2011) 1-15.
[38] J.C.M. Souza, R.M. Nascimento, A.E. Martinelli, *Surface & Coatings Technology* **205** (2010) 787-92.
[39] J.R. Jones, *Acta Biomaterialia* **9** (2013) 4457-86.
[40] L. Lefebvre, J. Chevalier, L. Gremillard, R. Zenati, G. Thollet, D. Bernache-Assolant, A. Govin, *Acta Materialia* **55** (2007) 3305-13.
[41] K. Franks, I. Abrahams, G. Georgiou, J. Knowles, *Biomaterials* **22** (2001) 497-501.
[42] C. Garcia, S. Cere, A. Duran, *Journal of Non-Crystalline Solids* **348** (2004) 218-24.
[43] J. Zhong, D.C. Greenspan, *Journal of Biomedical Materials Research* **53** (2000) 694-701.
[44] X. Chatzistavrou, D. Esteve, E. Hatzistavrou, E. Kontonasaki, K. Paraskevopoulos, A. Boccaccini, *Bioceramics Development and Applications* **1** (2011) 1-4.
[45] R. Li, A.E. Clark, L.L. Hench, *Journal of Applied Biomaterials* **2** (1991) 231-9.

[46] L. Hench, *Journal of Materials Science: Materials in Medicine* **17** (2006) 967-78.
[47] P. Saravanapavan, J.R. Jones, R.S. Pryce, L.L. Hench, *Journal of Biomedical Materials Research Part A* **66A** (2003) 110-9.
[48] P. Saravanapavan, L.L. Hench, *Journal of Non-Crystalline Solids* **318** (2003) 1-13.
[49] A. Sadiasa, S.K. Sarkar, R.A. Franco, Y.K. Min, B.T. Lee, *Journal of Biomaterials Applications* **28** (2014) 739-56.
[50] N.J. Hallab, J.J. Jacobs, in: B.D. Ratner, A.S. Hoffman, F.J. Schoen, J.E. Lemons (Eds.), Biomaterials Science (Third Edition), Academic Press, 2013, pp. 841-82.
[51] G. Binyamin, B.M. Shafi, C.M. Mery, *Seminars in Pediatric Surgery* **15** (2006) 276-83.
[52] J. Ballarre, D.A. Lopez, W.H. Schreiner, A. Duran, S.M. Cere, *Applied Surface Science* **253** (2007) 7260-4.
[53] A.A. Campbell, *Materials Today* **6** (2003) 26-30.
[54] Y. Yang, K.-H. Kim, J.L. Ong, *Biomaterials* **26** (2005) 327-37.
[55] L. Sun, C.C. Berndt, K.A. Gross, A. Kucuk, *Journal of Biomedical Materials Research* **58** (2001) 570-92.
[56] C.-H. Wang, J.-h. Wu, H.-Y. Li, P.-P. Wang, H.-E. Lee, J.-K. Du, *Journal of Dental Sciences* **8** (2013) 314-20.
[57] Y. Zhang, C. Qu, J.Q. Wu, M. Lu, P.G. Rao, X.X. Liu, *Journal of Wuhan University of Technology-Materials Science Edition* **23** (2008) 452-5.
[58] A. Tsetsekou, T. Papadopoulos, O. Adamopoulos, *Journal of Materials Science-Materials in Medicine* **13** (2002) 407-16.
[59] S. Hashimoto, A. Yamaguchi, K. Fukuda, S.W. Zhang, *Materials Research Bulletin* **40** (2005) 1577-83.
[60] W. Höland, M. Schweiger, M. Frank, V. Rheinberger, *Journal of Biomedical Materials Research* **53** (2000) 297-303.
[61] J. Dong, H. Luthy, A. Wohlwend, P. Schärer, *International Journal of Prosthodontics* **5** (1992).
[62] S.-C. Oh, J.-K. Dong, H. Lüthy, P. Schärer, *International Journal of Prosthodontics* **13** (2000).
[63] R. Dimitriou, E. Jones, D. McGonagle, P. Giannoudis, *BMC Medicine* **9** (2011) 66.
[64] C.G. Finkemeier, *The Journal of Bone & Joint Surgery* **84** (2002) 454-64.
[65] O.B. Fergal J, *Materials Today* **14** (2011) 88-95.
[66] G. Wei, P.X. Ma, *Biomaterials* **25** (2004) 4749-57.
[67] H. Dietmar W, *Biomaterials* **21** (2000) 2529-43.
[68] S. Sánchez-Salcedo, D. Arcos, M. Vallet-Regí, *Key Engineering Materials* **377** (2008) 19-42.
[69] http://www.biomech.ethz.ch/research/muller_group/ste.
[70] E. Sachlos, J. Czernuszka, *Eur Cell Mater* **5** (2003) 39-40.

[71] D. Bellucci, V. Cannillo, A. Sola, F. Chiellini, M. Gazzarri, C. Migone, *Ceramics International* **37** (2011) 1575-85.
[72] Q.Z. Chen, I.D. Thompson, A.R. Boccaccini, *Biomaterials* **27** (2006) 2414-25.
[73] T. Kokubo, Bioceramics and their clinical applications, Elsevier, 2008.
[74] D. Shi, Introduction to Biomaterials, World Scientific, 2006.
[75] S.V. Dorozhkin, M. Epple, *Angewandte Chemie International Edition* **41** (2002) 3130-46.
[76] C. Robinson, R.C. Shore, S.J. Brookes, S. Strafford, S.R. Wood, J. Kirkham, *Critical Reviews in Oral Biology & Medicine* **11** (2000) 481-95.
[77] http://cnx.org/content/m46511/latest/#fig-ch24_03_05.
[78] K. Fujita, S. Ma, M. Aida, T. Maeda, T. Ikemi, M. Hirata, N. Nishiyama, *Journal of Dental Research* **90** (2011) 607-12.
[79] J.H. Shepherd, D.V. Shepherd, S.M. Best, *Journal of Materials Science: Materials in Medicine* **23** (2012) 2335-47.
[80] T. Suzuki, T. Hatsushika, Y. Hayakawa, *Journal of the Chemical Society, Faraday Transactions 1: Physical Chemistry in Condensed Phases* **77** (1981) 1059-62.
[81] M. Mathew, S. Takagi, *Journal of Research of NIST* **106** (2001) 1035-44.
[82] X. Ma, D.E. Ellis, *Biomaterials* **29** (2008) 257-65.
[83] M. Corno, C. Busco, B. Civalleri, P. Ugliengo, *Physical Chemistry Chemical Physics* **8** (2006) 2464-72.
[84] S.V. Dorozhkin, *Journal of Functional Biomaterials* **1** (2010) 22-107.
[85] J.B. Park, R.S. Lakes, *Biomaterials* (2007) 459-83.
[86] I. Bogdanoviciene, A. Beganskiene, K. Tõnsuaadu, J. Glaser, H. Meyer, A. Kareiva, *Materials Research Bulletin* **41** (2006) 1754-62.
[87] M. Ferraz, F. Monteiro, C. Manuel, *Journal of Applied Biomaterials and Biomechanics* **2** (2004) 74-80.
[88] M. Fathi, A. Hanifi, V. Mortazavi, *Journal of materials processing technology* **202** (2008) 536-42.
[89] S. Samal, D.-W. Park, *Chemical Engineering Research and Design* **90** (2012) 548-54.
[90] S.E. Saddow, Silicon carbide biotechnology : biocompatible semiconductor for advanced biomedical devices and applications, 1st ed., Elsevier, Amsterdam, 2012.
[91] H. Tagai, H. Aoki, Preparation of synthetic hydroxyapatite and sintering of apatite ceramics, ^'Mechanical Properties of Biomaterials'. Proc. Conf. at Keele Univ., Sept., 1978. Edited by G. W. Hastings and D. F. Williams. Chichester, Wiley, 1980., (1978).
[92] E. Bouyer, F. Gitzhofer, M. Boulos, *Journal of Materials Science: Materials in Medicine* **11** (2000) 523-31.
[93] E. Hayek, H. Newesely, M.L. Rumpel, *Inorganic Syntheses, Volume 7* (1963) 63-5.

[94] M.H. Santos, M.d. Oliveira, L.P.d.F. Souza, H.S. Mansur, W.L. Vasconcelos, *Materials Research* **7** (2004) 625-30.
[95] C. Manuel, M. Ferraz, F. Monteiro, *Key Engineering Materials* **240** (2003) 555-8.
[96] D. Janaćković, I. Jankovic-Castvan, R. Petrović, L. Kostic-Gvozdenovic, S. Milonjić, D. Uskoković, *Key Engineering Materials* **240** (2002) 437-40.
[97] B.-H. Chen, K.-I. Chen, M.-L. Ho, H.-N. Chen, W.-C. Chen, C.-K. Wang, *Materials Chemistry and Physics* **113** (2009) 365-71.
[98] W.-J. Shih, Y.-F. Chen, M.-C. Wang, M.-H. Hon, *Journal of Crystal Growth* **270** (2004) 211-8.
[99] R.E. Riman, W.L. Suchanek, *Advances in Science and Technology* **45** (2006) 184-93.
[100] M. Sadat-Shojai, *Journal of the Iranian Chemical Society* **6** (2009) 386-92.
[101] I.S. Neira, Y.V. Kolen'ko, O.I. Lebedev, G. Van Tendeloo, H.S. Gupta, F. Guitián, M. Yoshimura, *Crystal Growth and Design* **9** (2008) 466-74.
[102] S. Jinawath, D. Pongkao, W. Suchanek, M. Yoshimura, *International Journal of Inorganic Materials* **3** (2001) 997-1001.
[103] Y.-z. Zhao, J. Zhu, S.-h. Zhu, Y.-y. Huang, Z.-y. Li, K.-c. Zhou, *Transactions of Nonferrous Metals Society of China* **21** (2011) 1773-8.
[104] A. Aminian, M. Solati-Hashjin, A. Samadikuchaksaraei, F. Bakhshi, F. Gorjipour, A. Farzadi, F. Moztarzadeh, M. Schmücker, *Ceramics International* **37** (2011) 1219-29.
[105] F. Bakan, O. Laçin, H. Sarac, *Powder Technology* **233** (2013) 295-302.
[106] A. Deptula, W. Lada, T. Olczak, A. Borello, C. Alvani, A. Dibartolomeo, *Journal of Non-Crystalline Solids* **147** (1992) 537-41.
[107] Y. Masuda, K. Matubara, S. Sakka, *Nippon Seramikkusu Kyokai Gakujutsu Ronbunshi-Journal of the Ceramic Society of Japan* **98** (1990) 1255-66.
[108] A. Balamurugan, J. Michel, J. Faure, H. Benhayoune, L. Wortham, G. Sockalingum, V. Banchet, S. Bouthors, D. Laurent-Maquin, G. Balossier, *Ceramics-Silikaty* **50** (2006) 27-31.
[109] T. Brendel, A. Engel, C. Russel, *Journal of Materials Science-Materials in Medicine* **3** (1992) 175-9.
[110] H. Takahashi, M. Yashima, M. Kakihana, M. Yoshimura, *European Journal of Solid State and Inorganic Chemistry* **32** (1995) 829-35.
[111] U. Vijayalakshmi, S. Rajeswari, *Trends in Biomaterials and Artificial Organs* **19** (2006) 57-62.
[112] D. Haddow, P. James, R. Van Noort, *Journal of Materials Science: Materials in Medicine* **7** (1996) 255-60.
[113] C.S. Chai, K.A. Gross, B. Ben-Nissan, *Biomaterials* **19** (1998) 2291-6.
[114] A. Jillavenkatesa, R.A. Condrate, *Journal of Materials Science* **33** (1998) 4111-9.
[115] B. Ben-Nissan, D.D. Green, G.S.K. Kannangara, C.S. Chai, A. Milev, *Journal of Sol-Gel Science and Technology* **21** (2001) 27-37.

[116] S.R. Ramanan, R. Venkatesh, *Materials Letters* **58** (2004) 3320-3.
[117] H. Arce, M.L. Montero, A. Saenz, V.M. Castano, *Polyhedron* **23** (2004) 1897-901.
[118] M.L. Montero, A. Saenz, V.M. Castano, *Journal of Materials Science* **39** (2004) 339-41.
[119] A. Saenz, M.L. Montero, V.M. Castano, *Physica Status Solidi B-Basic Research* **230** (2002) 347-50.
[120] K.S. Tenhuisen, P.W. Brown, *Journal of Materials Science-Materials in Medicine* **5** (1994) 291-8.
[121] H.K. Varma, S.S. Babu, *Ceramics International* **31** (2005) 109-14.
[122] T.A. Kuriakose, S.N. Kalkura, M. Palanichamy, D. Arivuoli, K. Dierks, G. Bocelli, C. Betzel, *Journal of Crystal Growth* **263** (2004) 517-23.
[123] A. Bigi, E. Boanini, K. Rubini, *Journal of Solid State Chemistry* **177** (2004) 3092-8.
[124] K. Cheng, S. Zhang, W.J. Weng, *Journal of Sol-Gel Science and Technology* **38** (2006) 13-7.
[125] M.F. Hsieh, L.H. Perng, T.S. Chin, H.G. Perng, *Biomaterials* **22** (2001) 2601-7.
[126] D.M. Liu, T. Troczynski, W.J. Tseng, *Biomaterials* **22** (2001) 1721-30.
[127] M. Manso-Silvan, M. Langlet, C. Jimenez, M. Fernandez, J.M. Martinez-Duart, *Journal of the European Ceramic Society* **23** (2003) 243-6.
[128] A.C. Taş, *Journal of the American Ceramic Society* **84** (2001) 295-300.
[129] C.C. Silva, A.S.B. Sombra, *Journal of Physics and Chemistry of Solids* **65** (2004) 1031-3.
[130] S.-H. Rhee, *Biomaterials* **23** (2002) 1147-52.
[131] W. Kim, Q. Zhang, F. Saito, *Journal of Materials Science* **35** (2000) 5401-5.
[132] I. Kimura, *Research Letters in Materials Science* **2007** (2007).
[133] M. Shirkhanzadeh, *Journal of Materials Science: Materials in Medicine* **9** (1998) 67-72.
[134] A. Cüneyt Tas, *Biomaterials* **21** (2000) 1429-38.
[135] J.B. Liu, K.W. Li, H. Wang, M.K. Zhu, H. Yan, *Chemical Physics Letters* **396** (2004) 429-32.
[136] S.K. Padmanabhan, E. Ul Haq, A. Licciulli, *Current Applied Physics* **14** (2014) 87-92.
[137] M. Omori, T. Onoki, T. Hashida, A. Okubo, Y. Murakami, *Ceramics International* **32** (2006) 617-21.
[138] P. Rouhani, N. Taghavinia, S. Rouhani, *Ultrasonics Sonochemistry* **17** (2010) 853-6.
[139] E. Boanini, M. Gazzano, A. Bigi, *Acta Biomaterialia* **6** (2010) 1882-94.
[140] F. Ren, R. Xin, X. Ge, Y. Leng, *Acta Biomaterialia* **5** (2009) 3141-9.
[141] F. Miyaji, Y. Kono, Y. Suyama, *Materials Research Bulletin* **40** (2005) 209-20.

[142] D. Laurencin, N. Almora-Barrios, N.H. de Leeuw, C. Gervais, C. Bonhomme, F. Mauri, W. Chrzanowski, J.C. Knowles, R.J. Newport, A. Wong, Z. Gan, M.E. Smith, *Biomaterials* **32** (2011) 1826-37.
[143] I. Mayer, F. Cuisinier, S. Gdalya, I. Popov, *Journal of inorganic biochemistry* **102** (2008) 311-7.
[144] C. Zollfrank, L. Müller, P. Greil, F.A. Müller, *Acta Biomaterialia* **1** (2005) 663-9.
[145] Y. Lin, Z. Yang, J. Cheng, *Journal of Rare Earths* **25** (2007) 452-6.
[146] R. Ternane, M.T. Cohen-Adad, G. Panczer, C. Goutaudier, C. Dujardin, G. Boulon, N. Kbir-Ariguib, M. Trabelsi-Ayedi, *Solid State Sciences* **4** (2002) 53-9.
[147] M. Hidouri, K. Boughzala, J.P. Lecompte, K. Bouzouita, *Comptes Rendus Physique* **10** (2009) 242-8.
[148] L.M. Rodriguez-Lorenzo, J.N. Hart, K.A. Gross, *Biomaterials* **24** (2003) 3777-85.
[149] M. Bohner, *Injury* **31, Supplement 4** (2000) D37-D47.
[150] S.V. Dorozhkin, *Materials* **2** (2009) 399-498.
[151] S.V. Dorozhkin, *Journal of Materials Science* **43** (2008) 3028-57.
[152] S.V. Dorozhkin, *Journal of Materials Science* **42** (2007) 1061-95.
[153] L. Wang, G.H. Nancollas, *Chemical reviews* **108** (2008) 4628-69.
[154] J. Zhou, X. Zhang, J. Chen, S. Zeng, K. De Groot, *Journal of Materials Science: Materials in Medicine* **4** (1993) 83-5.
[155] S. Oh, N. Oh, M. Appleford, J.L. Ong, *American Journal of Biochemistry & Biotechnology* **2** (2006).
[156] M. Sadat-Shojai, M.-T. Khorasani, E. Dinpanah-Khoshdargi, A. Jamshidi, *Acta Biomaterialia* **9** (2013) 7591-621.
[157] H. Eshtiagh-Hosseini, M.R. Housaindokht, M. Chahkandi, *Materials Chemistry and Physics* **106** (2007) 310-6.
[158] A. Bigi, B. Bracci, F. Cuisinier, R. Elkaim, M. Fini, I. Mayer, I. Mihailescu, G. Socol, L. Sturba, P. Torricelli, *Biomaterials* **26** (2005) 2381-9.
[159] K. Bleek, A. Taubert, *Acta Biomaterialia* **9** (2013) 6283-321.
[160] A. Farzadi, M. Solati-Hashjin, F. Bakhshi, A. Aminian, *Ceramics International* **37** (2011) 65-71.
[161] O. Suzuki, *Acta Biomaterialia* **6** (2010) 3379-87.
[162] M. Kutz, Standard handbook of biomedical engineering and design, McGraw-Hill, New York, 2003.
[163] J.E. Lemons, C.E. Misch, in: B.D. Ratner, A.S. Hoffman, F.J. Schoen, J.E. Lemons (Eds.), Biomaterials Science (Third Edition), Academic Press, 2013, pp. 882-8.
[164] W.A. B, W.L. K, Fused porcelain-to-metal teeth, Se^condary Fused porcelain-to-metal teeth, Google Patents, 1962.
[165] S. Assmann, M. Ermrich, K. Kunzmann, *Journal of Materials Science* **36** (2001) 5403-6.
[166] X.X. Li, L.L. Shaw, *Materials Letters* **61** (2007) 3946-50.

[167] J.R. Kelly, P. Benetti, *Australian Dental Journal* **56** (2011) 84-96.
[168] M. Atai, E. Yassini, M. Amini, D.C. Watts, *Dental Materials* **23** (2007) 1181-7.
[169] W. Höland, V. Rheinberger, E. Apel, C. van't Hoen, *Journal of the European Ceramic Society* **27** (2007) 1521-6.
[170] B. Kukiattrakoon, C. Hengtrakool, U. Kedjarune-Leggat, *Dental Materials Journal* **29** (2010) 502-11.
[171] C. Fredericci, H. Yoshimura, A. Molisani, M. Pinto, P. Cesar, *Ceramics International* **37** (2011) 1073-8.
[172] C. Baerlocher, L.B. McCusker, D.H. Olson, Atlas of zeolite framework types, Elsevier, 2007.
[173] I. Yanase, S. Tamai, S. Matsuura, H. Kobayashi, *Journal of the European Ceramic Society* **25** (2005) 3173-9.
[174] F. Mtzzt, *American Mineralogist* **61** (1976) 108-15.
[175] I. Yanase, K. Ichiyoshi, H. Kobayashi, *Solid State Communications* **139** (2006) 1-4.
[176] I.E. Paukov, I.A. Belitsky, B.A. Fursenko, *Thermochimica Acta* **387** (2002) 23-8.
[177] D.C. Palmer, E.K.H. Salje, *Physics and Chemistry of Minerals* **17** (1990) 444-52.
[178] http://www.iza-online.org/natural/Datasheets/Leucite/leucite.htm.
[179] S. Hashimoto, F. Sato, S. Honda, H. Awaji, K. Fukuda, *Journal of the Ceramic Society of Japan* **113** (2005) 488-90.
[180] Y. Zhang, J.Q. Wu, P.G. Rao, M. Lv, *Materials Letters* **60** (2006) 2819-23.
[181] Y. Zhang, M. Lv, D.D. Chen, J.Q. Wu, *Materials Letters* **61** (2007) 2978-81.
[182] N. Xie, J.L. Bell, W.M. Krivenw, *Journal of the American Ceramic Society* **93** (2010) 2644-9.
[183] Y. Zhang, M. Lv, P.G. Rao, A.Z. Shui, H.Q. Wu, *Journal of the Ceramic Society of Japan* **115** (2007) 329-32.
[184] M.J. Cattell, T.C. Chadwick, J.C. Knowles, R.L. Clarke, D.Y.D. Samarawickrama, *Dental Materials* **22** (2006) 925-33.
[185] X. Chen, T.C. Chadwick, R.M. Wilson, R.G. Hill, M.J. Cattell, *Dental Materials* **27** (2011) 1153-61.
[186] X. Chen, T.C. Chadwick, R.M. Wilson, R. Hill, M.J. Cattell, *Journal of Dental Research* **89** (2010) 1510-6.
[187] M.B. Tosic, R.Z. Dimitrijevic, M.M. Mitrovic, *Journal of Materials Science* **37** (2002) 2293-303.
[188] M.J. Cattell, T.C. Chadwick, J.C. Knowles, R.L. Clarke, E. Lynch, *Dental Materials* **17** (2001) 21-33.
[189] M. Kohoutkova, A. Klouzkova, P. Kostka, M. Mrazova, *Journal of Non-Crystalline Solids* **354** (2008) 741-8.

[190] A. Klouzkova, M. Mrazova, M. Kohoutkova, *Journal of Physics and Chemistry of Solids* **68** (2007) 1207-10.
[191] K. Annapurna, R.N. Dwivedi, A. Kumar, A.K. Chaudhuri, S. Buddhudu, *Spectrochimica Acta Part a-Molecular and Biomolecular Spectroscopy* **56** (2000) 103-9.
[192] A.D. Sontakke, K. Biswas, K. Annapurna, *Journal of Luminescence* **129** (2009) 1347-55.
[193] G.C. Righini, M. Ferrari, *Rivista del Nuovo Cimento* **28** (2005) 1-53.
[194] M. Aoyama, T. Hayakawa, S. Honda, Y. Iwamoto, *Journal of Luminescence* **132** (2012) 2603-7.
[195] C.P. Yoganand, V. Selvarajan, V. Cannillo, A. Sola, E. Roumeli, O.M. Goudouri, K.M. Paraskevopoulos, M. Rouabhia, *Ceramics International* **36** (2010) 1757-66.
[196] T. Watanabe, A. Nezu, Y. Abe, Y. Ishii, K. Adachi, *Thin Solid Films* **435** (2003) 27-32.
[197] I. Mohai, J. Szepvolgyi, *Chemical Engineering and Processing* **44** (2005) 225-9.
[198] T. Ishigaki, J.-G. Li, *Science and Technology of Advanced Materials* **8** (2007) 617-23.
[199] Z. Károly, J. Szépvölgyi, Z. Farkas, *Powder Technology* **110** (2000) 169-78.
[200] D. Vollath, *Journal of Nanoparticle Research* **10** (2008) 39-57.
[201] J. Xu, K.A. Khor, Z. Dong, Y. Gu, R. Kumar, P. Cheang, *Materials Science and Engineering: A* **374** (2004) 101-8.
[202] E. Gomez, D.A. Rani, C.R. Cheeseman, D. Deegan, M. Wise, A.R. Boccaccini, *Journal of Hazardous Materials* **161** (2009) 614-26.
[203] J. Szepvolgyi, I. Mohai, Z. Karoly, L. Gal, *Journal of the European Ceramic Society* **28** (2008) 895-9.
[204] Z. Karoly, J. Szepvogyi, *Powder Technology* **132** (2003) 211-5.
[205] Z. Károly, J. Szépvölgyi, *Chemical Engineering and Processing: Process Intensification* **44** (2005) 221-4.
[206] J.M. Kim, S.M. Chang, S. Kim, K.-S. Kim, J. Kim, W.-S. Kim, *Ceramics International* **35** (2009) 1243-7.
[207] H. Lei, P. Zhang, *Applied Surface Science* **253** (2007) 8754-61.
[208] J.H. Seo, J.S. Kim, M.Y. Lee, W.T. Ju, I.T. Nam, *Thin Solid Films* **519** (2011) 7111-5.
[209] D. Harbec, F. Gitzhofer, A. Tagnit-Hamou, *Powder Technology* **214** (2011) 356-64.
[210] Y.K. Kim, K.P. Rajesh, J.-S. Yu, *Journal of Hazardous Materials* **260** (2013) 350-7.
[211] J.Y. Thompson, B.R. Stoner, J.R. Piascik, *Materials Science and Engineering: C* **27** (2007) 565-9.
[212] H. Herman, S. Sampath, R. McCune, *Mrs Bulletin* **25** (2000) 17-25.
[213] S. Cha, Y.-S. Park, *Clinical Plasma Medicine* (2014).

[214] C.P. Yoganand, V. Selvarajan, J.S. Wu, D.F. Xue, *Vacuum* **83** (2008) 319-25.
[215] C.J. Brinker, G.W. Scherer, Sol-gel science: the physics and chemistry of sol-gel processing, Gulf Professional Publishing, 1990.
[216] L. Jia, F. Gitzhofer, *Plasma Chemistry and Plasma Processing* **29** (2009) 497-513.
[217] A. Paz, D. Guadarrama, M. López, J. E. González, N. Brizuela, J. Aragón, *Química Nova* **35** (2012) 1724-7.
[218] E. Garskaite, K.-A. Gross, S.-W. Yang, T.C.-K. Yang, J.-C. Yang, A. Kareiva, *CrystEngComm* **16** (2014) 3950-9.
[219] J.-P. Lafon, E. Champion, D. Bernache-Assollant, R. Gibert, A.-M. Danna, *Journal of Thermal Analysis and Calorimetry* **72** (2003) 1127-34.
[220] C. Özgür, F. Çolak, O. Şan, *Journal of Non-Crystalline Solids* **357** (2011) 116-20.
[221] D. Chen, L. Li, J. Liu, S. Qi, F. Tang, X. Ren, W. Wu, J. Ren, L. Zhang, *Journal of Colloid and Interface Science* **308** (2007) 351-5.
[222] N. Dubnikova, E. Garskaite, J. Pinkas, P. Bezdicka, A. Beganskiene, A. Kareiva, *Journal of Sol-Gel Science and Technology* **55** (2010) 213-9.
[223] D.P. Wang, X. Duan, J.Y. Zhang, A.H. Yao, L.Y. Zhou, W.H. Huang, *Journal of Materials Science* **44** (2009) 4020-5.
[224] R.P. Maiti, S. Basu, S. Bhattacharya, D. Chakravorty, *Journal of Non-Crystalline Solids* **355** (2009) 2254-9.
[225] Y. Sun, G. Guo, B. Yang, X. Zhou, Y. Liu, G. Zhao, *Journal of Non-Crystalline Solids* **357** (2011) 1085-9.
[226] L. Tong, D. Liu, J. Shi, X. Yang, H. Yang, *Journal of Materials Science* **47** (2012) 132-7.
[227] W.J. Stark, S.E. Pratsinis, *Powder Technology* **126** (2002) 103-8.